CENTRO DE INVESTIGACIÓN Y DE ESTUDIOS AVANZADOS DEL INSTITUTO POLITÉCNICO NACIONAL

Unidad Mérida

DEPARTAMENTO DE FÍSICA APLICADA

"Propiedades mecánicas de la monocapa de BeH_2: un estudio a primeros principios"

TESIS

Que presenta

Armando Antonio Morín Martínez

Para obtener el grado de

Maestro en Ciencias

en

Fisicoquímica

Director de Tesis:

Dr. José Gabriel Merino Hernández

Mérida, Yucatán, México Diciembre de 2020

CENTRO DE INVESTIGACIÓN Y DE ESTUDIOS AVANZADOS DEL INSTITUTO POLITÉCNICO NACIONAL

Unidad Mérida

DEPARTAMENTO DE FÍSICA APLICADA

"Mechanical properties of the BeH_2 monolayer: a first–principles study"

a thesis submitted by:

Armando Antonio Morín Martínez

In partial fulfillment of the requirements for the degree of

Master of Sciences

in

Physical Chemistry

Thesis Advisor:

Dr. José Gabriel Merino Hernández

Mérida, Yucatán, México December, 2020

A Gloria y Armando,

por todo el amor y el apoyo.

Agradecimientos

El viaje fue largo, pero sin duda, bastante enriquecedor. No hubiese sido posible llegar a esta instancia sin el continuo apoyo de mi familia y amigos, a quienes les estoy extremadamente agradecido.

Desearía expresar un profundo agradecimiento al Dr. Gabriel Merino, mi asesor, por haberme permitido formar parte de su grupo de investigación. Por su experiencia, paciencia, y puntuales observaciones que ayudaron en la elaboración de esta tesis.

No puedo dar cuenta a lo agradecido que estoy con el Dr. Miguel E. Cifuentes Quintal por su tutoría, y el tiempo que invirtió en brindarme nuevas perspectivas que no hicieron más que nutrir este trabajo.

Desearía también, extender mi agradecimiento hacia mi comité de sinodales, el Dr. Romeo de Coss y el Dr. Ricardo Grau-Crespo, por el tiempo que dedicaron en la revisión de este trabajo, y por sus valiosos comentarios y sugerencias.

Agradezco también al personal administrativo y de apoyo del Cinvestav, por su asistencia durante mi estancia en la institución. Muchas gracias a los compañeros y amigos de laboratorio, de clases, y del campus. Gracias por las charlas de ciencia, y las de no-ciencia también, gracias por haberme permitido tantas experiencias a su lado que me han hecho crecer personal y profesionalmente.

Por último, agradezco a las instituciones que han permitido hacer esto posible. Al Cinvestav unidad Mérida por permitirme hacer uso de sus instalaciones, y a los profesores de la unidad que han participado en mi proceso de formación. Al Conacyt por haberme brindado una beca para realizar mis estudios de posgrado, así como al proyecto Conacyt No. CB–2015–252356, el cual ha facilitado la realización de este trabajo.

Resumen

En este trabajo se discuten las propiedades mecánicas de dos monocapas recientemente propuestas, α-BeH_2 y β-BeH_2. Los estados fundamentales de α-BeH_2 y β-BeH_2 se analizaron a un nivel GGA-PBE, ambas monocapas son similares en energía, siendo α-BeH_2 ligeramente favorecida. La estabilidad de las monocapas como estructuras independientes se evaluó al estimar sus energías de cohesión y calcular las energías de interacción intercapa en distintas configuraciones de apilamiento de bicapas. La estructura electrónica se analizó determinando las estructuras de bandas a lo largo de los puntos de alta simetría y se calcularon las densidades de estados (DOS), obteniendo brechas de energía prohibida cercanas a los 5 eV en ambos compuestos. La interacción entre orbitales se analizó mediante la DOS proyectada (pDOS) y con el esquema de población cristalino proyectado por las superposiciones del hamiltoniano (pCOHP), determinando los distintos pares de contactos con interacciones enlazantes y se calcularon las fuerzas de enlace, para que, en conjunto con las diferencias de densidades de carga, se obtiene un panorama más claro sobre la naturaleza del enlace en estos cristales. La respuesta elástica lineal se evaluó calculando las constantes elásticas de segundo orden (SOEC) y las propiedades elásticas dependientes de la dirección también se consideraron. La red periódica cristalina de α-BeH_2 es cuadrada y ésta tiene un coeficiente de Poisson negativo (NPR, por sus siglas en inglés); su anisotropía revela un coeficiente de Poisson positivo (PPR) grande a ángulos de 45° y el módulo de elasticidad en esta orientación es mucho más bajo qué el obtenido para la orientación con NPR. En la búsqueda por encontrar las inestabilidades mecánicas para las direcciones de tensión uniaxiales y biaxiales, primero se calcularon los esfuerzos de tensión ideal para después, adoptando una súper celda, estimar las transiciones de fase. Existen transiciones de fase para todas las direcciones evaluadas mucho antes de llegar a las deformaciones críticas. Los resultados son contrastantes, debido a que mientras α-BeH_2 exhibe una elasticidad superior a la mayoría de los materiales 2D conocidos, β-BeH_2 se vuelve inestable a valores de deformación muy pequeños. En un esfuerzo por comprender las marcadas diferencias entre las elasticidades de ambas monocapas, se estudiaron los cambios elásticos estructurales. Además, se elucidó el mecanismo que produce al NPR de α-BeH_2 al determinar los cambios estructurales en los

componentes de la red cristalina. Este cristal bidimensional se presenta así mismo como un caso de estudio interesante, ya que provee una ventana excepcional para cuantificar y distinguir como un compuesto con dos fases estables puede, desde la microestructura, ofrecer respuestas mecánicas y comportamientos ante la deformación muy variados.

Abstract

Herein, the mechanical properties of two recently predicted monolayers, α-BeH_2 and β-BeH_2, are presented. The ground-states of α-BeH_2 and β-BeH_2 are predicted at the GGA-PBE level of theory, both monolayers are energetically similar, with α-BeH_2 being the more energetically favored. A study on the stability of the monolayers as free-standing structures was performed by estimating their cohesive energies and by calculating the interlayer binding energies in bilayers of several stacking orders. The electronic structure was analyzed by determining the band structures along the high-symmetry points and the density of states (DOS), obtaining large forbidden energy band gaps of ~5 eV for both compounds. Orbital interactions were analyzed via projected DOS (pDOS) and through the projected Crystal Overlap Hamiltonian Population (pCOHP) scheme, several pairwise bonding contacts were detected and their bond strengths were also computed, so that, together with density of charges differences, a clearer perspective on the bonding nature of the materials can be reached. The linear-elastic response was evaluated by determining the second order elastic constants (SOEC) and the direction-dependent elastic properties accounted for. The periodic α-BeH_2 crystal has a square lattice with a negative Poisson's ratio (NPR). Its anisotropy reveals a large positive Poisson's ratio at angles of 45° and the elastic modulus at this direction is much lower than in the direction with an NPR. The ideal tensile strengths for uniaxial and biaxial tensile directions of strain are then pursued, first by computing the ideal tensile strengths, and then, using a supercell approach, computing the phase transitions. Mechanical instabilities begin to occur for all tested directions much before reaching the critical strains. The computed results are intriguing, while α-BeH_2 reveals appealing high elasticity, β-BeH_2 fails at very low strains. The elastic structural changes were studied in order to understand why the marked differences in elasticity for both polymorphs, is achieved. Moreover, the mechanism that produces the NPR in α-BeH_2 has been elucidated from measuring the structural changes in the components of the lattice. This polymorphic 2D crystal presents itself as an interesting case study, as it provides an exceptional window to quantify and distinguish how a compound with two stable phases, will have a varied mechanical response and behavior against strains from the microstructure.

Table of Contents

List of Figures

List of Tables

Introduction

When a solid is subjected to an external load, its volume and shape change. This knowledge has allowed us, throughout millennia, to voluntarily modify many materials into products of "load-bearing" applications. The understanding of the behavior of materials against external forces has been of core importance to the development of human civilization. Today, as materials research continues to expand and develop novel compounds, a large emphasis is held on studying their mechanical properties. Even when the primary function may be other than mechanical, the resistance to deformations plays a crucial role in the success of the desired application.

The macroscopic approach to assess the mechanical properties of solid materials is heavily influenced by the defects present in the system, undermining their usable strength.[1] Over time, the techniques used to evaluate these properties have progressed consistently, to the point where these can be measured at the nanoscale, giving insightful information on the chemical bonding of materials.[2] Together with the development of novel technologies has impacted positively on the growth of more powerful computational resources, and together with the enhancement of simulation tools to describe theoretical models, it is possible to accurately predict the mechanical properties of crystals within a small range of error to the observed values.

Furthermore, computational models allow us to predict features not easily available in real world conditions. Properties like the elastic constants, which contain essential information on the response of solids against external forces at small deformations; or the ideal strength, which sets the upper boundary of strength a perfect material can have against a uniform load, can be estimated from computations. Such achievements have given scientists worldwide the tools to study not only bulk solids, but also, to tap into systems of lower dimensions.

The concept of two-dimensional (2D) materials became more than a textbook exercise by the turn of the XXI century, as graphene was isolated and characterized by Novoselov *et al*.[3-4] Graphene is a carbon allotrope that consists of a single layer of atoms

disposed over a hexagonal array. Soon enough, many reports began to appear regarding the novel electronic properties offered by this material,[5] seen for the very first time in solid-state systems. Exceptional mechanical properties were also revealed,[6-7] which catapulted graphene as the lightest, strongest material known. The area of opportunities brought about with the introduction of graphene convinced the materials community that there is plenty of space at the 2D scale.

Several of the 2D materials first isolated with graphene, like hexagonal boron nitride (h-BN) or molybdenum disulfide (MoS_2), have hexagonal lattices.[8] This infers that inside a range of small deformations (infinitesimal strains), the output given by these materials is invariant of the direction of measure. However, 2D materials are not limited to this lattice symmetry and, in turn, exhibit an interesting array of exotic and anomalous properties rarely detected in isotropic solids.[9] These anisotropic materials exhibit properties that are dependent on the direction whence they are measured. One such direction-dependent property is the Poisson's ratio (ν), a measure of the structural changes in a solid produced at the dimensions perpendicular to the applied load.

When a material is distorted in a given direction, a change of size at the perpendicular dimensions will occur, this is the Poisson effect and its unit of measure is the Poisson's ratio, $\upsilon = -\varepsilon_{\perp}/\varepsilon_{\parallel}$, where ν is the negative of the quotient between the perpendicular strain ($\varepsilon_{\perp}$) and the parallel strain ($\varepsilon_{\parallel}$).[10] Most materials' response against tension is to contract in the directions traverse to the applied load, yielding a positive Poisson's ratio (PPR). Nevertheless, some few known materials go against intuition and, for particular directions, exhibit a negative Poisson's ratio (NPR).[11] NPR materials (also called auxetics) were popularized after the re-entrant metallic foam produced by Lakes in 1987.[12] Phosphorene became the first documented evidence of an NPR in 2D materials,[13-14] the mechanism of its NPR holds much resemblance to the hinged microstructure of Lakes. Auxetic materials are very alluring due to their observed improved resistance against indentation, fracture toughness, and vibration damping.[15] Naturally occurring auxetic materials are scarce in the bulk, however, a small but growing group of 2D materials have been predicted to display this

phenomenon.[16] Auxeticity in 2D can either be displayed out-of-plane, in-plane, or bidirectionally (both in-plane and out-of-plane).[17-18]

Under large deformations (finite strains), visible changes in the shape or volume in a solid body are produced. From here, the resistance of solids against a loading condition (the type and direction of the induced deformation), can be calculated into the stress-strain curves, the most reliable and complete source for the evaluation of mechanical properties of materials. A material becomes mechanically unstable when a maximum value in the stress-strain curve has been reached, at this region, any subsequent perturbation will provoke a collapse in the integrity of the structure, leading into a structural phase transition or failure.[19] Anisotropy plays an important role in evaluating a solid at finite strains, as the mechanical instabilities are sensitive to the direction of the applied load,[20] even for hexagonal lattices.[6] 2D materials introduce excellent mechanical properties not seen in the bulk state,[21] their virtual atomic thickness, high in-plane cohesiveness, light mass and high crystallinity,[22] render them as promising candidates for strain-bearing applications.[23]

With the aid of powerful exploration algorithms and high-throughput computational methods, significant efforts have been put into predicting 2D phases from naturally occurring bulk structures,[24-25] to be then experimentally isolated and characterized. As well into designing many novel monolayered components with no known parent structure to be further synthesized.[26-28] In the second group it is possible to find BeH_2, a polymorphic monolayered crystal of exciting elastic properties.

Planar ultra-thin layered systems of BeH_2 were first conceptualized in 1989 by Seel *et al*.[29] Recently, Li *et al*.,[30] through a particle-swarm optimization (PSO) method,[31] predicted two thermodynamically stable phases of square and hexagonal lattices, labeled α-BeH_2 and β-BeH_2, respectively. The main difference between the predicted monolayers of Li *et al*., and Seel *et al*., is found in the out-of-plane distortions of the more recent individual layers, which reduces the lattice parameters and, do not display imaginary vibrational modes, which the flat layer does.[32]

In the work of Li *et al*., the structural, thermal, and dynamic stabilities of the ground-state for the α-BeH_2 and β-BeH_2 monolayers were first assessed. A large electronic band gap

of ~5 eV and multicentered bonds were predicted in both polymorphs, emphasizing on the structural stability of the monolayers. The linear elastic properties were also addressed, the monolayers exhibited stiffness values comparable to other 2D materials like germanene or Cu_2Si. Another relevant feature was an in-plane auxeticity predicted for α-BeH_2, with clear promise for mechanical applications.

The structural stability of the BeH_2 monolayers was discussed. The treatment of the infinitesimal strain response was given for an isotropic medium. These conditions are enough to describe the response to deformation in the hexagonal lattice of β-BeH_2, but they do not give a complete picture of the elastic response for the square lattice of α-BeH_2. Seen from the perspective of the unusual mechanical properties, the anisotropy of α-BeH_2 and its NPR are attractive features that have yet to be explored in detail. This polymorphic 2D crystal presents itself as an interesting case study, as it provides an exceptional window to quantify and distinguish how, from the choice of lattice, the crystal structure will tailor the mechanical response and the modes of failure of a compound with two different stable phases.

The general objective of this dissertation is to study, by means of first-principles computations, the mechanical response of the BeH_2 monolayers under the infinitesimal- and finite-strains regimes, and to determine their mechanical instabilities. Starting from the characterization of the monolayers' ground-state, analyzing their electronic structure and chemical bonding, estimating the interactions between layers produced at different bilayer stacking orders, and measuring the mechanical response in the infinitesimal-strains regime considering direction-dependent properties. As well as in the finite strains regime, estimating the response under uniaxial and biaxial tensile stress of the BeH_2 monolayers, calculating the ideal strengths in the stress-strain curves and localizing the phase transitions for each of the computed directions. The polymorphism of the selected material is of great interest, as each phase will behave differently when mechanically evaluated, this conduct will aid in understanding the microscopic origin for the auxeticity of α-BeH_2.

Therefore, this work is outlined as follows. The first Chapter presents a background on the characteristics that define a 2D material and cover the concepts of the mechanical properties in 2D materials; introducing an exotic elastic property, the negative Poisson’s

ratio. The Chapter also includes a brief summary on the current state of research for 2D BeH_2. The second Chapter is a preamble to the results, and it includes important information on the theory and methods behind the calculation of the linear-elastic and finite-strain properties of materials from first-principles computations. Chapter 3 presents the results on the atomic structure, the binding energies for several bilayered stacking orders, and the analysis of the electronic structure for the individual layers. The linear-elastic regime of the monolayers is also evaluated, with results on the direction-dependent elastic properties of the monolayers. The fourth Chapter presents the predicted finite-strains response of the BeH_2 single layers at biaxial and uniaxial tensile strains, calculating the ideal strengths, as well as their mechanical instabilities. The changes with strain in the structural parameters of the monolayers are also explored, aiming to understand the mechanism of the auxeticity in the α-BeH_2 phase. Finally, a brief Summary of the results is given followed by the Perspectives of this work.

1. Elasticity in 2D Materials: Background

1.1. Introduction

The existence of two-dimensional (2D) crystalline structures had been theorized decades ago and were deemed to be thermodynamically unstable for any temperature above absolute zero.[33-34] The works of Novoselov *et al.*,[3, 8] would radically change such a paradigm. Graphene, a carbon allotrope that consists of a single layer of atoms disposed over a hexagonal array, revealed impressive feats unseen before in the solid-state: such as a quantum Hall effect,[35] quantum confinement,[36] ultrahigh stiffness,[6-7] extremely high mobility[37] and a large specific surface area,[38] making it desirable for nanomechanical, environmental, and electronic applications, to mention a few. Graphene attracted enormous attention both in academia and industry. A revolution in materials research had begun, it was the dawn of 2D materials science.

Compounds of many shapes and chemical formulae started populating the flatland,[39-41] many of which trace back from bulk 3D predecessors and can be cleaved into few- and single-layered structures with relative ease. Some, however, would not be able to be isolated as effortlessly, as their interlayer interactions are of more significant magnitudes, limiting them to the best of cases, as substrate supported single-layers.[42-43]

Due to their atomic thickness, 2D materials come as natural candidates to exhibit remarkable mechanical properties.[21] With time, more techniques focused on synthesizing 2D materials began to appear, substantially increasing the number of experimentally available 2D solids. Unfortunately, experiments centered on analyzing the mechanical properties of 2D materials still present technical challenges to be overcome, but computational simulations have helped in predicting behaviors not yet accessible *in situ*.

With the aid of powerful exploration algorithms and high-throughput computational methods, significant efforts have been put into predicting 2D phases from naturally occurring bulk structures to be exfoliated from,[24-25] or into designing novel monolayered components

with no known parent structure which await synthesis.[26-28] Materials scientists now have the tools to computationally explore a wide variety of 2D systems, among which is BeH_2; a polymorphic 2D material with exciting elastic properties, of interest for this work. The exploration of the mechanical properties of 2D crystals serves a dual purpose, as these hold the baseline for the design of flexible, transparent, and composite devices,[23, 44] but also aid in the understanding of fundamental mechanics.

1.2. Layered and Non-layered 2D Materials

The isolation of graphene, a flat sheet of carbon atoms arranged in a hexagonal lattice (Fig. 1.1a) obtained from the exfoliated flakes of highly oriented pyrolytic graphite, cleverly loops around postulates held on the impossibility of obtaining 2D crystals at room conditions; as it is of finite size and displays out-of-plane fluctuations like a tethered membrane.[45-47] Therefore, although graphene may not be entirely two-dimensional, it is an atom-thick monolayer embedded in a higher-dimensional space, becoming the first layered 2D material.

The first wave of 2D materials also introduced some of the more representatives, with hexagonal boron nitride (h-BN) and MoS_2.[8] h-BN (Fig 1.1b) is a planar honeycomb lattice isostructural to graphene, very similar in lattice parameter as well, and it is thought of as an ideal partner for graphene electronics.[48] MoS_2 is pertinent to the family of the transition metal dichalcogenides (TMDs), a varied group of binary compounds of general formula MX_2; of these, the group-16 TMDs (M= Cr, Mo, W and X=S, Se, Te) are stable at room conditions.[49-50] TMDs crystalize in two polytypes (stacking orders), with the metallic center either having a trigonal prismatic (H=hexagonal) (Fig. 1.1c) or octahedral (T=trigonal antiprismatic) (Fig. 1.1d) environment. Most of the known 2D materials are of hexagonal symmetry,[51] their characteristic honeycomb backbone is patterned by two chiral directions, the armchair (nearest-neighbor) and zigzag (second-nearest neighbor) directions.

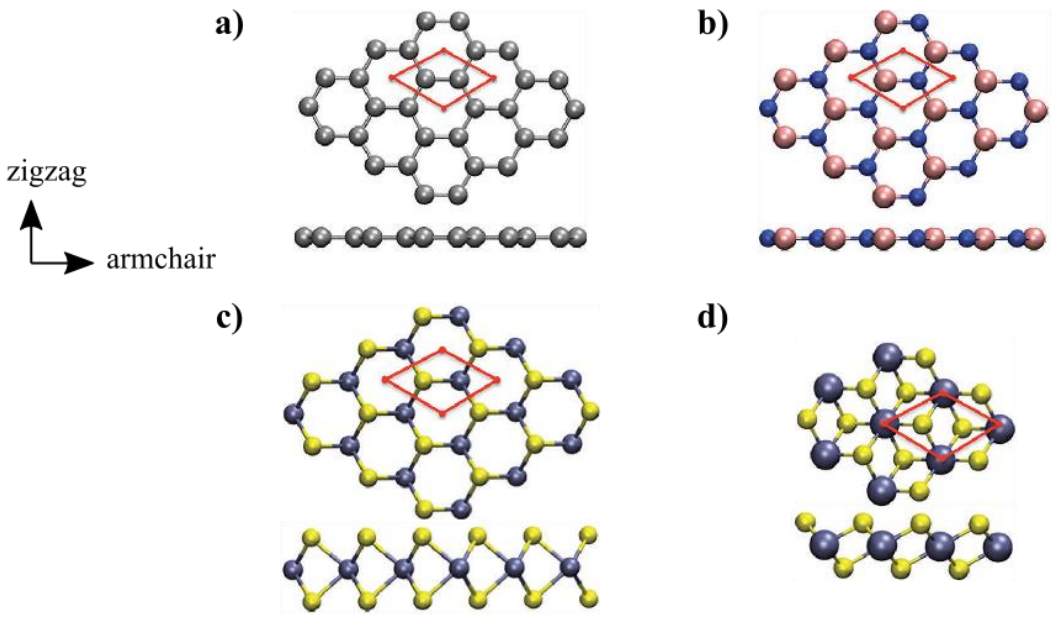

Figure 1.1 Atomically thin 2D materials. a) Graphene, b) hexagonal boron nitride (h-BN), c) hexagonal molybdenum disulfide (H-MoS_2), and d) (trigonal antiprismatic) T-MoS_2. The axes signal their chiral directions. Adapted from Ref. 50.

Graphene, h-BN, and MoS_2 are of the several layered 2D materials that can be cleaved from parent bulk structures (Fig. 1.2a). These layered 2D materials are known for their strong in-plane cohesiveness and slight out-of-plane crumpling, resulting in intrinsically stable structures.[46-47] In all, the properties procured by the layered 2D materials are far different and more enticing than those of their 3D counterparts.

Others, however, lack a 3D structure to be extracted from. The heavier group-14 allotropes of graphene, silicene, germanene, and stanene, fall in this category. Initially thought of as a logical choice for the development of nano-electronics, isolated 2D silicon and germanium become extremely volatile and unstable at room conditions.[42, 52] The ground-state of the heavier group-14 2D crystals (X-enes) deviates from the planar sp^2 hybridized structure of graphene and instead consists of a low-buckled honeycomb configuration,[53] given to the presence of a mixture of sp^2 and sp^3 hybridized states. This electronic disposition holds a significant role as silicene,[54-55] germanene,[56] and stanene[57] have shown evidence of growth atop metallic substrates (Fig. 1.2b). Where the contact produced between the X-ene layers and the metallic substrate is a strong bonding interaction that also influences the

properties of the monolayers; hence, earning the nickname of non-layered 2D materials. A workaround to reduce the effect of external factors in synthetic X-enes and increase their stability is to consider bilayered structures.[58] Yaokawa *et al*.,[59] passivated patches of bilayer silicene sandwiched in between CaF_2 layers, where sp^3 hybridized Si-Si tetrahedral bonds helped to stabilize the system.

The influence of stacking monolayers is also regarded for layered 2D materials. The dispersion van der Waals (vdW) forces responsible for allowing the mechanical exfoliation of 2D systems, also influence on the interaction produced between layered configurations. Layer stacking emerged as a new degree of freedom for the tuning and design of complex multi-layered heterostructures, as the hypothetical vdW array shown in Fig. 1.2c.[60] The resulting stacked bi- and multi-layers are brought together by a binding energy, the parameter that defines the strength of the interaction between monolayers. Several studies have been dedicated to the effects that different stacking orders will have on the binding energies of bilayered 2D materials,[61-63] finding that stronger binding energies will have repercussions on the interlayer distance and affect the intrinsic properties of the monolayers. On that note, binding energies of lower magnitudes will allow the monolayers to slide easily from one another, a much desired property for lubricative applications.[64]

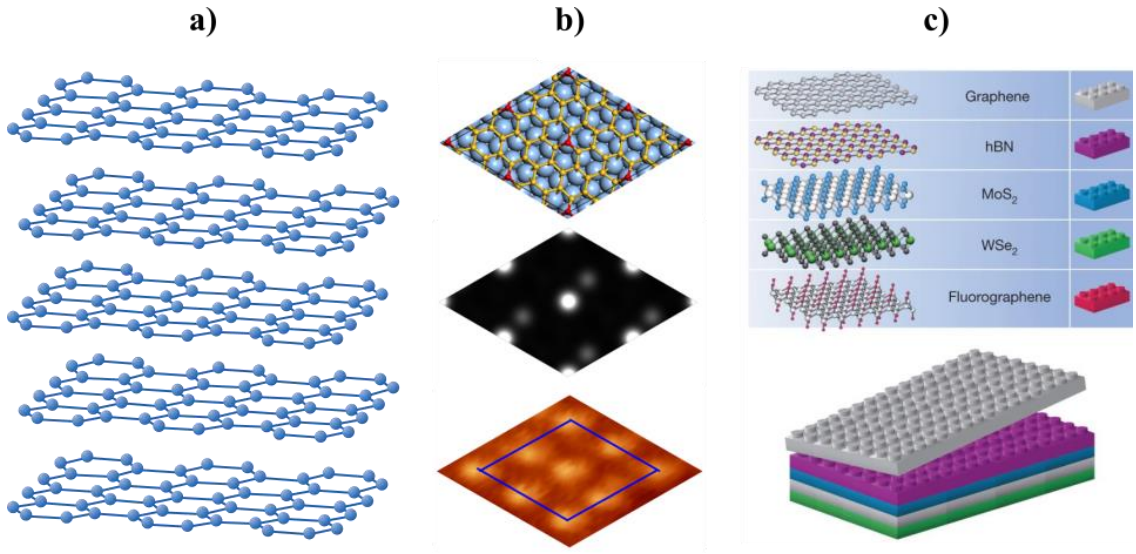

Figure 1.2. a) 3D layered graphite; b) (upper panel) Atomic structure of silicene on an Ag (111) substrate, (center) simulated and (lower) experimental STM images; c) hypothetical vdW heterostructure built from different 2D slabs. Adapted from Refs. 46, 52, 60.

1.3. 2D Materials Under Infinitesimal Deformations

The internal resistance against deformation in a material is known as the Young's modulus, or elastic modulus (E), it is a measure of the stiffness of solids. The produced deformation will affect in the perpendicular directions of the solid, which in turn can be measured by the Poisson's ratio (υ). These properties are essential to describe the response of 2D materials against external forces, and they can be obtained from inducing small distortions (infinitesimal strains) to the solid; the produced deformations are so small that the volume of the solid remains unchanged. In this region of small distortions, the behavior of most solids is linearly proportional, this is the linear-elastic limit. Within this limit, the elastic constants, fundamental units that determine the inherent response of a solid when stressed, can be obtained. In Fig. 1.3, a hexagonal 2D lattice is being pulled at one axis, a uniaxial loading condition; the response given by the material is measured by both the deformation parallel to ($\varepsilon_{\parallel}$) and the deformation perpendicular to ($\varepsilon_{\perp}$) the applied load. From these, the elastic modulus and Poisson's ratio can be estimated.

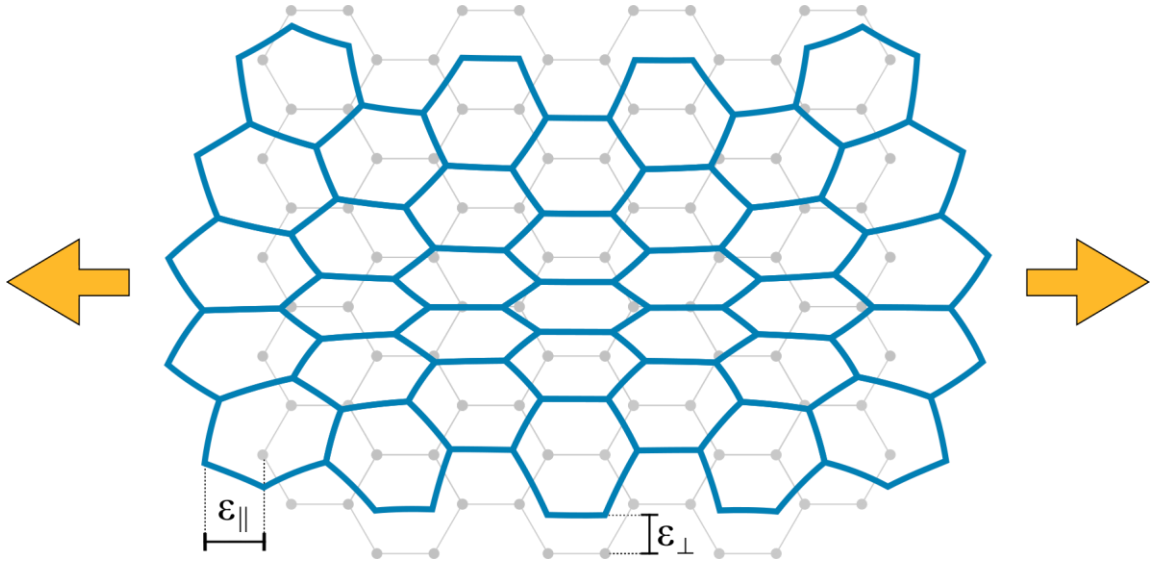

Figure 1.3. A uniaxial load is applied on a 2D hexagonal lattice. The original backbone is shaded in grey behind the blue structure deformed in the directions of the orange arrows. The changes produced in the geometry of the lattice can be characterized by the parallel ($\varepsilon_{\parallel}$) and perpendicular ($\varepsilon_{\perp}$) strains.

At an early stage of 2D materials research, graphene became the stiffest material known,[6-7] with a Young's modulus greater than 1.0 TPa. Interest from the scientific community on the elastic response of other 2D materials was quick to rise, as these became the object of study for applications in novel strain-resistant technologies and flexible electronics.[23, 44]

Anisotropy is another key feature of 2D materials, the rate of deformation and the elastic response will depend mainly on the lattice symmetry and the direction of the incoming load.[51] Assuming an isotropic medium is helpful to predict certain characteristics of a material, but it will not display a complete picture.[9] A good example of an anisotropic 2D material is single-layer black phosphorus,[65] here referred to as phosphorene (Fig. 1.4a).

Phosphorene is composed by a honeycomb lattice, similarly to graphene or h-BN, but in a peculiar puckering. The phosphorus atom in phosphorene adopts an sp^3 hybridization,[66] bonding with three adjacent phosphorus atoms taking up the three valence electrons of the atom. Direction-dependent electronic and elastic properties in phosphorene have been predicted.[67] The elastic response of phosphorene is heavily influenced by direction, as Young's modulus is closely at a 4:1 proportion (166 to 37 GPa) from zigzag to armchair directions (Fig. 1.4b).[20] Likewise, its Poisson's ratio is very sensitive to direction, with ν ranging from ~0.40 in the armchair, to ~0.93 in the zigzag direction, revealing this material has high traverse contractions.

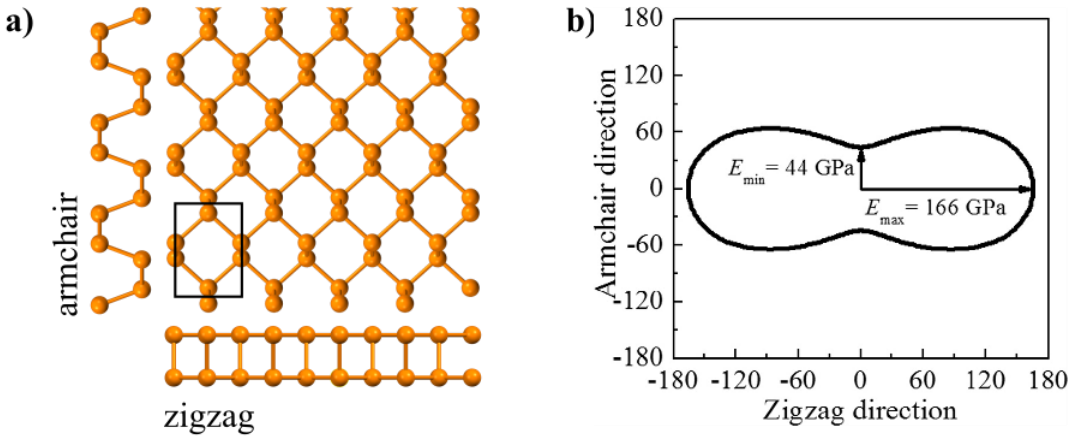

Figure 1.4. Atomic structure of phosphorene, a) top and side views of the armchair and zigzag directions; b) in-plane anisotropy of elastic modulus. Figure adapted from Ref. 20.

Generally, when a material is stretched, a contraction in the perpendicular plane will occur. While NPRs are not theoretically prohibited,[68] it was not until recently that this type of material was recognized. No structures with an NPR were verified until 1987,[12] when Lakes produced a metallic foam from a low-density open-cell polymer foam as a precursor. The ribs of each cell permanently protrude inwards (Fig 1.5a), resulting in a re-entrant structure. When the system is under mechanical tension, one of the hinges opens along the tensile axis, whereas the other hinge expands in the lateral direction, producing the NPR effect in the out-of-plane direction.

Evans *et al*.,[69] proposed a flat molecular network that could exhibit an NPR when stretched (Fig 1.5b). They would also coin the term auxetic, from the Greek *auxetos*: "that may be increased", for materials with transverse expansions. Thereon, a limited but varied group of materials like cubic metals,[70] lipidic membranes, and blood cell cytoskeletons[71] have been reported to express auxeticity in some form. Among the attributed properties of auxetics are improved indentation resistance,[72] fracture toughness,[73] and wave attenuation and steering.[74]

Auxeticity in 2D materials can be revealed in-plane, out-of-plane, or it can even appear in both directions (bidirectional). Phosphorene's puckered lattice effectively mimics the re-entrant mechanism proposed by Lakes, revealing an out-of-plane NPR of $\nu = -0.027$ (Fig. 1.5c). The auxetic behavior in phosphorene can be described by the interaction of two orthogonal hinges produced from the angle θ_{546} of atoms 4, 5 and 6, and the angle θ_{214} (or θ_{314}) from atoms 1, 2 (or 3) and 4. On applying tension in the zigzag (*x*) direction (Fig. 1.5c.i) the hinge θ_{546} is opened, which makes θ_{214} to close in the armchair (*y*) direction (Fig. 1.5c.ii), reducing the angle tilt and increasing the monolayer height.[13] This phenomenon was later experimentally confirmed,[14] becoming the first evidence of auxeticity in a 2D material.

Soon, more out-of-plane auxetic 2D materials were reported. Black phosphorus' allotrope, δ-phosphorene (Fig. 1.5d), revealed in-plane auxeticity.[75] Heavier Group 15 2D materials of the same backbone as black phosphorus, also exhibited out-of-plane NPRs.[76-77] Graphene has been predicted to display a transition into auxeticity on stretching in the armchair direction for strains larger than 6% (Fig. 1.5e),[78-79] and its hydrogenated allotrope,

B-graphane, is expected to exhibit small in-plane auxeticity.[80] An increasing number of highly anisotropic 2D materials began to emerge and populate the auxetic realm,[16, 18, 81] with some even being designed to reproduce the 2D re-entrant honeycomb structure (Fig 1.5f).[82] Table 1.1 presents data on some recently predicted auxetic 2D materials with the direction and magnitude of their NPRs.

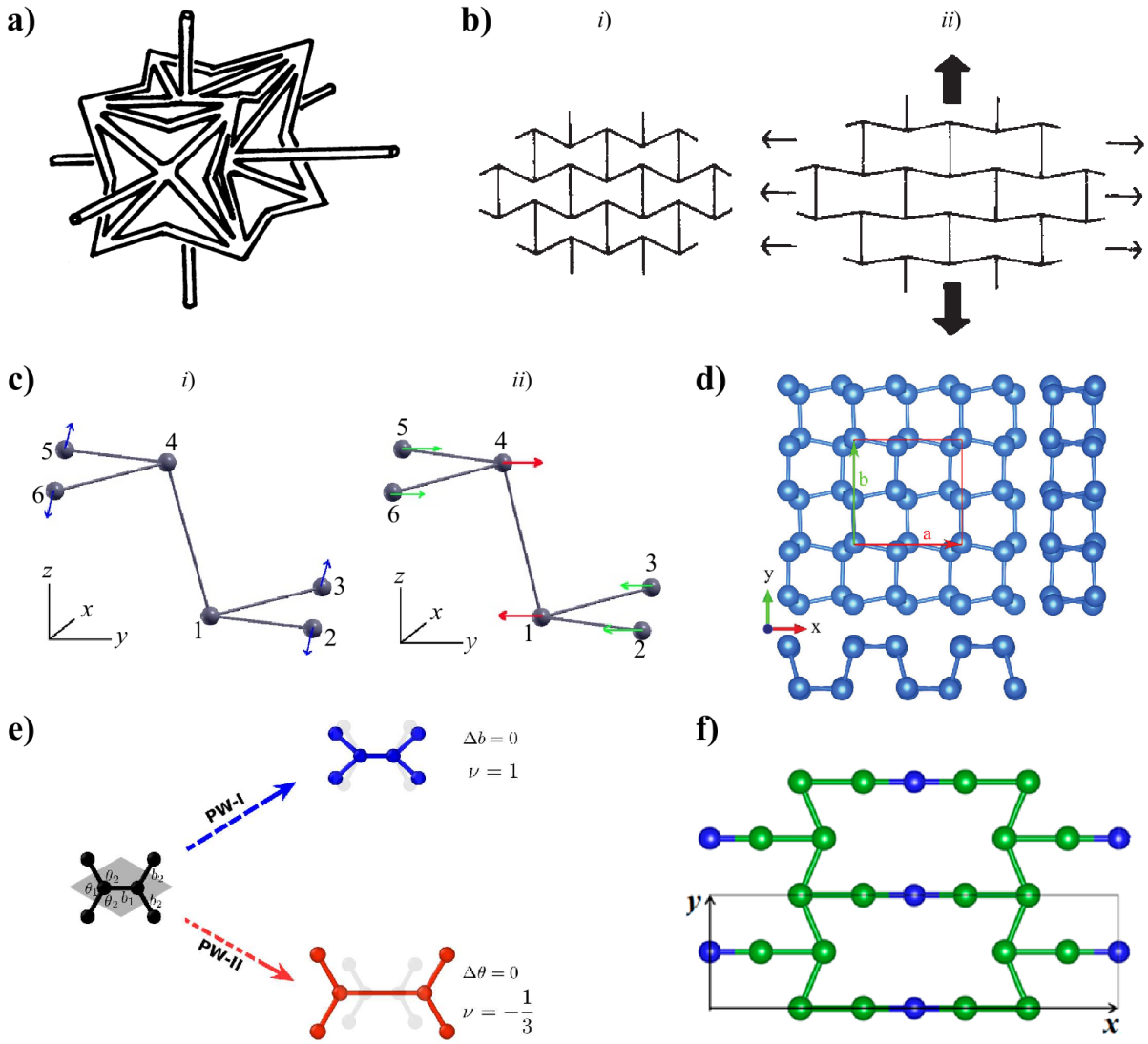

Figure 1.5. NPR materials. a) Idealized 3D re-entrant structure of the auxetic metallic foam; b) 2D re-entrant honeycomb lattice *i*) at rest, *ii*) when an axial load is applied to it; c) local environment of phosphorene *i*) at rest, *ii*) when a load is applied in the *x* direction, the orthogonal hinges come closer, reducing the tilt of angle θ_{124} and producing the out-of-plane NPR; d) atomic structure of δ-phosphorene, the black phosphorus allotrope with an in-plane NPR f) B_4N atomic structure, mimicking the re-entrant honeycomb lattice. Figures adapted from Refs. 12, 13, 69 75, 78 and 82.

Table 1.1. 2D materials of predicted NPR, their direction, and magnitudes. Directions given are parallel to the applied strain.

2D crystal	Direction	Magnitude
Phosphorene[13-14]	Out-of-plane	Zigzag: -0.03
Arsenene[81]	Out-of-plane	Zigzag: -0.12
B_4N[82]	In-plane	Armchair: -0.02, Zigzag: -0.03
B-Graphane[80]	In-plane	Armchair: -0.007, Zigzag: -0.006
δ-Phosphorene[75]	In-plane	Armchair: -0.16, Zigzag: -0.27
Graphene[78-79]	In-plane	Armchair: -0.03
Ag_2S[17]	Bidirectional	In: -0.12, Out: -0.52
$GaPS_4$[18]	Bidirectional	In: -0.03, Out: -0.62

1.4. 2D Materials Under Finite Deformations

Deformations that produce visible changes in the shape or volume in a solid body are inside the large deformations (or finite-strains) regime. The finite-strains regime measures the response of solids against an applied load until a state of failure is induced and can be projected into the stress-strain curves (Fig. 1.6), the most reliable and complete source for the evaluation of mechanical properties of materials.

The stress-strain curve is an important graphical tool that allows to measure and compare a material's resistance at a loading condition. In the early-strains portion of the curve, the elastic modulus of materials can be approximated. On entering the finite-strains regime, the ideal strength of materials can be calculated.

The ideal strength of a crystalline solid is the maximum strength of its perfect crystal configuration.[83] Certain conditions must be met to assess the ideal strength of a material, the system must be a perfect single crystal (void of defects and impurities) at its fundamental

state, at a uniform loading direction (axial, biaxial, multiaxial) and type (shear strain or tensile strain).

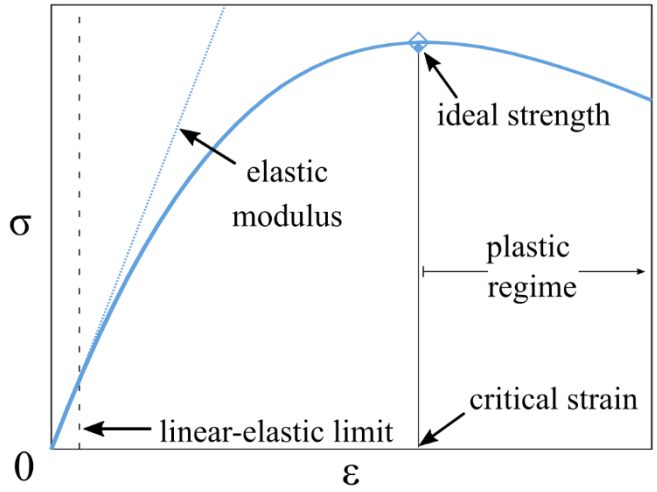

Figure 1.6. The stress-strain curve for a perfect crystal. The regions of importance are indicated by the arrows.

The ideal strength sets the upper boundary on the possible resistance any crystal can achieve, providing information on the stability and chemical bonding of materials.[84] The value of strain at which the ideal strength is located is called the critical strain. However, the ideal strengths for particular directions in some materials would not be determined by their critical strains, as some reports suggest, on phase transitions or failure modes becoming active before these values are reached.[85-86] Hence, limiting the ideal strength.

The structural deformations (change of buckling height, bond stretching, bond rotation, etc.) are reversible and the 2D crystal will return to its original configuration, as long as a state of meta-stability or mechanical instability is not exceeded.[19] In this region, any subtle perturbation will yield permanent changes on the configuration of the solid, and the accumulated strain energy is released in the form of dislocations or bond breaking in a process known as plastic deformation.

Experimentally, the mechanic properties of 2D materials are generally obtained in a process called nanoindentation, where the tip of an AFM cantilever will induce a condition of biaxial strain (equivalent deformation of the two in-plane axes) at a small region of the crystal, ultimately driving the membrane into failure.[87-88] At this point, the breaking strength

and strain are measured. A sample of smooth surface and a low density of defects can approach pristine conditions, and let the measured parameters be much in the vicinity to the values of their ideal tensile strengths. Unfortunately, experiments that analyze the elastic properties of 2D materials are still few, and computational simulations have helped in closing the gap by predicting behaviors not accessible *in situ*.

The elasticity of graphene was first addressed by Liu *et al.*,[6] predicting a large in-plane Young's modulus of 1.0 TPa, uniaxial strengths in the zigzag and armchair directions respectively, of 110 GPa and 121 GPa, and mechanical instabilities at deformations of ~0.20 and ~0.27 as seen in the stress–strain curves of Fig. 1.7, firmly placing graphene as one of the strongest materials known.

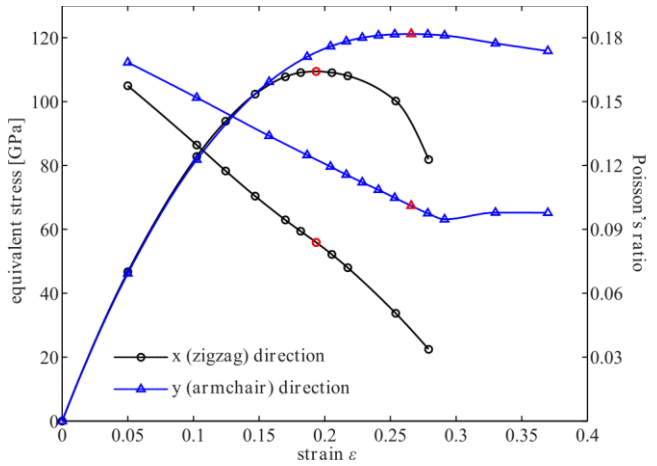

Figure 1.7. Stress-strain curves for the computational uniaxial tensile test of graphene. In blue the response of the solid in the armchair direction, in black, the resistance in the zigzag direction. The Poisson's ratios as functions of strain are also plotted, these being the descending slopes conserving the color scheme of the strengths. In red, the critical strains. Adapted from Ref. 6.

The experiments of Lee *et al.*,[7] were in line with earlier predictions, as breaking strengths of 130 GPa and fracture deformations of ~25% were reported for biaxially loaded graphene. Marianetti *et al.*,[89] computationally elucidated the failure mechanism in biaxially strained graphene; their results predicted that the instabilities occurring in the structure are due to the presence of imaginary frequencies at around 15% deformation, diverging from the reported breaking strain of 25%. A possible reason behind such disagreement is attributed to the chemical reaction between the graphene sheet and the AFM tip.

Naturally, focus on the elasticity of other 2D crystals was quick to arise. h-BN revealed a breaking strength of 70.5±5.5 GPa, and a Young's modulus of 0.865±0.073 TPa, much similar to the measured values of graphene.[90-91] Bertolazzi *et al.*,[92] and later Cooper *et al.*,[93] found that MoS_2 has a Young's Modulus of 270±100 GPa similar to alloy steel, breaking strengths of 22±4 GPa, and breaking strains of 6~11%, placing it as a suitable option for flexible electronics. Isaacs and Marianetti,[94] would find imaginary frequencies as the driving failure mechanism of both biaxially strained MoS_2 and h-BN. Thus, best practices call for the evaluation not only of the ideal tensile strengths, but also, of the instabilities and phase transitions that might occur when studying materials far from equilibrium.

Phosphorene has an ideal strength in the zigzag direction of 15~18 GPa, much higher than in the armchair direction, 6~8 GPa.[20, 95] The critical strain values would not be clear, though. While Jiang and Park[96] predicted ideal strains of 48% and 11% in the zigzag and armchair directions respectively, in another approach, Wei and Peng[20], computed them at 30% and 27%, for the zigzag and armchair directions. More recently, nanoindentation experiments on few-layered suspended phosphorene films,[97] yielded breaking strains ranging from 8~17%, closer in agreement to the computed maximum strains of 21% (armchair) and 15% (zigzag) by Tian, *et al.*[95] With no current experimental reports on the finite-strains response of monolayer phosphorene, it is relevant to consider, as Falin *et al.*,[90] noticed, that the mechanical response of 2D materials can be sensitive to the interlayer interactions of stacked systems.

In Table 1.2, the experimental elastic properties for the 2D materials above mentioned are summarized and paired with the values of known bulk materials of sturdy nature. The exploration of the mechanical properties of 2D materials serves a dual purpose, as these hold the baseline for the design of flexible, transparent electronics and composite devices, but also aid in the understanding of fundamental mechanics.

Table 1.2. Experimental values for the mechanic properties of materials in N dimensions (N=2,3).

ND	Material Name	Young's Modulus (GPa)	Breaking Strength (GPa)	Breaking Strain (%)
3D	Stainless Steel (ASTM-A514)[98]	205	0.83	15
2D	MoS_2[92]	270±100	22±4	8±3
3D	Tungsten carbide[99]	550	0.035	<1
2D	*h*-BN[90]	865±73	70.5±5.5	12.5±3.0
3D	Diamond (C)[100]	1050	~100	<1
2D	Graphene (C)[7]	1000±100	130	~25

1.5. The Case of Crystalline Beryllium Hydride

There is no knowledge of naturally occurring bulk beryllium hydride (or of any alkaline earth hydride for that matter). Thus, synthetic beryllium hydride (BeH_2) became into fruition in the 1950s;[101-103] the obtained metallic hydride was classified as a linear polymeric chain (1D) (Fig. 1.6a).[104] Some years later, BeH_2 attracted attention when the search for rocket fuels was on,[105] its elevated hydrogen storage percentage, low base metal density, and high heat of formation made it a considerable option as fuel propellants and hydrogen storage devices.[106-107] However, several factors made the earned interest to be dropped almost immediately, as there was not yet a proper way to synthesize BeH_2 of high purity, its cost was too elevated and most importantly, a severe risk of intoxication (berylliosis) was ever-present. The possibility of producing high-temperature superconductivity from hydrogen-dominant metallic compounds,[108] renewed interest in studying metallic hydrides at high pressures.[109-111]

A crystalline structure for BeH_2 appeared in 1988, when Smith *et al.*,[112] described for the first time the ground-state configuration of bulk BeH_2. This was a body-centered orthorhombic unit-cell containing 12 BeH_2 molecules; the crystal is arranged in a framework of corner-sharing BeH_4 tetrahedra arranged in an orthorhombic Ibam space group, No. 72 (Fig. 1.5b). No known analog among the tetrahedral network formers (BeF_2, SiO_2, GeO_2) displays this type of structure. Vajeeston *et al.*,[113] later predicted this variant as the least energetic compared to several proposed polymorphs and a stability up to hydrostatic pressures of ~7 GPa. Their computations also found this phase to have a large band gap of 5.5 eV at the generalized gradient approximation (GGA), and covalent interactions from wide valence mixture of Be *s, p* and H occupied states.[114] A more recent work discussed that the main reason behind the 3D ground-state remaining evasive for so long was due to the cohesive energies of polymerized and orthorhombic BeH_2 being so similar to one another.[115]

The 1D and 3D phases of BeH_2 have been theoretically and experimentally evaluated, the mandatory question would be: is there a 2D phase for BeH_2? Given the earlier stated, naturally-occurring phases of bulk BeH_2 are non-existent, and the only known crystalline 3D phase is not a reliable candidate to exfoliate thin layers from, as it is covalently bonded in all three Cartesian dimensions.

Early works on a BeH_2 monolayer (Fig. 1.5c) started with Seel *et al.*,[29, 116] and Wu *et al.*,[117] drawing inspiration from a flat slab of cubic perovskite $LiBeH_3$. This system became the topic of discussion, as the stability and electronic nature (metallic or insulating) were debated. Interest re-emerged in 2017 with the work of Yang *et al.*,[32] and their tight-binding (TB) model which predicted this monolayer as a semimetal of topological relevance; they would find out that this flat sheet revealed imaginary frequencies, thus, it was not a stable system.

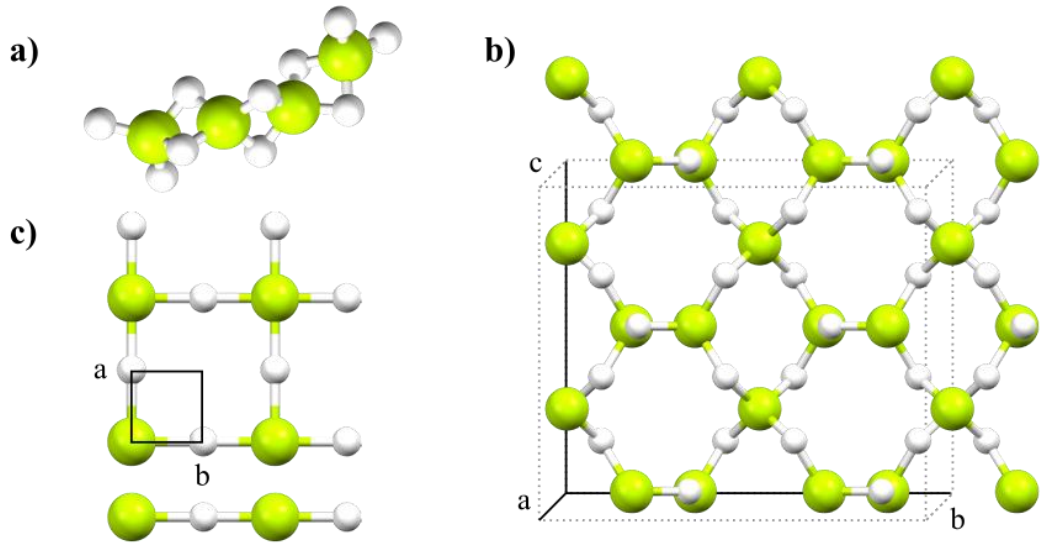

Figure 1.8. a) 1D polymeric linear chain of BeH_2; b) 3D crystal structure of BeH_2; c) 2D square flat lattice of BeH_2. With information from Refs. 28, 117 and 118.

In 2018, Li *et al.*,[30] ventured into the prediction and design of monolayered phases of BeH_2. Aiding from massive search algorithms that use the particle swarm optimization (PSO) method,[31] they proposed two thermodynamically stable polymorphs. These two phases exhibited square and hexagonal lattices (of D_{2d} and D_{3d} point group symmetries) and were respectively labeled as α-BeH_2 and β-BeH_2, where the α- prefix was assigned to the more energetically favored of the two. Li *et al.*, structurally characterized both BeH_2 monolayers, they predicted that the ground-state was not the flat slab earlier theorized by Seel *et* al., but rather atomic layers with out-of-plane distortions. Their kinetic and thermodynamic stabilities were computed, no imaginary frequencies were found and thermal reversibility up to 500 K was revealed. Both BeH_2 monolayers have large band gaps of ~5 eV at the GGA approach, cohesive energies of 2.76 eV/atom, and the bonding nature of these electron deficient crystals was addressed via the solid-state adaptative natural density partitioning (SSAdNDP)[120] technique, predicting the existence of a 3c-2e (3 center, 2 electron) and 4c-2e multicentered bonds for α-BeH_2 and β-BeH_2, respectively.

The linear-elastic properties in isotropic conditions were also calculated, elastic moduli of 60 Nm^{-1} and 85 Nm^{-1} were revealed for the α-BeH_2 and β-BeH_2 polymorphs, rendering them stiffer than silicene (71 Nm^{-1}) or germanene (42 Nm^{-1}). Also, a negative c_{12} elastic

constant was obtained for α-BeH_2, resulting in an in-plane NPR of -0.19, endorsing it as a compelling candidate for its potential applications in mechanics.

1.6. Open Problems

Two thermodynamically stable phases for single-layered BeH_2 have been computationally predicted. This 2D crystal presents itself as an interesting case study, as it is an excellent opportunity to understand how the morphology of the microstructure shapes the predicted properties of a compound with two different stable phases.

- Li *et al.*,[30] treated the linear-elastic properties in an isotropic medium, conditions that satisfy the hexagonal lattice of β-BeH_2, but the α-BeH_2 phase exhibits unusual mechanical properties which are inviting to be explored from many directions.
- The influence of strong interactions between layers can affect the structure and properties of individual layers. The results of Zhou *et al.*,[28] hold promise on the potential of obtaining free-standing monolayered metallic hydrides. Therefore, an estimation of the binding energies for several bilayered stacking orders can help predict if standalone individual layers of BeH_2 are within reach.
- The nature of the chemical bond also holds relevance. It is possible to gain insights from the superposition of occupied states and, from the atomic-pair interactions, compute an approximate value of their bond strengths.
- Accompanying the work on the infinitesimal-strains regime, it is suitable to cover the finite-strains regime as well. The ideal tensile strength is of interest, as it can provide information on the mechanical stability and instabilities of the BeH_2 monolayers. It is also possible for instabilities to become active before reaching the critical strain, therefore, it is important to address these situations as well.
- The α-BeH_2 phase exhibits auxeticity, while in β-BeH_2 it has not been registered. The mechanism on how the NPR is produced and how it modifies the structure of the monolayer has yet to be addressed.

2. Deforming Materials by Computations: Theory and Methods

2.1. Introduction

First-principles computations can reliably determine the number of basic material properties, like the elasticity of solid bodies. This is a crucial advantage, as it allows to estimate the mechanical stability and strength not only of known solids but also, of materials that have yet to be experimentally produced.

Elasticity is the property of materials to resist a distorting load and return to their original shape once said force is released. The intensity or degree of deformation a body is subjected to is known as strain, and the internal opposition of the body against deformation is known as stress. For a wide majority of materials, within a limit of small distortions, both stress and strain are linearly proportionally related by Hooke's law.

Hooke's law allows to calculate the elastic constants in a material, the fundamental units that determine the inherent response of a solid when stressed; all elastic constants can be extracted from ground-state total energy methods. The number of independent elastic constants is related to the symmetry of the lattice, and for most orders of symmetry, properties are direction-dependent. As loading conditions drift from the proportionality of Hooke's law, more properties of the material can be determined.

The stress-strain curve is the most reliable and complete source for the evaluation of mechanical properties of materials. The stress-strain curves help in understanding the elastic strength of a material, they show the resistance to deformation a material has against external forces and also reveal the difficulty of producing failure in the structure. A property of interest found only in stress-strain curves is the ideal strength, the maximum resistance of a pristine material at its ground-state. The focus of this Chapter is to introduce the mechanics background and the methodology used in this dissertation. The contents in the following sections draw from the texts in Refs. 51, 67-68, 99 and 121-122, for further consultation.

2.2. Strain and stress

The strain (ε) is a ratio that represents the displacement between particles in a solid body relative to a reference frame. In a state of equilibrium without the influence of an external field, an unstrained system is described by a set of vectors orthonormal to one another, $\hat{\mathbf{x}}$, $\hat{\mathbf{y}}$, $\hat{\mathbf{z}}$. After a slight, uniform distortion of the solid, the new vectors, **x'**, **y'**, **z'**, have undergone a modification in both their direction and magnitudes. These changes can be embodied in a system of equations of the form,

$$\mathbf{x}' = (1 + \varepsilon_{11})\hat{\mathbf{x}} + \varepsilon_{12}\hat{\mathbf{y}} + \varepsilon_{13}\hat{\mathbf{z}} \tag{2.1}$$

$$\mathbf{y}' = \varepsilon_{21}\hat{\mathbf{x}} + (1 + \varepsilon_{22})\hat{\mathbf{y}} + \varepsilon_{23}\hat{\mathbf{z}} \tag{2.2}$$

$$\mathbf{z}' = \varepsilon_{31}\hat{\mathbf{x}} + \varepsilon_{32}\hat{\mathbf{y}} + (1 + \varepsilon_{33})\hat{\mathbf{z}}, \tag{2.3}$$

where ε_{ij} ($i,j,$=1,2,3) quantify the deformation of a body in three dimensions, giving form to the strain tensor,

$$\varepsilon_{ij} = \begin{bmatrix} \varepsilon_{11} & \varepsilon_{12} & \varepsilon_{13} \\ \varepsilon_{21} & \varepsilon_{22} & \varepsilon_{23} \\ \varepsilon_{31} & \varepsilon_{32} & \varepsilon_{33} \end{bmatrix}. \tag{2.4}$$

Stress (σ) is the internal resistance of a solid body against an acting force measured on an element of the area. In a three-dimensional continuum, stress can be calculated in terms of nine quantities, three per plane, on three mutually perpendicular planes at a point. Herein, the Cauchy stress tensor, the response of the solid given at the current state of deformation, is reported,

$$\sigma_{ij} = \begin{bmatrix} \sigma_{11} & \sigma_{12} & \sigma_{13} \\ \sigma_{21} & \sigma_{22} & \sigma_{23} \\ \sigma_{31} & \sigma_{32} & \sigma_{33} \end{bmatrix}. \tag{2.5}$$

By considering a cubic element (Fig 2.1), which volume corresponds to an infinitesimal portion of an arbitrary solid in a state of unrest, the stress in the infinitesimally small system can be characterized by nine stress components acting on each j^{th} face at every i^{th} Cartesian direction.

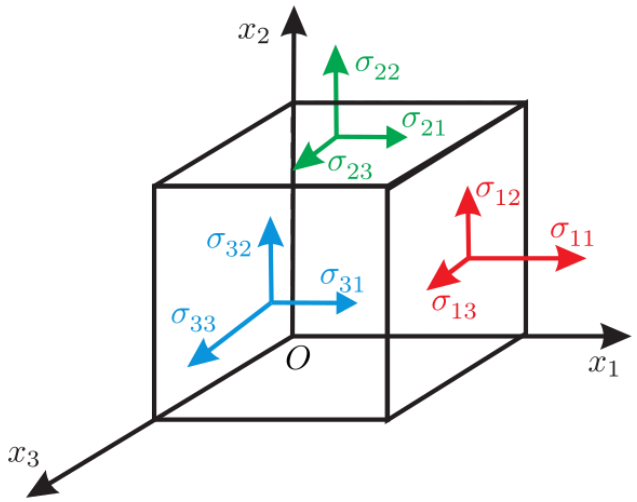

Figure 2.1. Geometrical representation of the Cauchy stress tensor, σ_{ij}. The σ_{ij} components represent the applied force on the j^{th} face of the volume along the i^{th} directions. Image adapted from Ref. 123.

2.3. Elastic Energy

In a state of thermodynamic equilibrium, the free energy of a system is a minimum. The energy of the system is also a function of the strain tensor, $E(\varepsilon_{ij})$. Then, a function of strain energy density per unit volume can be defined by,

$$U(\varepsilon_{ij}) = \frac{E(\varepsilon_{ij})}{V}. \tag{2.6}$$

The strain energy density function contains the complete information of the elastic response of a given material. In the limit of small deformations, the energy of the system can be expanded into a power series for the components of ε_{ij},

$$U(\varepsilon_{ij}) = U_0 + U^{(1)}(\varepsilon_{ij}) + \frac{1}{2}U^{(2)}(\varepsilon_{ij}{}^2) + O(\varepsilon_{ij}{}^3), \tag{2.7}$$

where U_0 is the energy density of the unstrained lattice, is $U^{(1)}$ is the linear term of the expansion that accounts for the residual stresses in a system, $U^{(2)}$ is the second-order expansion coefficient and $O(\varepsilon_{ij}{}^3)$ indicates that the neglected polynomial terms in the expansion are of order three and above.[120] Inside of $U^{(2)}$ is contained fundamental information on the behavior of the solid body when deformed, it can be expressed as,

$$U^{(2)}(\varepsilon_{ij}{}^2) = \frac{\partial^2 U(\varepsilon_{ij})}{\partial \varepsilon_{ij} \partial \varepsilon_{kl}} = C_{ijkl}, \tag{2.8}$$

where C_{ijkl} is the fourth-rank stiffness tensor. Thus, the stiffness tensor can be obtained from the second derivative of the strain energy density. And so, the strain energy density function for a deformed solid is given by,

$$U(\varepsilon_{ij}) = U_0 + C_{ij}\varepsilon_{ij} + \frac{1}{2}C_{ijkl}\varepsilon_{ij}\varepsilon_{kl}. \tag{2.9}$$

2.4. The Generalized Hooke's Law

Within the linear-elastic limit and through infinitesimal strains, both the stress and strain (for most materials) are proportionally related by Hooke's law,[68]

$$\sigma \propto \varepsilon. \tag{2.10}$$

The constitutive equation that binds these parameters is given by,

$$\sigma_{mn} = \frac{\partial U(\varepsilon_{mn})}{\partial \varepsilon_{mn}} = C_{ijmn}\varepsilon_{ij}. \tag{2.11}$$

So that, for a solid body, free of residual stresses and within linear-elastic conditions, the generalized Hooke's law is,

$$\sigma_{ij} = C_{ijkl}\varepsilon_{kl} \tag{2.12}$$

Both the stress and strain tensors are second-rank, having nine coefficients each. The stiffness tensor, then, would have 81 different components. The latter is true; luckily, the non-diagonal elements of the stress and strain tensors are related by symmetry: $a_{ij} = a_{ji}$, reducing to six independent coefficients in each tensor. There are now 36 values in the 6×6 stiffness tensor, that can be further reduced as,

$$C_{ijkl} = C_{klij}, \tag{2.13}$$

bringing the number down to 21 unique coefficients, the most any 3D anisotropic crystalline material can have,

$$C_{ijkl} = \begin{bmatrix} c_{1111} & c_{1122} & c_{1133} & c_{1123} & c_{1113} & c_{1112} \\ & c_{2222} & c_{2233} & c_{2223} & c_{2213} & c_{2212} \\ & & c_{3333} & c_{3323} & c_{3313} & c_{3312} \\ & & & c_{2323} & c_{2313} & c_{2312} \\ & & & & c_{1313} & c_{1312} \\ & & & & & c_{1212} \end{bmatrix}. \tag{2.14}$$

These stiffness coefficients are called the Second Order Elastic Constants (SOEC), and they are the fundamental units that determine the inherent response of a solid when stressed. First-principles computations that use periodic boundary conditions (PBC) assume the existence of a single crystal. Thus, all elastic constants can be extracted from ground-state total energy methods.

The tensorial notation is characteristic of crystalline symmetry, as it is very helpful in modeling the elastic response of solids in a Cartesian plane. The Voigt (engineering) notation is a method that aims to simplify the stress and strain tensors into 6×1 column vectors and the stiffness tensor into a square 6×6 matrix. By the combination of the pairs of indices as,

$$11 \rightarrow 1,\ 22 \rightarrow 2,\ 33 \rightarrow 3,\ 23 \rightarrow 4,\ 13 \rightarrow 5,\ 12 \rightarrow 6 \tag{2.15}$$

This matrix notation is widely used across materials' science, as it also will be used in this text.

2.5. Symmetry of 2D materials

There are five distinct types of 2D lattices, Fig. 2.2 summarizes the main characteristics that differentiate one lattice-type from another; *n*-fold rotational symmetry means that rotation by 360°/*n* will not change the structure or properties of the lattice. The number of elastic constants decreases with increasing order of symmetry.

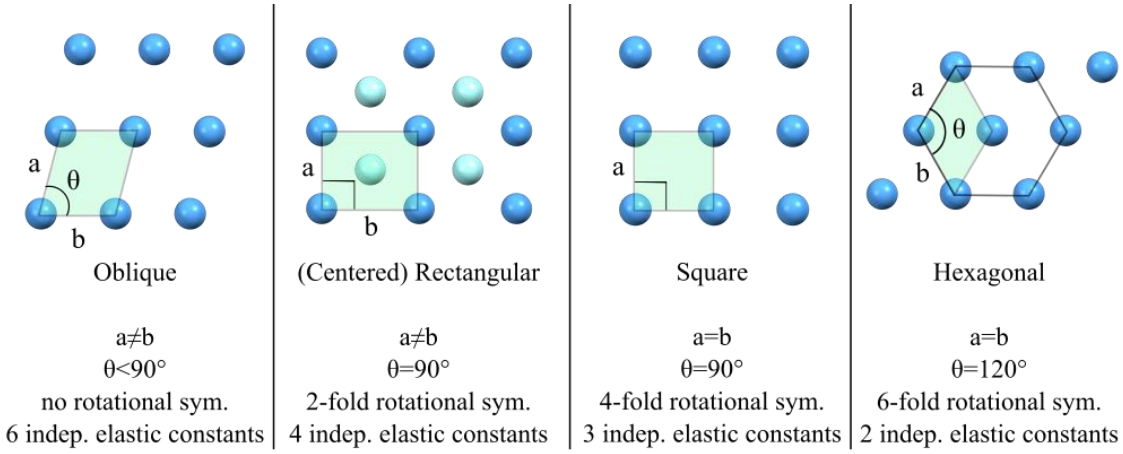

Figure 2.2. The different 2D lattices. The unit cell appears in the light-colored shade, along with the lattice parameters and bond angles. The second panel groups two types of lattices, the simple rectangular and the body-centered rectangular. In growing order of symmetry, the number of independent elastic constants reduces. Adapted from Ref. 51.

The 2×2 infinitesimal in-plane strain tensor is given by,

$$\varepsilon_{ij} = \begin{pmatrix} \varepsilon_1 & \varepsilon_6 \\ \varepsilon_6 & \varepsilon_2 \end{pmatrix}, \tag{2.16}$$

and in column vector form,

$$\varepsilon_{ij} = \begin{pmatrix} \varepsilon_1 \\ \varepsilon_2 \\ 2\varepsilon_6 \end{pmatrix}. \tag{2.17}$$

In a 2D crystal, the most anisotropic lattice consists of 6 independent elastic constants,

$$\begin{pmatrix} \sigma_1 \\ \sigma_2 \\ \sigma_6 \end{pmatrix} = \begin{pmatrix} c_{11} & c_{12} & c_{16} \\ & c_{22} & c_{26} \\ & & c_{66} \end{pmatrix} \begin{pmatrix} \varepsilon_1 \\ \varepsilon_2 \\ 2\varepsilon_6 \end{pmatrix}. \tag{2.18}$$

Notably, the stiffness tensor is discarded from any components in a third dimension, this is known as a state of plane-stress.[99] The third-dimension components of stress vanish at the surface due to the lack of external forces acting in that direction to balance them, more so if the specimen is very thin in this direction for stress to build up to an appreciable amount. This does not mean that the strain is unaccounted for, as there will be deformation in the thickness of the structure.

The next sections will deal with the cases of the square and hexagonal lattices, as these hold interest for the development of this work. The unit cell vectors for the square lattice are,

$$\vec{a}_1 = a_0 \hat{\mathrm{x}}_1, \qquad \vec{a}_2 = a_0 \hat{\mathrm{x}}_2, \tag{2.19}$$

where a_0 is the lattice parameter. The primitive cell vectors for the hexagonal lattice are,

$$\vec{a}_1 = \frac{1}{2} a_0 \hat{\mathrm{x}}_1 - \frac{\sqrt{3}}{2} a_0 \hat{\mathrm{x}}_2, \qquad \vec{a}_2 = \frac{1}{2} a_0 \hat{\mathrm{x}}_1 + \frac{\sqrt{3}}{2} a_0 \hat{\mathrm{x}}_2. \tag{2.20}$$

2.6. Infinitesimally Strained 2D materials

As seen in Section 2.3, the strain energy density function, U(ε), contains the necessary information to estimate the physical value of the independent elastic constants in a solid body. For a 2D material, a set of small, uniform in-plane deformations of the lattice are performed to describe the strain energy function. The applied loading conditions can be seen in Fig. 2.3. A biaxial strain (also known as in-plane hydrostatic) produces a change of area in the crystal; this deformation occurs in equal parts to both in-plane axial components of the 2D lattice. In uniaxial strain, the applied deformation is parallel to an in-plane axis, breaking the initial symmetry, and producing the Poisson effect. In shear strain, a volume conserving deformation takes place, with the lattice components being strained equally but at opposing directions.

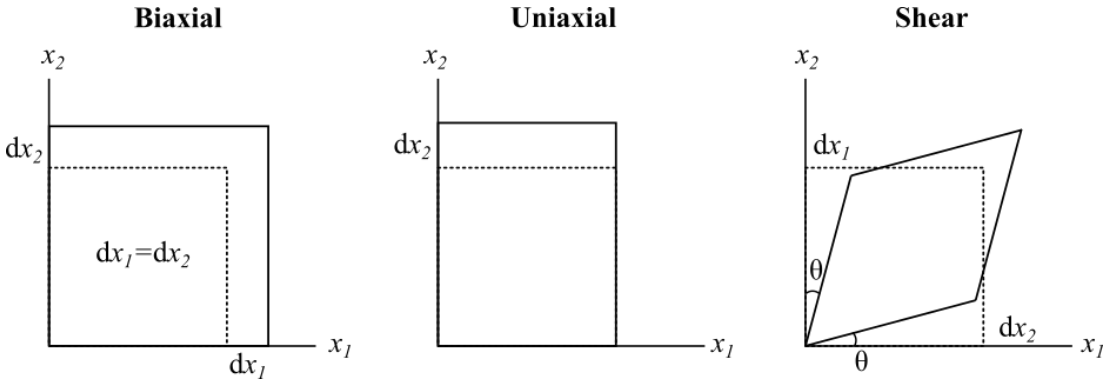

Figure 2.3. Infinitesimal strains approach to calculate the elastic constants of 2D lattices.

Thus, the infinitesimal in-plane strains on the square and hexagonal lattices are,

Biaxial strain

$$\varepsilon_{ij} = \begin{pmatrix} \xi & & \\ & \xi & \\ & & 0 \end{pmatrix}, \tag{2.21}$$

square lattice

$$\vec{a}_1 = a_0 \begin{pmatrix} 1+\xi \\ 0 \end{pmatrix}, \qquad \vec{a}_2 = a_0 \begin{pmatrix} 0 \\ 1+\xi \end{pmatrix}, \tag{2.22}$$

hexagonal lattice

$$\vec{a}_1 = a_0 \begin{pmatrix} \frac{1}{2}(1+\xi) \\ -\frac{\sqrt{3}}{2}(1+\xi) \end{pmatrix}, \qquad \vec{a}_2 = a_0 \begin{pmatrix} \frac{1}{2}(1+\xi) \\ \frac{\sqrt{3}}{2}(1+\xi) \end{pmatrix}. \tag{2.23}$$

Uniaxial strain

$$\varepsilon_{ij} = \begin{pmatrix} \xi & & \\ & 0 & \\ & & 0 \end{pmatrix}, \tag{2.24}$$

square lattice

$$\vec{a}_1 = a_0 \begin{pmatrix} 1+\xi \\ 0 \end{pmatrix}, \qquad \vec{a}_2 = a_0 \begin{pmatrix} 0 \\ 1 \end{pmatrix}, \tag{2.25}$$

hexagonal lattice

$$\vec{a}_1 = a_0 \begin{pmatrix} \frac{1}{2}(1+\xi) \\ -\frac{\sqrt{3}}{2}(1+\xi) \end{pmatrix}, \qquad \vec{a}_2 = a_0 \begin{pmatrix} \frac{1}{2} \\ \frac{\sqrt{3}}{2} \end{pmatrix}. \tag{2.26}$$

Shear strain

$$\varepsilon_{ij} = \begin{pmatrix} 0 & & \\ & 0 & \\ & & 2\xi \end{pmatrix}, \tag{2.27}$$

square lattice

$$\vec{a}_1 = a_0 \begin{pmatrix} 1+\frac{1}{2}\xi \\ -\frac{1}{2}\xi \end{pmatrix}, \qquad \vec{a}_2 = a_0 \begin{pmatrix} -\frac{1}{2}\xi \\ 1+\frac{1}{2}\xi \end{pmatrix}, \tag{2.28}$$

hexagonal lattice

$$\vec{a}_1 = a_0 \begin{pmatrix} \frac{1}{2} - \frac{\sqrt{3}}{2}\xi \\ -\frac{\sqrt{3}}{2} + \frac{1}{2}\xi \end{pmatrix}, \qquad \vec{a}_2 = a_0 \begin{pmatrix} \frac{1}{2} + \frac{\sqrt{3}}{2}\xi \\ \frac{\sqrt{3}}{2} - \frac{1}{2}\xi \end{pmatrix}, \tag{2.29}$$

where ξ is the magnitude of the strain.

In a defined range of infinitesimal strains, the computed curves of deformation allow obtaining the strain energy density difference function, ΔU(ε), of Equation 2.9. Plugging in for the infinitesimal deformations performed, the corresponding ΔU(ε) are,

Biaxial

$$\Delta U(\xi) = \sigma_1 \xi + \frac{1}{2} c_{11} \xi\xi + \sigma_2 \xi + \frac{1}{2} c_{12} \xi\xi$$
$$= (\sigma_1 + \sigma_2)\xi + \frac{1}{2}(c_{11} + c_{12})\xi^2, \quad (2.30)$$

Uniaxial

$$\Delta U(\xi) = \sigma_2 \xi + \frac{1}{2} c_{12} \xi^2, \quad (2.31)$$

Shear

$$\Delta U(\xi) = 2\sigma_6 \xi + c_{66} \xi^2. \quad (2.32)$$

From the second derivatives of the ΔU(ε) functions, it is possible to isolate and solve for the values of the elastic constants. The 3×3 stiffness matrix has been generated,

$$C_{ij} = \begin{pmatrix} c_{11} & c_{12} & 0 \\ c_{12} & c_{11} & 0 \\ 0 & 0 & c_{66} \end{pmatrix}, \quad (2.33)$$

the conditions of elastic stability for these lattices must meet the following criteria:

$$c_{11}{}^2 - c_{12}{}^2 > 0, \quad (2.34)$$

$$c_{66} > 0. \quad (2.35)$$

There is also the *Cauchy relation* for isotropic solids,[124] the expression $(c_{11}\text{-}c_{12})=c_{66}$ holds truth in 2D crystals. As seen in Fig. 2.2, hexagonal lattices have only two independent elastic

constants. It is relevant to mention that the elastic constants of 2D materials are measured in units of Nm^{-1}, from dividing values of energy over area. These can be converted into conventional units of Pascals (Pa), on considering that a component in the third dimension (the interlayer spacing) is missing.

Hooke's law (Eq. 2.12) states that the proportionality between stress and strain is linear under infinitesimal deformations. Therefore, for strain to be a function of stress,

$$\varepsilon_i = C_{ij}{}^{-1}\sigma_j = S_{ij}\sigma_j, \tag{2.36}$$

where the inverse of C_{ij} is the compliance tensor, S_{ij}. Which, in terms of the SOECs is,

$$S_{ij} = \frac{1}{\Delta}\begin{pmatrix} c_{11} & -c_{12} & 0 \\ -c_{12} & c_{11} & 0 \\ 0 & 0 & \frac{\Delta}{c_{66}} \end{pmatrix}, \tag{2.37}$$

with $\Delta = c_{11}{}^2 - c_{12}{}^2$. The relevance of the compliance tensor is that it can also be represented by the elastic modulus and the Poisson's ratio, which are easier to calculate through experiments.

2.7. Direction-dependent Properties

The reaction of solid bodies against external forces is dependent, for most symmetries, on the direction on which it is measured. The algebraic method to calculate the anisotropic response of 2D materials extracts from the doctoral thesis of Cadelano, E.,[122] and from the Supporting Information outlined in Wang *et al*.[67]

A uniaxial tension, σ, is applied to an arbitrary 2D lattice in the $\hat{n} = \hat{e}_{x1}\cos(\theta) + \hat{e}_{x2}\sin(\theta)$ direction, where $\hat{e}_{x1}$ and $\hat{e}_{x2}$ are the orthonormal vectors along the x_1 and x_2 axis (Fig. 2.4). The unit stress tensor along θ is,

$$\sigma_{ij} = \sigma \hat{n} \otimes \hat{n}, \tag{2.38}$$

$$\sigma_{ij} = \begin{pmatrix} \sigma_{x1x1} \\ \sigma_{x2x2} \\ \sigma_{x1x2} \end{pmatrix} = \sigma \begin{pmatrix} \cos^2\theta \\ \sin^2\theta \\ \cos\theta \sin\theta \end{pmatrix}. \tag{2.39}$$

A traverse vector to $\hat{n}$ would be in the form of $\hat{t}$= -$\hat{e}_{x1}$sin(θ)+ $\hat{e}_{x2}$cos(θ), so that $\hat{n} \cdot \hat{t}$ =0.

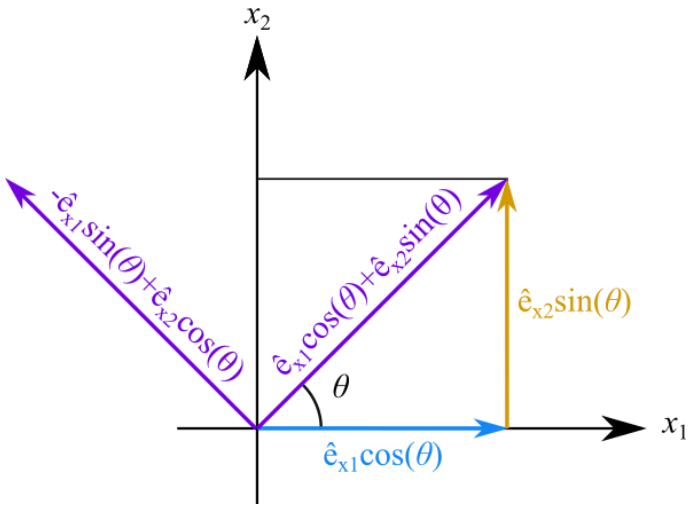

Figure 2.4. A uniaxial tension is applied at an arbitrary angle (θ) in a 2D lattice. The elastic response of the material is then defined by the variation of the components of strain in the compliance tensor, S_{ij}.

The strain components parallel to ($\varepsilon_{\parallel}$) and perpendicular to ($\varepsilon_{\perp}$) can be described accordingly by,

$$\varepsilon_{\parallel} = \hat{n}^T \varepsilon_{ij} \hat{n} = \sigma(\cos\theta \quad \sin\theta)\, S_{ij} \begin{pmatrix} \cos^2\theta \\ \sin^2\theta \\ \cos\theta \sin\theta \end{pmatrix} \begin{pmatrix} \cos\theta \\ \sin\theta \end{pmatrix}, \tag{2.40}$$

$$\varepsilon_{\parallel} = \sigma \left[\frac{c_{11}}{\Delta} (\cos^4\theta + \sin^4\theta) + \left(\frac{1}{c_{66}} - \frac{2c_{12}}{\Delta} \right) \cos^2\theta \sin^2\theta \right], \tag{2.41}$$

$$\varepsilon_{\perp} = \hat{t}^T \varepsilon_{ij} \hat{t} = \sigma(-\sin\theta \quad \cos\theta)\, S_{ij} \begin{pmatrix} \cos^2\theta \\ \sin^2\theta \\ \cos\theta \sin\theta \end{pmatrix} \begin{pmatrix} -\sin\theta \\ \cos\theta \end{pmatrix}, \tag{2.42}$$

$$\varepsilon_{\perp} = \sigma \left[\left(\frac{2c_{11}}{\Delta} - \frac{1}{c_{66}} \right) \cos^2\theta \sin^2\theta - \frac{2c_{12}}{\Delta} (\cos^4\theta + \sin^4\theta) \right]. \tag{2.43}$$

From the above equations (2.41) and (2.43) the direction-dependent elastic properties for 2D square and hexagonal lattices can be described. The relation for the elastic modulus is then given by,

$$E(\theta) = \frac{\sigma}{\varepsilon_{\parallel}} = \frac{\Delta}{\left[c_{11}(\cos^4\theta + \sin^4\theta) + \left(\frac{\Delta}{c_{66}} - 2c_{12}\right)\cos^2\theta \sin^2\theta\right]}, \quad (2.44)$$

and for the Poisson's ratio,

$$\upsilon(\theta) = -\frac{\varepsilon_{\perp}}{\varepsilon_{\parallel}} = -\left[\frac{\left(2c_{11} - \frac{\Delta}{c_{66}}\right)\cos^2\theta \sin^2\theta - 2c_{12}(\cos^4\theta + \sin^4\theta)}{c_{11}(\cos^4\theta + \sin^4\theta) + \left(\frac{\Delta}{c_{66}} - 2c_{12}\right)\cos^2\theta \sin^2\theta}\right], \quad (2.45)$$

where $E(\theta)$ is estimated by the ratio of the stress and the produced deformation parallel to the incoming force, and $\nu(\theta)$ is obtained by the negative of the ratio between the traverse and the parallel distortions of the solid. In isotropic conditions, the elastic modulus is simplified to,

$$E = C_{11} - \frac{{C_{12}}^2}{C_{11}}. \quad (2.46)$$

Similarly, the Poisson's ratio in isotropic conditions is given by,

$$\upsilon = \frac{C_{12}}{C_{11}}. \quad (2.47)$$

2.8. Finite Strains Regime

Hooke's law vanishes as the driving force strays from the proportional limit and enters the finite-strains regime. In first-principles computations, the ideal tensile strength is estimated by deforming the primitive cell in a series of incremental strains while simultaneously

relaxing the stress components perpendicular to the in-plane loading conditions. In this work, the ideal tensile strength for uniaxial and biaxial directions for the two phases of BeH_2 are computed.

The finite-strain vectors of the biaxially deformed 2D lattices are,

$$a_0 \begin{pmatrix} \vec{a}_1 x_1 & \vec{a}_1 x_2 \\ \vec{a}_2 x_1 & \vec{a}_2 x_2 \end{pmatrix} \begin{pmatrix} 1+\varepsilon & 0 \\ 0 & 1+\varepsilon \end{pmatrix} = a_0 \begin{pmatrix} \vec{a}_1(1+\varepsilon)x_1 & \vec{a}_1(1+\varepsilon)x_2 \\ \vec{a}_2(1+\varepsilon)x_1 & \vec{a}_2(1+\varepsilon)x_2 \end{pmatrix}, \quad (2.48)$$

where ε is the unitary applied strain. Similarly, at uniaxial loading, the finite-strain vectors are,

$$a_0 \begin{pmatrix} \vec{a}_1 x_1 & \vec{a}_1 x_2 \\ \vec{a}_2 x_1 & \vec{a}_2 x_2 \end{pmatrix} \begin{pmatrix} 1+\varepsilon & 0 \\ 0 & 1 \end{pmatrix} = a_0 \begin{pmatrix} \vec{a}_1(1+\varepsilon)x_1 & \vec{a}_1 x_2 \\ \vec{a}_2(1+\varepsilon)x_1 & \vec{a}_2 x_2 \end{pmatrix}. \quad (2.49)$$

In Eq. 2.49 strain has been applied in the x_1 axis, the same is possible for the x_2 axis, by switching the location of ε to the lower element of the diagonal. The Poisson effect is notable when stretching uniaxially; therefore, it is also necessary to perform several small distortions in the direction perpendicular to the applied strain, so that a minimum energy configuration for that value of strain can be found. The Poisson's ratios for uniaxial loading conditions can be calculated by,

$$\upsilon_{ij} = -\frac{\partial \varepsilon_j}{\partial \varepsilon_i}, \quad (2.50)$$

where ε_j is the strain in the perpendicular axis, and ε_i is the strain parallel to the axis of the applied loading condition.

The critical strain will be defined by the maximum value of the stress-strain curve. However, instead of only using primitive cells when calculating stress-strain curves, it is more convenient to employ supercells. The larger number of components found in supercells allow for the sampling of distinct possible structures that are far from the reach of unit cells,

due to the large symmetric constraints of the latter. An example of this is the response of graphene at equi-biaxial strains.

The work of Marianetti *et al.*,[89] dealt with the failure mechanism of strained graphene, and noticed that a supercell was able to reveal a phase transition before reaching the value of the ideal strength. Shown in Fig 2.5, the blue curve projects the strength of the primitive cell of graphene, while the red curve displays the response of the larger supercell with the phase transition becoming active before reaching its critical strain.

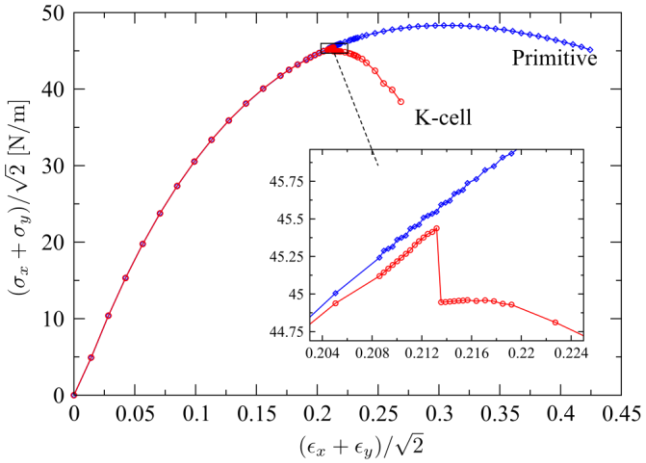

Figure 2.5. Stress–strain curve for the equi-biaxial strain test of graphene. In blue, the values for the primitive cell, and in red, the values for a supercell. The inset reveals the values of strain at which the supercell begins to separate, owing to instabilities that cannot be registered by the primitive cell. Adapted from Ref. 89.

2.9. Computational Details

The Density Functional Theory (DFT) computations reported in this work are based on the generalized gradient approximation of Perdew, Burke, and Ernzerhof (GGA-PBE),[125] as implemented in the Vienna *ab initio* Package (VASP).[126-127] The ion-electron interactions were treated using the projected augmented wave (PAW) method[128-129] that included semi-core states for the Be atom (Be_sv). A converged plane-wave cutoff of 600 eV was adopted for all computations.

For the ground-state and the infinitesimal-strain regime, the self-consistent cycle (SCF) would stop once the structure reached the energy convergence criterion of 10^{-8} eV/cell,

enough for optimization of lattice parameters and more precise estimation of the elastic constants, and the threshold for interatomic forces convergence during relaxation was set to 10^{-6} eV/Å. The sampling of the reciprocal space was first treated as a function of the second order elastic constants. The Γ-centered 20×20×1 and 18×18×1 *k*-mesh grids for the α-BeH_2 and β-BeH_2 phases, respectively, were adopted once convergence of the *k*-point–SOEC curves was considered optimal.

The simulation uses periodic boundary conditions for the two in-plane directions as well as the out-of-plane direction. Therefore, the computation will assume an infinite number of individual layers. Thus, a space in the out-of-plane axis of 15 Å was adopted, much larger than any other interlayer-spacing known, so that single layers and bilayers can be treated as isolated. To account for the weak interaction between layers, Grimme's DFT-D2[130] semi empirical correction method was implemented, opted due to the slight systematic overestimation of dispersion forces it gives.

The treatment of local bonding interactions was performed by adopting the projected Crystal Overlap Hamiltonian Population (pCOHP) technique as implemented in the Local Orbital Basis Suite Towards Electronic-Structure Reconstruction (LOBSTER)[131-134] software. The pCOHP scheme allows to project PAW functions onto localized orbitals and apply bond-analytic tools even though the system was brought to self-consistency in a plane wave basis, and analyze bonding, anti-bonding, and non-bonding interactions among pairs of atoms in the solid-state. Brought forward by Dronskowski and coworkers, COHP is a successor to Hughbanks and Hoffmann's Crystal Orbital Overlap Population (COOP)[135] approach. To perform the analysis, additional 2*p* basis functions for Be are involved, so that absolute charge spilling (that is, the percentage of electronic charge lost during projection) is in the 1~2% range. The integrated pCOHP (IpCOHP) value can be considered a measure of the bond strength, it is not an exact expression for the bond energy, but a good approximation.

For the finite-strain regime computations, the SCF cycles of the unit cells stopped at the 10^{-6} eV/cell convergence criterion, their atomic components were relaxed to 10^{-4} eV/Å, and the traverse stress tensor components relaxed to 10^{-3} GPa. The reciprocal space was sampled by Γ-centered 20×20×1 and 18×18×1 k-point meshes for α-BeH_2 and β-BeH_2,

respectively. The fully relaxed DFT unit-cell was then dilated in 1% increments to different levels of the applied loading conditions. After the application of each strain increment, the deformed structure was relaxed to a minimum energy configuration, while holding cell dimensions fixed. Stresses were computed in terms of force per unit area (Nm^{-1}) at the cross-sectional edges of the simulation cell and represent the true (Cauchy) stress components.

The energy convergence criterion for the 12 atom 2×2 supercells was set to 10^{-4} eV/cell, the interatomic forces were converged down to 10^{-2} eV/Å, and internal stress tensor components to 10^{-2} GPa. This time the Γ-centered reciprocal grids were accordingly sampled by 10×10×1 and 9×9×1 k-point meshes for α-BeH_2 and β-BeH_2. The mechanical instabilities in the 2×2 supercells were predicted by a method similar to that of Isaacs and Marianetti,[94] whereby introducing low randomized displacements ($\delta \leq |4|\%$) to the atoms composing the lattice and breaking the initial symmetry, the structure is left to relax.

The 27 atom 3×3 supercells were also evaluated. Luckily, every stress-strain curve and mechanical instabilities matched with the smaller 2×2 systems, thus, it is unambiguous that the mechanical properties of the BeH_2 monolayers have been treated with success.

3. Ground-state and Linear-elasticity of 2D BeH_2

3.1. Introduction

Herein, an assessment of the structural parameters and in-plane cohesiveness of both α-BeH_2 and β-BeH_2 is first performed. Grimme's D2[130] dispersion correction was used to describe the structural stability of the free-standing monolayers for several dimerized configurations. Very low interlayer interactions were computed, thus promoting both BeH_2 single-layers as stable standalone structures.

The electronic structure of the crystals is also addressed, the computed band-structures and density of states (DOS) reveal bandgaps of magnitudes in line to previous predictions. As well, an inspection on the chemical bond is performed, the projected Crystal Overlap Hamiltonian Population (pCOHP)[131-134] scheme is adopted to reveal the different pairwise bonding interactions of the crystals. The bonding strengths are also computed and, together with charge density difference plots, delocalized covalent bonds of high polarity are predicted.

The last segment of this Chapter covers the linear-elastic properties. The stiffness tensor of the BeH_2 monolayers is determined, and so are their direction-dependent elastic modulus and Poisson's ratio. Evaluating the anisotropy of α-BeH_2 to gain insights into the conditions of the lattice where auxeticity is displayed.

3.2. Atomic Structure

The primitive cell vectors of α-BeH_2 and β-BeH_2 are respectively,

$$\vec{a}_1 = a_0\hat{x}_1, \qquad \vec{a}_2 = a_0\hat{x}_2, \tag{3.1}$$

$$\vec{a}_1 = \frac{1}{2}a_0\hat{x}_1 - \frac{\sqrt{3}}{2}a_0\hat{x}_2, \qquad \vec{a}_2 = \frac{1}{2}a_0\hat{x}_1 + \frac{\sqrt{3}}{2}a_0\hat{x}_2. \tag{3.2}$$

The internal coordinates of their components are,

$$\alpha\text{-}BeH_2,\quad \begin{matrix} \text{Be: } 0,0 \\ \text{H: } \frac{1}{2},0 \\ \text{H: } 0,\frac{1}{2} \end{matrix} \tag{3.3}$$

$$\beta\text{-}BeH_2,\quad \begin{matrix} \text{Be: } 0,0 \\ \text{H: } \frac{1}{3},\frac{2}{3} \\ \text{H: } \frac{2}{3},\frac{1}{3} \end{matrix} \tag{3.4}$$

The lattice parameter, a_0, of α-BeH_2 is 2.41Å and of β-BeH_2, 2.32Å. Fig 3.1 shows the crystal structures of both BeH_2 monolayers. Note that the square lattice of α-BeH_2 has a D_{2d} point group (P-4m2) symmetry arranged in a network of Be centered tetrahedral units with H atoms at each extreme, with bond angles, $\theta_{H\text{-}Be\text{-}H}$, of 109.5°; while β-$BeH_2$ has a D_{3d} point group (P-3m1) symmetry, with six H first neighbors set in an octahedral (trigonal antiprismatic) environment at $\theta_{H\text{-}Be\text{-}H}$ = 90.0°±3.15°.

The predicted bond lengths (r) of the BeH_2 monolayers are longer than the theoretical values (r = 1.34 Å) of molecular[136] and polymeric[104] BeH_2. The bond length of α-BeH_2 is slightly larger than both values of r for the bulk crystalline phase[112] (r = 1.43 Å), and the theoretical 2D flat slab[116] (r = 1.46 Å), at r = 1.47 Å. β-BeH_2 has the largest known Be-H bond length to date (r = 1.60 Å).[30] The monolayers here discussed are not planar, as those first proposed by Seel,[116] rather, they display out-of-plane distortions of Δz= 1.68Å and Δz=

1.74Å, for the α-BeH_2 and β-BeH_2 phase, respectively. The computed structural parameters of both α-BeH_2 and β-BeH_2 are compared with the results by Li *et al.*,[30] in Table 3.1.

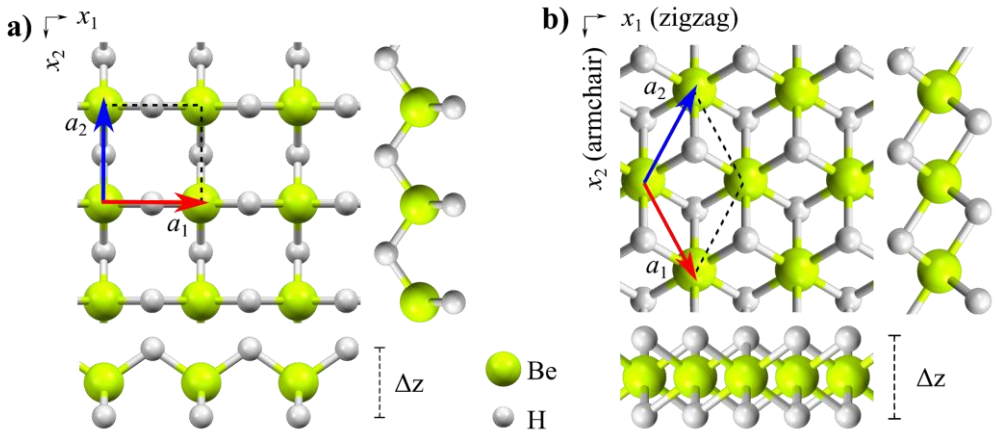

Figure 3.1. Crystal structures of a) α-BeH_2 and b) β-BeH_2. Δz is the out-of-plane distortion (buckling).

The square lattice is slightly more energetically favored than its hexagonal counterpart, with the former being lower in energy by ΔE=35 meV/unit cell. The in-plane cohesive energies (E_{coh}) were estimated by,

$$E_{coh} = \frac{n_{Be}E_{Be} + n_H E_H - E_{layer}}{n_{Be} + n_H}, \tag{3.5}$$

where n_x (x = H, Be) is the number of atoms for each element inside the single crystal and E_x (x=H, Be) are the energies for the atoms, and E_{layer}, the energy of each monolayer. The predicted values of E_{coh} are 2.69 eV/atom and 2.68 eV/atom for α-BeH_2 and β-BeH_2, respectively. The estimated values of E_{coh} are in accordance with the reported values of 2.76 eV/atom by Li *et al.*,[30] these are also discussed in Table 1, where the slight differences arise from the exclusion of dispersion correction methods. These values of bond strength are found slightly below the theoretical E_{coh} of planar hexacoordinate Cu_2Si[137] (3.46 eV/atom), and of black- and blue-phosphorene at 3.30 eV/atom and 3.38 eV/atom each,[138] but far from the E_{coh} of better known 2D materials like graphene (7.91 eV/atom)[139] and h-BN (7.07 eV/atom).[140]

Table 3.1. Structural parameters of the BeH_2 monolayers. Lattice parameters (a), H-Be bond length (r), out-of-plane distortions (Δz), H-Be-H bond angle (θ), energy difference (ΔE), and cohesive energies (E_{coh}).

System Name		a (Å)	r (Å)	Δz (Å)	θ (°)	ΔE (meV/cell)	E_{coh} (eV/atom)
α-BeH_2	Ref. [29]	2.38	1.46	1.68	109.4	14	2.76
	This work	2.41	1.47	1.67	109.5	34	2.69
β-BeH_2	Ref. [29]	2.30	1.59	1.75	90.0	-	2.76
	This work	2.32	1.60	1.74	90.0	-	2.68

3.3. A Free-standing Monolayer

In this work, the interlayer binding energies of several bilayered BeH_2 stacking orders are reported for the first time and depicted in Fig. 3.2. The proposed stacking orders for the bilayers follow the AA and AB configurations. AA stacking is produced where both layers are aligned so that a superimposed image is created, AB stacking has one of the layers shifted in-plane by half (one third) a unit cell for α-BeH_2 (β-BeH_2). Another variant is the mirroring image of the stacked bilayers, therefore, the AA' and AB' stacking orders are also evaluated. In summary, eight bilayered schemes are considered, their binding energies (E_{bind}) were determined using the following equation,

$$E_{bind} = \frac{E_{2L} - 2 * E_{1L}}{N}, \tag{3.6}$$

where E_{2L} is the energy of the bilayer, E_{1L} the energy of the free-standing monolayer, and N is the total number of atoms contained in the unit cell. A negative E_{bind} is an indicator of an attractive interaction.

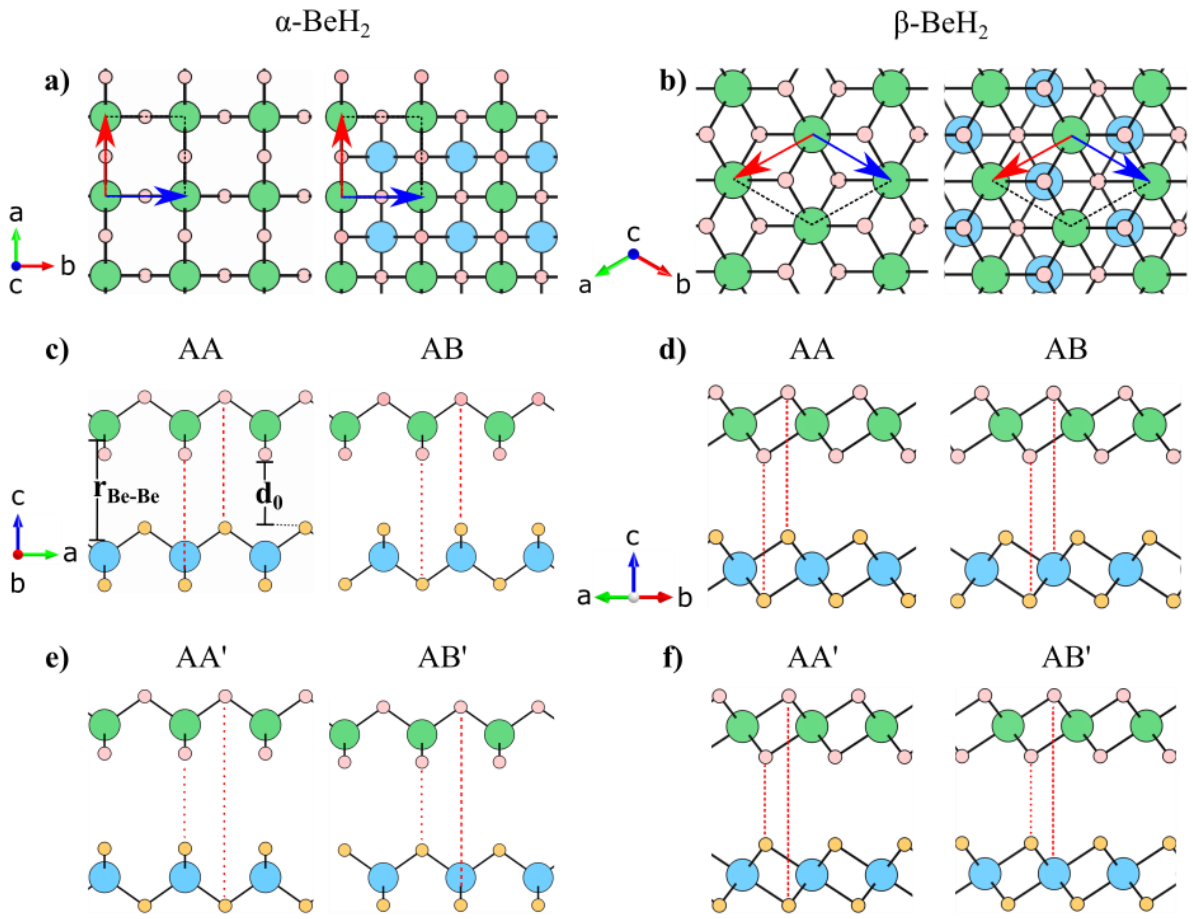

Figure 3.2. Top views for AA and AB stacking orders of a) α-BeH_2 and b) β-BeH_2 bilayers, respectively. Lateral views for AA and AB stackings of c) α-BeH_2 and d) β-BeH_2; mirror plane stackings AA' and AB' for e) α-BeH_2 and f) β-BeH_2. In dotted red lines, the vertically superposed atoms, the interplanar distance (d_0), and the Be-Be atomic distance (r_{Be-Be}).

The estimated binding energies are shown in Table 3.2. The DFT-D2 computations predict that both interlayer (d_0) and Be-Be atomic distances (r_{Be-Be}) are shortest in the AA stacking order. Hence, the strongest measured interactions for both polymorphs are found in the AA configuration, at E_{bind} 6.36 meV/atom and 8.11 eV/atom for α-BeH_2 and β-BeH_2, respectively. On comparing the obtained E_{bind} with previous reports on the interlayer interactions of graphite at several stacking orders using the same level, PBE/DFT-D2, graphene in its least energetically stable stacking order (AA), has an exfoliation energy of 41 meV/atom.[141]

The obtained binding energies are also in close agreement to the findings of Zhou *et al.*,[28] where 110 metallic hydrides ranging across the periodic table were proposed as stable 2D phases with potential for exfoliation from a bulk precursor. In such work, binding energies lower than $E_{bind} < 25$ meV/Å^2 (calculating the binding energies according to the in-plane area of the 2D crystal) were reported for the two BeH_2 polymorphs, in this convention, the binding energies for the BeH_2 bilayers here presented are $E_{bind} < 10$ meV/Å^2; the main difference being the choice of dispersion correction method, since the results of Zhou *et al.*, adopted the optB88-vdW functional.

The low energetic interactions between BeH_2 layers may promote them as desirable materials for tribological applications.[64] Besides, the out-of-plane distortions and lattice parameters are virtually unchanged from the monolayer configurations. Also, both d_0 and r_{Be-Be} are far from one another to generate any significant interaction. Therefore, it can be expected that both polymorphs of BeH_2 to be free-standing stable monolayers.

Table 3.2. Structural parameters for the considered BeH_2 bilayers. Lattice parameter (a_0), buckling (Δz), Be-Be atomic distance (r_{Be-Be}), interlayer space (d_0) and binding energies (E_{bind}).

Stacking Order	α-BeH_2					β-BeH_2				
	a_0 (Å)	Δz (Å)	r_{Be-Be} (Å)	d_0 (Å)	E_{bind} (meV/atom)	a_0 (Å)	Δz (Å)	r_{Be-Be} (Å)	d_0 (Å)	E_{bind} (meV/atom)
Monolayer	2.30	1.69	-	-	-	2.32	1.75	-	-	-
AA	"	"	3.87	2.18	-6.36	"	"	3.99	2.24	-8.11
AA'	"	"	4.50	2.81	-4.04	"	1.74	4.25	2.51	-6.21
AB	"	"	4.00	2.31	-4.21	"	1.75	4.00	2.25	-7.84
AB'	"	"	4.39	2.70	-4.22	"	"	4.25	2.50	-6.26

3.4. Electronic Structure and Chemical Bonding

Earlier works[113-114] on the electronic properties of the bulk BeH_2 ground-state computed forbidden energy gaps of 5.5 eV at the GGA-PBE level, with Be and H electrons mixing in the occupied states, signaling covalent bonding. Li *et al*.,[30] after relaxation at the GGA-D2 approach, also predicted large band gaps of 4.68 eV and 4.88 eV for α-BeH_2 and β-BeH_2, respectively. The BeH_2 monolayers do not follow classical chemical bond rules, rather, these electron-deficient systems are bonded together by multicentered bonds. The 3c-2e (3 center 2 electron) bonds in α-BeH_2 and 4c-2e bonds in β-BeH_2 were considered by Li *et al*., as responsible for the high structural stability of the individual layers.

Here, the electronic properties and chemical bonding of the BeH_2 monolayers are also given interpretation. The computed electronic bandgaps at the GGA-PBE ground-state for α-BeH_2 and β-BeH_2 are 4.58 eV and 4.84 eV, respectively; these values are in close agreement to earlier predictions. The respective band-structure and density of states (DOS) are presented in Figs. 3.3a and 3.4a. The valence band maxima (VBM) and conductance band minima (CBM) in α-BeH_2 are shown to be along the M→Γ and Γ→X paths, respectively. The VBM and CBM of β-BeH_2 occur at the Γ→K and M→Γ lines. The large forbidden energy gaps may also account for the stability of single layers against strong interactions from other layers.

Bulk BeH_2, as discussed by Vajeeston *et al*.,[113] has degenerate Be 2-*s* and H 1-*s* states in the occupied states energy range with a finite electron distribution between the Be and H atoms, reflecting covalent interaction contrary to the heavier ionic alkaline-earth hydrides. Moreover, a substantial hybridization of Be *p* states has also been reported for this structure.[110] The former is partly attributed to the atomic radii of Be and H being more related one another than to the heavier group 2 metals, but also because the outer electronic shells of Be and H are closer in energy, allowing for hybridized states. The DOSs of α-BeH_2 and β-BeH_2 are also integrated by a wide valence band (Fig. 3.3a and 3.4a), and the electron count in the outer shells sums to four, discarding any involvement of the innermost shell. The atom-projected DOS (pDOS) displays the internal mixing of H and Be states, shown as diffuse

curves intertwined for most of the occupied energy levels. The individual contributions of the atomic orbitals in α-BeH_2 and β-BeH_2 are shown respectively in Figs. 3.3c and 3.4c. The lower levels of the pDOS diagrams depict the presence mostly of *s* states of beryllium, and to a lower degree, of H and the in-plane *p* states. As a side note to the reader, the p_x and p_y states have been merged and renamed as in-plane *p* states (p_{ip}), for ease of interpretation and because the information provided individually is the only variant on rotation of the interacting contact. On approaching the Fermi level, E_F, jagged peaks of Be *p* and H *s* states can be found.

However, to get a clearer image of the bonding interactions within the monolayers, the projected Crystal Overlap Hamiltonian Population (pCOHP)[131-134] technique was adopted. Whereas the pDOS provides insight into the probability of finding an electron in an atomic orbital as a function of energy, pCOHP enables to evaluate whether the electron is at bonding, non-bonding, or anti-bonding state in a given atomic pair. The bonding interactions lower the energy of the system, as a convention a negative sign is attached to pCOHP functions, so that bonding states remain in the positive values of the plot and anti-bonding states on the negative side; non-bonding contributions are valued zero. The integrated curves of pCOHP, IpCOHP, up to E_F are a measure of the bond strength. The delocalized electrons in the valence states of α-BeH_2 and β-BeH_2 involve multiple overlaps for the Be-H contacts, and in lower measure, for neighboring Be-Be pairs as well.

The -pCOHP scheme finds a total of eight pairwise interactions for a Be atom in α-BeH_2 (Fig. 3.3b), distributed along the four bonding directions of the lattice. The computed interactions of the Be-Be and Be-H contacts are shown in Fig. 3.3d and Fig. 3.3e, respectively. At the lower energetic levels, Be *s* states are binding to Be *s*, $p_{ip,}$ and H states. On nearing -2 eV, bonding p_z states briefly emerge, together with p_{ip} contacts to other *p* and H states. The VBM is filled almost completely by in-plane *p* and H bonding states.

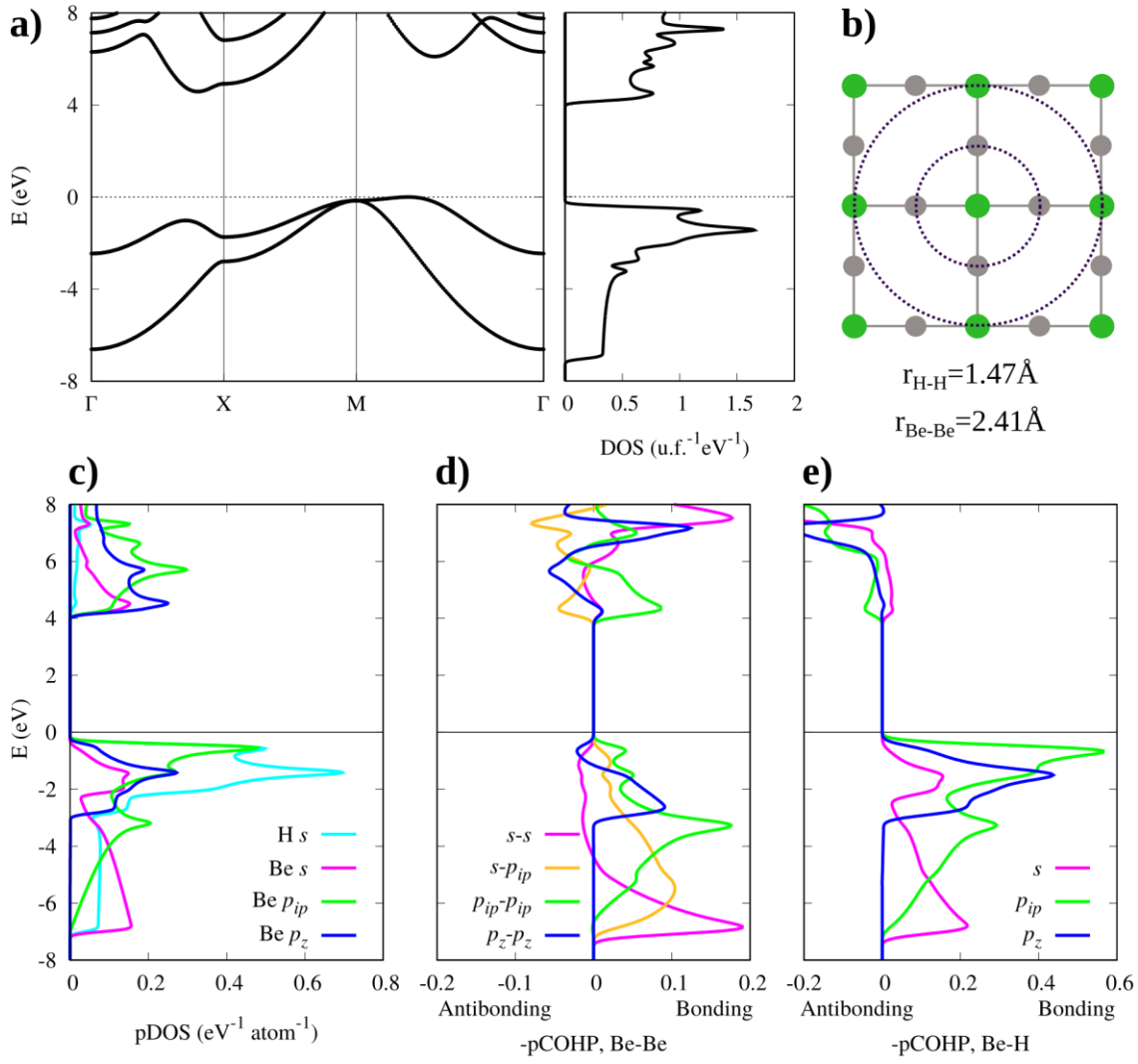

Figure 3.3. Electronic structure of α-BeH_2 a) Band structure and DOS with Fermi level assigned at 0 eV, b) Top view of the β-BeH_2 lattice with the eight interacting contacts of a centered Be atom encircled, lengths (r) for the Be-Be and Be-H contacts; c) pDOS, d) and e) -pCOHP of Be-Be and Be-H interactions.

In β-BeH_2, a Be atom has twelve contacts, six of each in alternating order (Fig. 3.4b). The bonding character is similar to α-BeH_2 in the lower occupied states (Figs. 3.4d and 3.4e), Be *s* states binding to Be *s*, $p_{ip,}$ and H states. Close to the -5 eV level, sharp *p* bonding states arise for both Be-Be and Be-H contacts. The VBM reveals small Be-Be antibonding interactions, and also, Be-H bonding peaks involving all available Be *s* and *p* states.

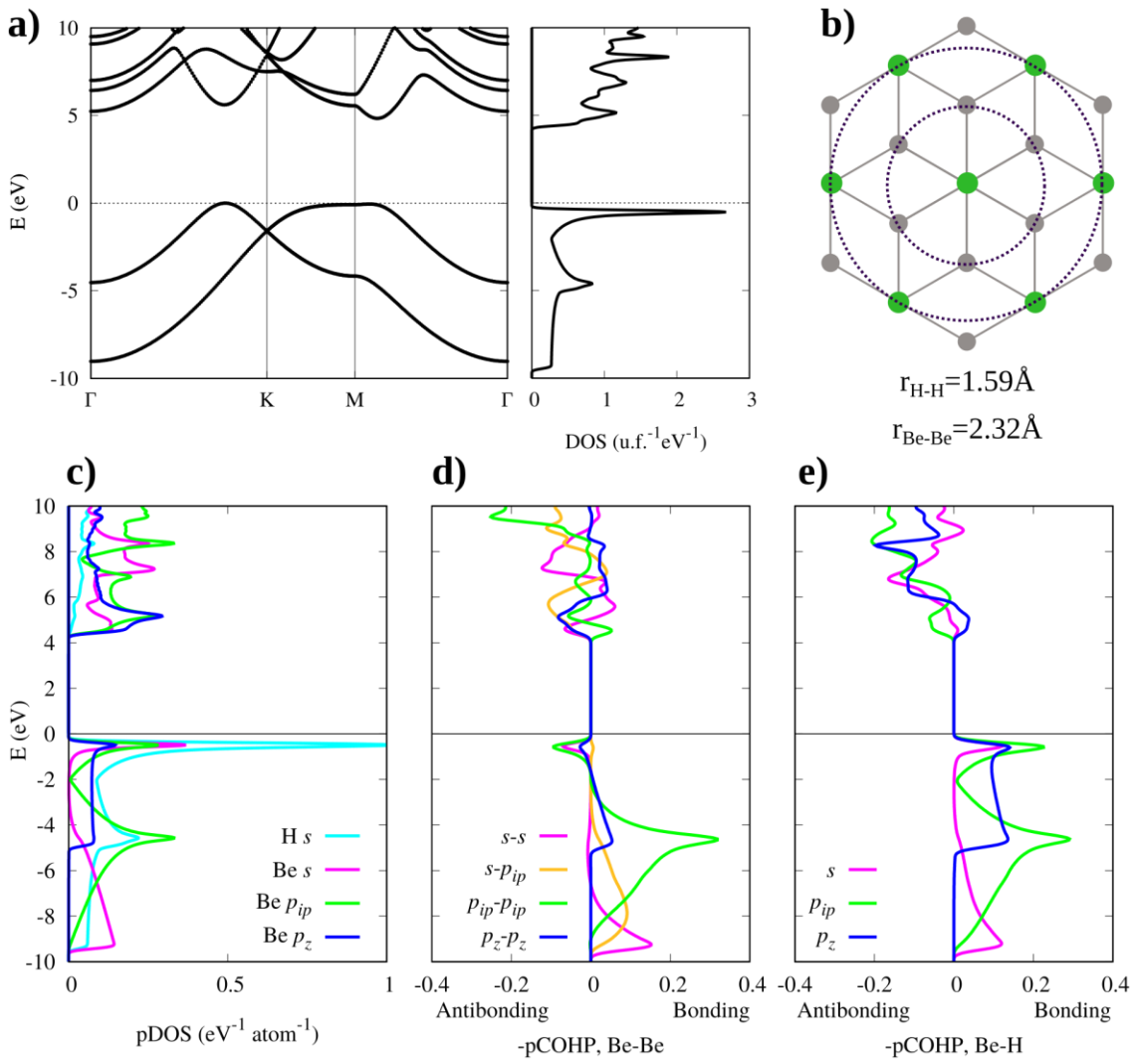

Figure 3.4. Electronic structure of β-BeH_2 a) Band structure and DOS with Fermi level assigned at 0 eV, b) Top view of the β-BeH_2 lattice with the twelve interacting contacts of a centered Be atom encircled, lengths (r) for the Be-Be and Be-H contacts; c) pDOS, d) and e) -pCOHP of Be-Be and Be-H interactions.

Most of the involved bonding contacts shown in the -pCOHP curves for α-BeH_2 and β-BeH_2 are found in the energy interval from -2 eV to E_F. At that same energy range, bonding Be-Be interactions vanish, and Be-H contacts reach bonding maxima. The computed IpCOHP up to the highest occupied band reveals bond strengths in α-BeH_2 of 1.33 eV for the Be-Be pairs, and of 2.70 eV for the Be-H bonds, a value similar to the calculated E_{coh} of 2.69 eV/atom in Section 3.2. The computed bond strengths in β-BeH_2 are 1.46 eV and 1.80 eV for the Be-Be and Be-H pairs, respectively. The IpCOHP values imply that the Be-H bond in α-

BeH_2 is stronger than in β-BeH_2. By inspecting Figs. 3.3e and 3.4e, it can be seen that the pCOHP curves in α-BeH_2 have a larger density of bonding states than those of β-BeH_2, translating into a greater bond strength when integrated. The shorter Be-H bond lengths in α-BeH_2 (r = 1.47Å) may be playing an important part in the bond strength, with the longer Be-H bonds of β-BeH_2 (r = 1.60Å), limiting its bond strength.

Although the pCOHP technique can only provide measurements for pairwise interactions and not many-particle contacts, one can intuitively elaborate a bonding scheme by considering the overall bonding states in place; no H-H interacting contacts are registered, therefore, H can serve as a starting point. According to the -pCOHP curves of Figs. 3.3 and 3.4, all pairs of similar natures share the same bonding scheme. Hence, in α-BeH_2, the charge is split in equal parts for an H atom with two neighboring Be atoms, and for each Be atom paired to 4 H atoms, its charge also splits uniformly. The result is a tri-atomic cloud with an electron density of 2*e*. For β-BeH_2, H has three Be neighbors, and these have a total of six H contacts. The binding enclosure forms a tetra-atomic region with an electron population of 2*e*.

The charge density difference technique allows visualizing how the electrons in a compound move with respect to a starting position. From the overlapping free atomic (o.f.a.) orbitals to the charge densities in a constituted solid, it is possible to gain insight on the chemical bond occurring in the material. The charge density difference, $\Delta\rho$, can be extracted from,

$$\Delta\rho = \rho_{comp} - \rho_{o.f.a}, \tag{3.7}$$

where ρ_{comp} is the charge density of the compound once the SCF cycle has converged.

The charge density difference maps of Fig. 3.5 reveal the electronic concentration in α-BeH_2 and β-BeH_2. The minimum values of the scale in white reveal the zones depleted of charge (Figs. 3.5a and 3.5b) belonging to the Be atoms. The darkened areas have a higher charge density (Figs. 3.5c and 3.5d) and show that the electronic charge is concentrated mainly around the H nuclei, but also, that the produced covalent interactions do not follow

the 2c-2e convention. As Li *et al.*,[30] have proposed, the chemical bond of the BeH_2 monolayers is described by the formation of multicentered bonds. From Figs. 3.5c and 3.5d, and gathering from the above IpCOHP analysis, a 3 center 2 electron (3c-2e) "banana bond", with two Be atoms and one H atom, is generated in α-BeH_2; as for β-BeH_2, a 4c-2e bond with one H atom and three Be atoms leasing most of their electron density, is best described.

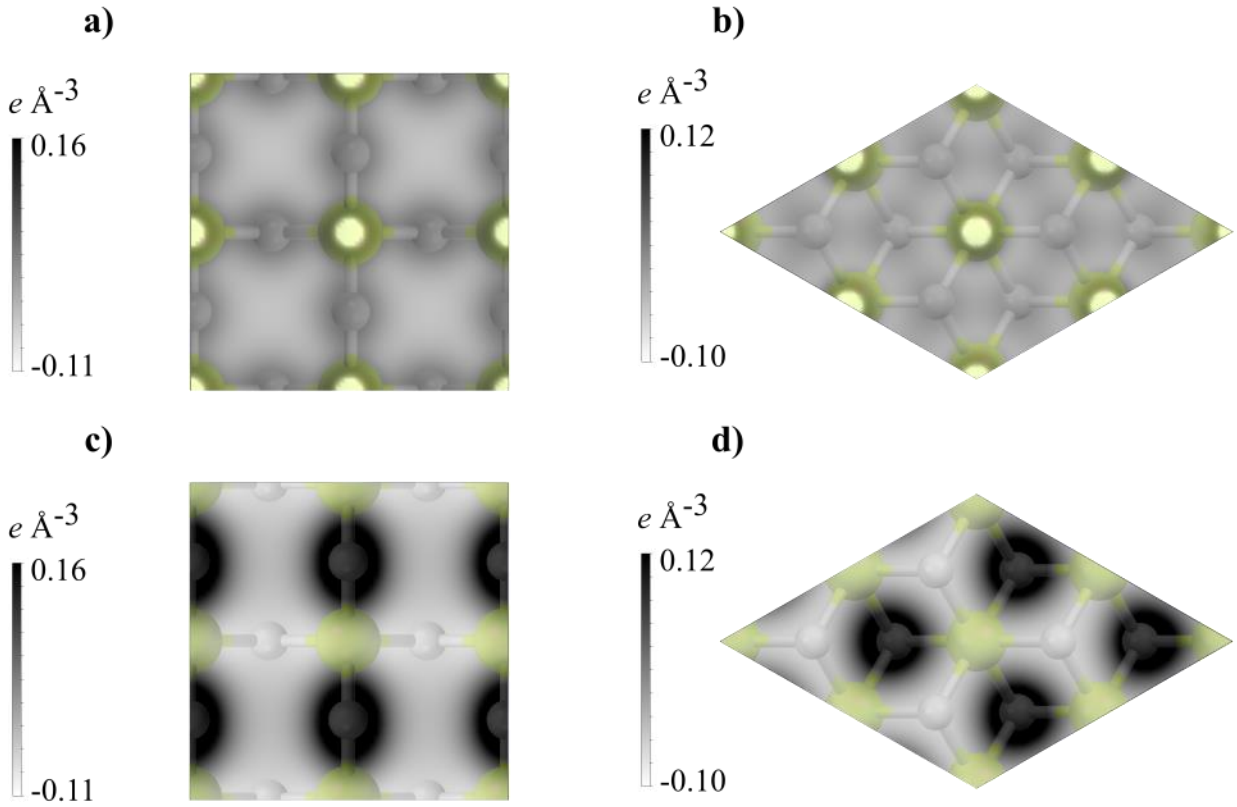

Figure 3.5. Charge density difference in the (100) plane at Δz=0 Å for a) α-BeH_2, and b) β-BeH_2 ; and at Δz=0.84 Å for c) α-BeH_2, and Δz=0.87 Å for d) β-BeH_2. The areas in lighter shade mark the zones depleted of charge, while the darker zones reflect the parts where the charge is most concentrated.

3.5. Linear-elasticity

After validation of the individual stability of the BeH_2 monolayers, their response at small strains is revised. The stiffness tensor is estimated by deforming the lattice at small steps of ε=0.002, within a linear-elastic limit of $\varepsilon_{ij} \leq \pm 0.02$. The number of elastic constants is defined

by the symmetry of the 2D lattice, for that matter, there are three independent elastic constants for α-BeH_2 and two for β-BeH_2. In Fig. 3.4, the small strain curves for the applied deformations in both monolayers are plotted.

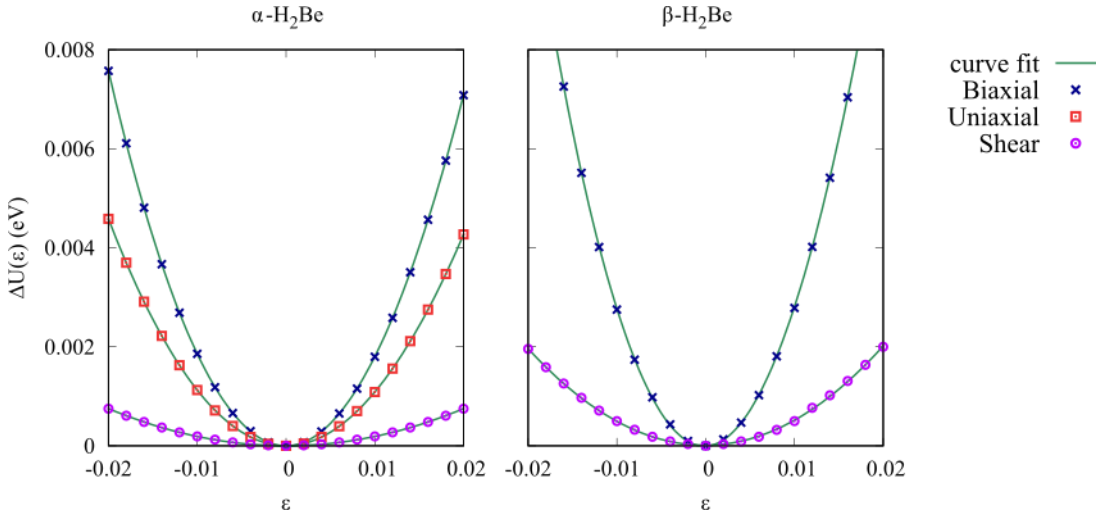

Figure 3.6. Small strain curves for a) α-BeH_2 and b) β-BeH_2 with a least-squares polynomial fit to obtain the strain energy density difference functions.

Least-squares polynomial fitting is performed to draw a curve that will become the strain energy density difference function, ΔU(ε). The stiffness matrix of α-BeH_2 and β-BeH_2 can now be generated as seen in Section 2.6. The values of the calculated SOECs together with the isotropic elastic modulus and Poisson's ratios can be found in Table 3.3, where these are compared to previous reports.

Table 3.3. Elastic properties of the BeH_2 monolayers. The SOEC and elastic moduli together with the values in the literature.

System Name		c_{11} (Nm^{-1})	c_{12} (Nm^{-1})	c_{66} (Nm^{-1})	E (Nm^{-1})	υ
α-BeH_2	Ref. 30	62.24	-11.84	8.21	59.98	-0.19
	This work	61.06	-10.29	10.45	59.33	-0.17
β-BeH_2	Ref. 30	84.97	13.98	35.50	82.67	0.16
	This work	81.38	15.19	33.09	78.54	0.19

The elastic stability criteria from Section 2.6 have been met,

α-BeH_2, $$61.06^2 + (-10.29)^2 > 0, \quad 8.21 > 0, \tag{3.7}$$

β-BeH_2, $$81.38^2 + 15.19^2 > 0, \quad 33.09 > 0. \tag{3.8}$$

In this work, a limit of 2% was set as the defining linear-elastic limit; however, the infinitesimal-strains regime was computed up to 5% deformation, since the reported elastic constants in the literature,[30] have no mention of the percentage to which these were estimated. Second- to fifth-order polynomial fitting was addressed, assessing the error margin between each term of the fitted curve, cautious to avoid overfitting. The literature, also, mentions the use of dispersion correction methods in their computations, reducing the lattice parameter and increasing cohesiveness, as seen in Section 3.2.

The careful computations for the values of the elastic constants in this work were done until convergence with the values of cutoff energy and k-points grid was definite. The adaptation of semi-core pseudopotentials which involve the 1*s* electron shell of Be was also considered, no change in the total energies with respect to the pseudopotential with a frozen core was seen, in turn, the calculated values of the elastic constants show no variation. The adoption of dispersion forces was also addressed, nevertheless, while most elastic constants did match to a low percent of error, *ca.* ~1%, the error margin for c_{66} in α-BeH_2, compared to the literature, was always overestimated by at least ~10%.

The values of the elastic modulus for both BeH_2 single layers fall short compared to better known 2D crystals like graphene (340 Nm^{-1}), h-BN (278 Nm^{-1}) or MoS_2 (120 Nm^{-1}), but can be more relatable to more compliant materials like phosphorene[20] (89 Nm^{-1} zigzag, 25 Nm^{-1} armchair). A negative value for c_{12} in α-BeH_2 yields a negative in-plane Poisson's ratio in isotropic conditions, it is not yet known if the auxetic behavior is valid at every direction. Therefore, to have a clearer grasp on the conditions that will allow α-BeH_2 to exhibit auxeticity, its anisotropic response must be evaluated.

The resulting direction-dependent properties are projected in polar plot form (Fig. 3.6), and the calculated values are resumed in Table 3.4. β-BeH_2, in its hexagonal lattice, confirms its status as an isotropic material, its mechanical properties are invariant to the direction they are measured. On the other hand, the square lattice of α-BeH_2 reveals an interesting anisotropy.

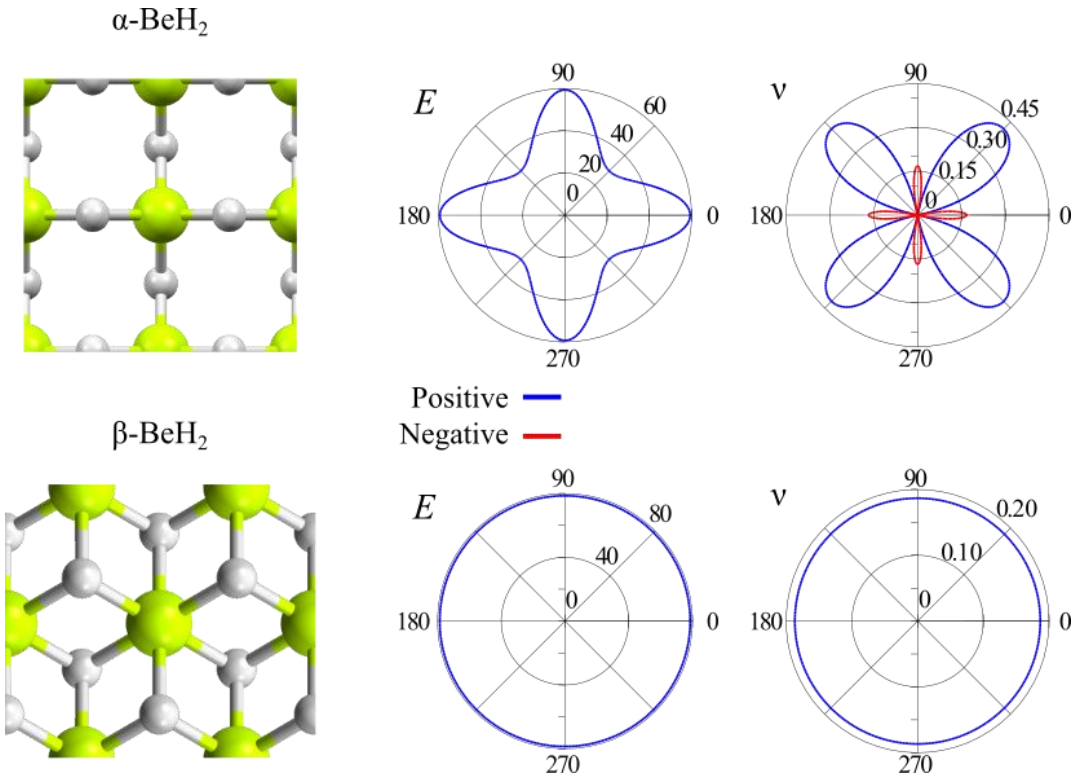

Figure 3.7. Be-centered monolayer perspectives and polar plots of the direction-dependent mechanical properties for α-BeH_2 and β-BeH_2. The NPR in α-BeH_2 is expressed only in the directions parallel to the Be-H bonds. The Be-H bonds of β-BeH_2 are invariant to the direction which they are infinitesimally stretched.

Table 3.4. Direction-dependent mechanical properties of α-BeH_2 and β-BeH_2.

System Name		E (Nm^{-1})	υ
α-BeH_2	at 0° (45°)	59.33 (29.62)	-0.17 (0.42)
β-BeH_2		78.54	0.19

Due to the 4-fold symmetry of α-BeH_2, the pattern will repeat at every quadrant of the plot. The Poisson's ratio is a very specific property, as it will be negative only in narrow

strips parallel to the directions of the Be-H bonds. For all other regions, the Poisson's ratio is a large positive value, with a maximum at the diagonal of the lattice (45°). In all, the Poisson's ratios of α-BeH_2 arrive at a wonderful petal flower figure.

Likewise, the elastic modulus is also affected by direction. A minimum *E* is predicted in the diagonals, this is important due to the elevated contraction rate and low resistance of the monolayer in these directions. Since *E* has a maximum value in the directions parallel to where ν is negative, a stiffer response of the crystal is expected. These remarks are in line with the theory on auxetic solids that emphasize enhancement of stiffness in the directions where negative Poisson's ratios are found.[10-11] Other 2D materials that have also expressed in-plane auxeticity and documented this behavior are δ-phosphorene,[75] B-graphane,[80] B_4N,[82] and Be_5C_2.[141]

4. 2D BeH_2 under Large Deformations

4.1. Introduction

No current precedent is known of studies that consider the BeH_2 monolayers under large deformations. In this Chapter, the structural behavior, and the mechanical response of 2D BeH_2 under tensile strains are reported for the first time. Therefore, the finite-strains regime is explored by inducing biaxial and uniaxial tensile strains. Having in α-BeH_2, as seen in its polar plots, two main uniaxial paths of interest, along the axis and the 45° diagonal directions. Whereas the chiral directions of β-BeH_2, zigzag and armchair, are also evaluated.

By performing small progressive strains to the unit cells, it is possible to compute the ideal tensile strengths. However, before rushing into conclusions, one must also make certain that mechanical instabilities are also considered, as the lattice may very well fall into a plastic deformation that will cause a phase transition or failure of the structure before the critical strain is reached. Since unit cells are constrained to a reduced space, few degrees of freedom are allowed for their components to relax properly at extreme conditions. For that, the straining process is repeated, but this time involving a larger structure with more components in the lattice, a 2x2 supercell is adopted.

The stress-strain curves have calculated the mechanical response of the BeH_2 monolayers under large deformation, they have predicted them as soft 2D crystals, with the α-BeH_2 phase as a material of superior elasticity, for every loading condition evaluated; while β-BeH_2 has revealed to fail at short strains. α-BeH_2 is also interesting due to its negative Poisson's ratio, a more in-depth analysis to the structural changes that occur with deformation of the structure have given light into describing the behavior that produces this phenomenon. In all, the BeH_2 polymorphs are exciting materials for their use in mechanical applications.

4.2. Structural Analysis

The bond lengths (r_{Be-H}) and bond angles (θ_{H-Be-H}) of α-BeH_2 and β-BeH_2 at the ground-state do not change with respect to the direction they are measured. Nonetheless, when straining the lattice at specific directions, the parameters will behave accordingly to the conditions of the load exerted on them. Here, two bond lengths, r_1 and r_2, are contemplated for α-BeH_2 (Fig. 4.1a) and for β-BeH_2 (Fig. 4.1b).

In α-BeH_2, the r_1 bonds are parallel to the x_1 axis, and the r_2 bonds are found parallel to the x_2 axis. There are four bond angles considered in α-BeH_2, the θ_1 and θ_2 bond angles are each colinear to the r_1 and r_2 bonds, generating hinges parallel to the x_1 and x_2 axes, respectively. The θ_3 and θ_4 bond angles sit at the meeting points of r_1 and r_2 bonds, completing the coordination tetrahedra of α-BeH_2.

In β-BeH_2, the r_2 bonds will be taken as parallel to the x_2 axis (the armchair direction), while r_1 bonds are found along the zigzag directions of the lattice. Three bond angles were considered in β-BeH_2, the θ_1 bond angle binds together two r_1 bonds running through the zigzag direction. The θ_2 and θ_3 angles are found at the sitting points of r_1 and r_2 bonds, with θ_2 merging an r_2 bond and a first-neighbor r_1 bond, while θ_3 groups together an r_2 bond with a second-neighbor r_1 bond.

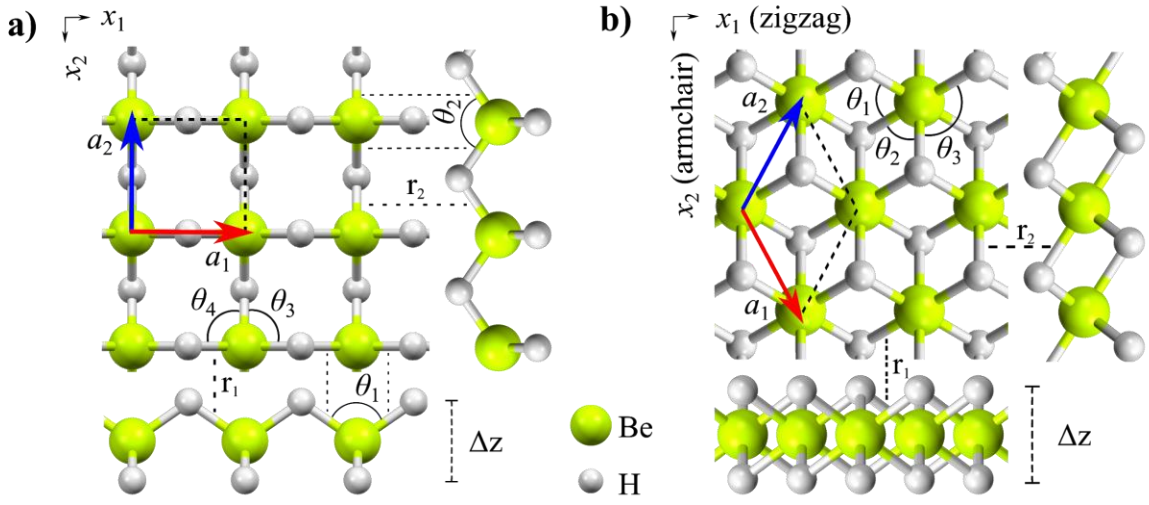

Figure 4.1 The ground-state structures of a) α-BeH_2 and b) β-BeH_2. The bond lengths (r) and bond angles (θ) are shown.

4.3. BeH_2 Under Biaxial Tensile Strain

The biaxial tensile strain, as mentioned in Chapter 2, is an isotropic in-plane deformation of the lattice. From loading a crystal in this condition, it is possible to gain insight into the mechanical properties that the solid will reveal, while keeping a number of variables controlled (like perpendicular strain).

Under large deformations, Eq. 2.48 determines the deformed lattice vectors to evaluate this loading condition. In Fig. 4.2, the changes in structural parameters like the out-of-plane resultant strain, bond lengths and the bond angles of the in-plane biaxially strained BeH_2 monolayers are addressed. These values measure until a state of mechanical instability in the lattice is reached.

The out-of-plane resultant strain measures the changes produced in the thickness of the lattice. Of note, the scale at which these deformations occur, in α-BeH_2 the resultant strain is about eight times that of β-BeH_2, this drastic reduction in the thickness of α-BeH_2 can be regarded as a flattening of the layer (Figs. 4.2a and 4.2b). The biaxial strain affects both bond lengths at the same rate, since the load is applied at all directions of the plane, thus obtaining the overlapped curves of Figs. 4.2c and 4.2d; all four curves of bond lengths reach a value close to 1.68 Å. The bond angles of interest for α-BeH_2 (Fig. 4.2e) and β-BeH_2 (Fig. 4.2f) are also shown. In α-BeH_2, the angles θ_1 and θ_2 are indistinguishable from each other, as also happens with θ_3 and θ_4. In β-BeH_2, this also happens for θ_1 and θ_2. Thus, for both monolayers, only θ_1 and θ_3 are needed.

The applied tension on α-BeH_2 creates a stretch of the bonds, r_1 and r_2, opening the bond angles parallel to the deformation, θ_1, and θ_2. In consequence, the bond angles found perpendicular to the strain, θ_3 and θ_4, are reduced. The overall effect is a flattening of the layer, as seen in the resultant strain Figures 4.2a and 4.2b. Biaxial tension in β-BeH_2 delivers a similar picture, a stretch of the bond lengths r_1 and r_2 opens the θ_3 bond angle; the effect of said opening will force the angles θ_1 and θ_2 to become narrower.

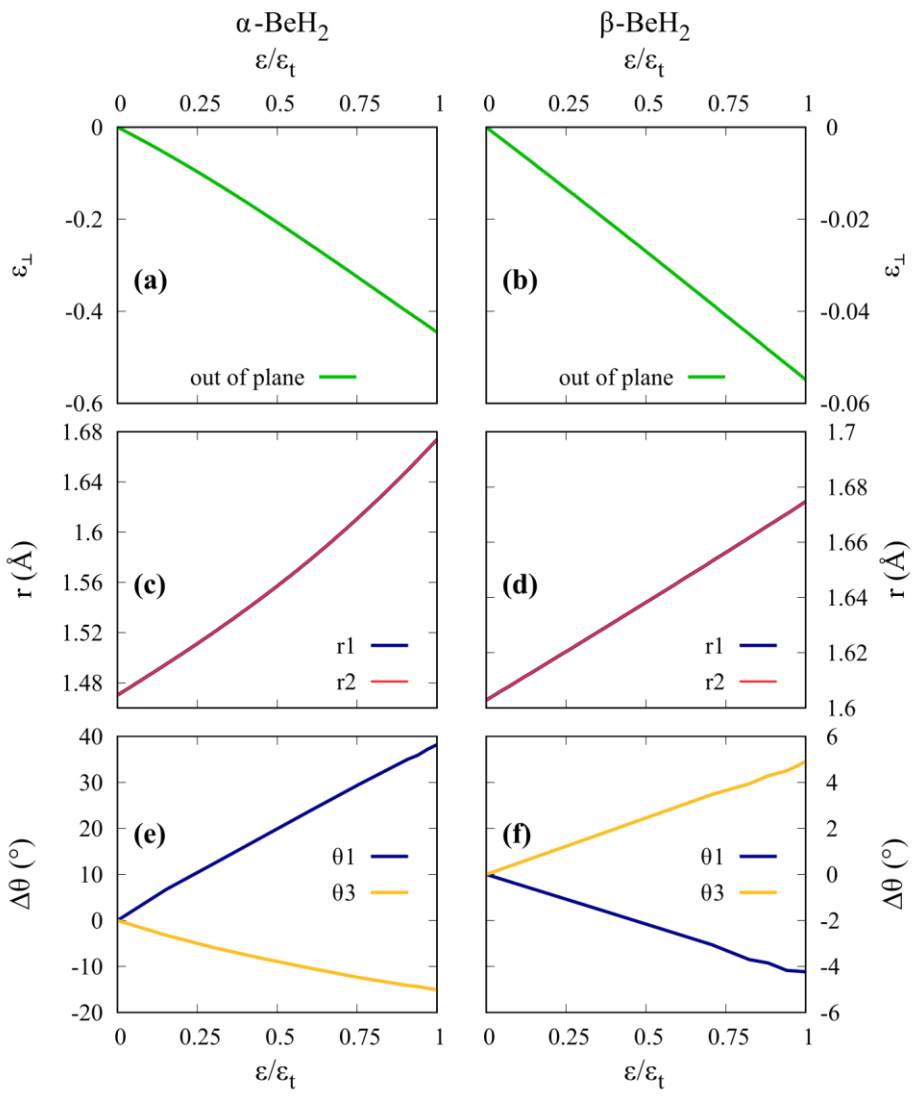

Figure 4.2. Structural deformations (out-of-plane resultant strain, $\varepsilon_{\perp}$; bond length, r; change in bond angles, $\Delta\theta$) of α-BeH_2 and β-BeH_2 under biaxial tensile strain until phase transition (ε_t).

The resistance against biaxial strains for α-BeH_2 and β-BeH_2 was computed, and their respective stress-strain curves have been calculated into Fig. 4.3, and Fig. 4.4, respectively. The elastic modulus of α-BeH_2 is E= 46.70 Nm^{-1}, the stiffness in this direction is slightly lower than the value predicted for the infinitesimally strained lattice. The computed ideal strength under biaxial strain is of 6.30 Nm^{-1}, at a critical strain of 0.47. To validate the values for the primitive cell, supercells were adopted. A phase transition is predicted to occur at a

maximum strain of 0.33, with a strength of 5.99 Nm^{-1}. The values of strain that this phase can bear suggest mechanical flexibility superior to most 2D materials.

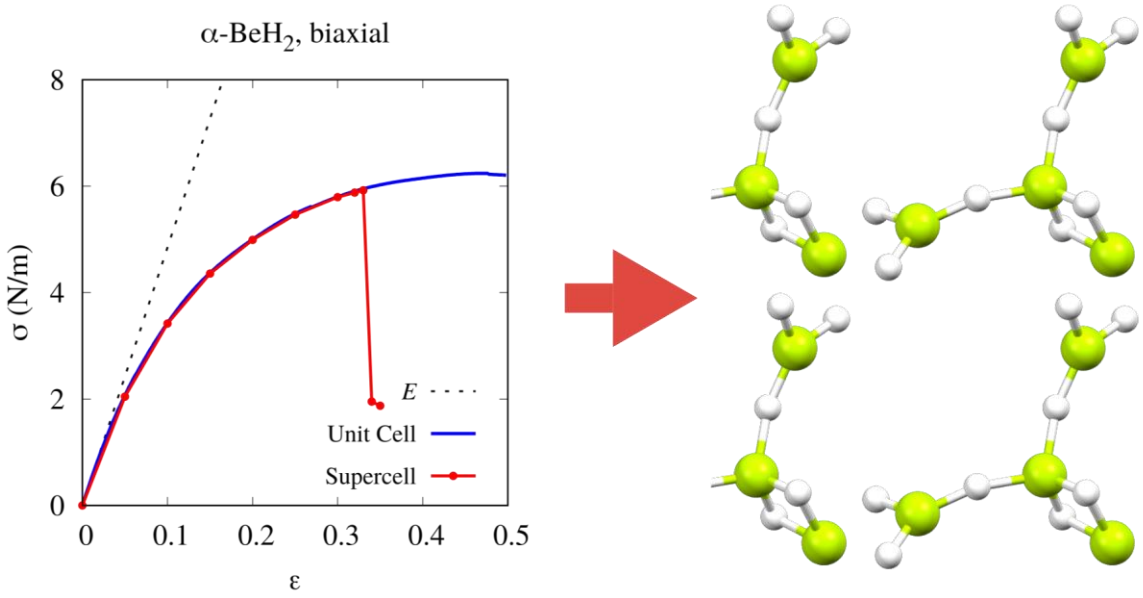

Figure 4.3. Stress-strain curves for α-BeH_2 under biaxial tensile strain and plastically deformed structure. *E* is the infinitesimal elastic modulus, the blue curve is the calculated curve with a primitive cell, and in red, the calculated curve of a supercell.

The elastic modulus of biaxially strained β-BeH_2 is 88.47 Nm^{-1}, a stiffer response than when infinitesimally strained. The computed ideal strength is of 10.57 Nm^{-1}, at a critical strain of 0.35, revealing greater resistance to load than the ideal strength of biaxially strained α-BeH_2. However, phase transitions were predicted to occur at strains of 0.08 and strengths of 5.71 Nm^{-1}. These results show a drastic deviation from the computed values for critical strains, limiting the potential flexibility of the structure. The calculated values from the stress-strain curves of α-BeH_2 and β-BeH_2, together with the out-of-plane distortion and bond lengths before undergoing phase transitions, can be found in Table 4.1.

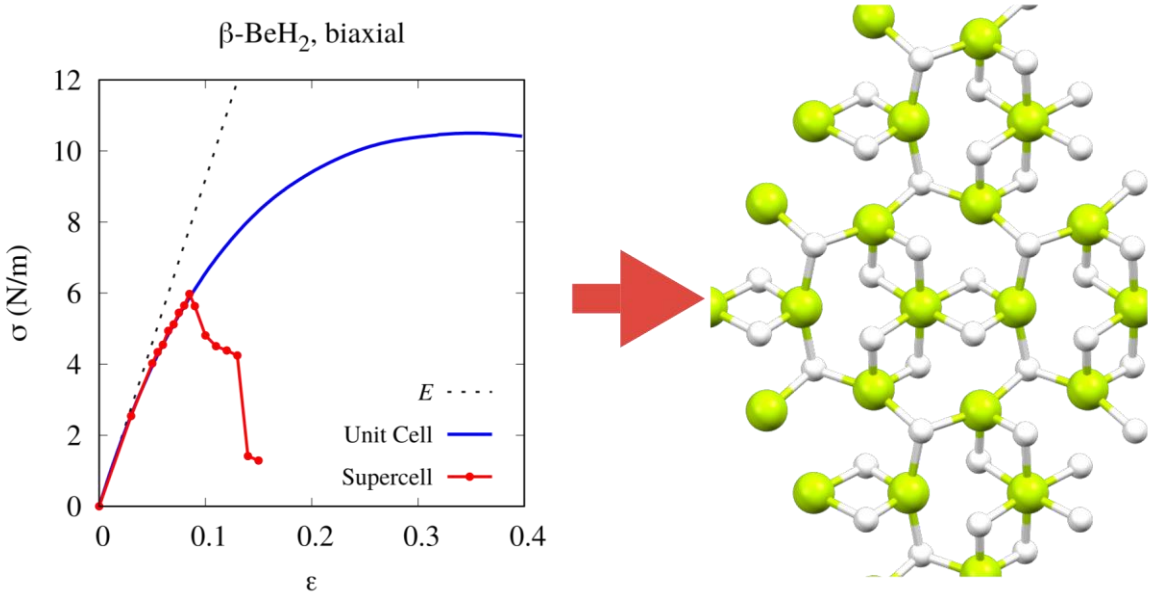

Figure 4.4. Stress-strain curves for β-BeH_2 under biaxial tensile strain and plastically deformed structure. *E* is the infinitesimal elastic modulus, the blue curve is the calculated curve with a primitive cell, and in red, the calculated curve of a supercell.

Table 4.1. α-BeH_2 and β-BeH_2 under biaxial strain. The elastic modulus (*E*), the critical strains (ε_c) and the ideal strength (σ_c); together with the maximum strains (ε_t) and strengths (σ_t), out-of-plane distortions (Δz), and bond length (r) before phase transitions

System name	*E* (N/m)	ε_c	σ_c (N/m)	σ_t (N/m)	ε_t	Δz (Å)	r(Å)
α-BeH_2	46.70	0.47	6.30	5.99	0.33	0.93	1.68
β-BeH_2	88.47	0.35	10.57	5.71	0.08	1.68	1.68

4.4. 2D BeH_2 Under Uniaxial Tensile Strain

The anisotropy of α-BeH_2, as seen by the polar plots of Section 3.5, highlights two paths of interest for uniaxial tension to be applied. Here, tension parallel to the x_1 axis will be labeled as axial, while at an angle of 45°, it will be named as the diagonal direction. The lattice vectors to apply a uniaxial tensile strain (Eq. 2.49) in diagonal α-BeH_2 are given by,

$$\vec{a}_1 = \frac{\sqrt{2}}{2} a_0 \hat{x}_1 + \frac{\sqrt{2}}{2} a_0 \hat{x}_2, \qquad \vec{a}_2 = -\frac{\sqrt{2}}{2} a_0 \hat{x}_1 + \frac{\sqrt{2}}{2} a_0 \hat{x}_2. \tag{4.1}$$

Similarly, the chirality of β-BeH_2 distinguishes two principal orientations, the zigzag and armchair directions, both taken into consideration.

The deformation in the lattice parameters with respect to the applied uniaxial strain of α-BeH_2 and β-BeH_2 is shown in Fig. 4.5. The expected behavior is for these to decrease virtually monotonically as strain progresses, as a sign of traverse contraction; as happens with the rate of change for the uniaxial distortions of β-BeH_2 (Figs. 4.5b and 4.5c). However, axial α-BeH_2 does not follow this logic (Fig. 4.5a), an increment of the in-plane transverse direction is registered, an indicator of auxeticity. In this direction, a maximum expansion of 4% is predicted, preserving its auxetic behavior until the point of instability. Strained diagonal α-BeH_2, (Fig. 4.5c), denotes a reversal of behavior in the thickness of the monolayer mid-strain, transitioning into out-of-plane auxeticity and recovering most of the original buckling before failure. Diagonal α-BeH_2 also undergoes an in-plane traverse compression of 13%, indicating a substantial contraction in the direction perpendicular to the applied strain, in line to its calculated infinitesimal in-plane Poisson's ratio.

From the traverse strains for the uniaxially loaded BeH_2 monolayers, the Poisson's ratios are calculated from Eq. 2.50 and shown in Fig. 4.6. The Poisson's ratios as functions of the applied strain for the in-plane axial and out-of-plane diagonal directions of α-BeH_2 are shown in Fig. 4.6a. In diagonal α-BeH_2, the calculated Poisson's ratios range from $0.32 < \upsilon < -0.27$, at an almost constant decrement. The transition into auxeticity is computed close to 0.75 of the normalized strain, and the Poisson's ratio continues to drop until reaching failure. Strain in the axial α-BeH_2 does reveal auxeticity, the slope of the curve progressively decreases until stagnation in the rate of change is computed halfway into the applied strain.

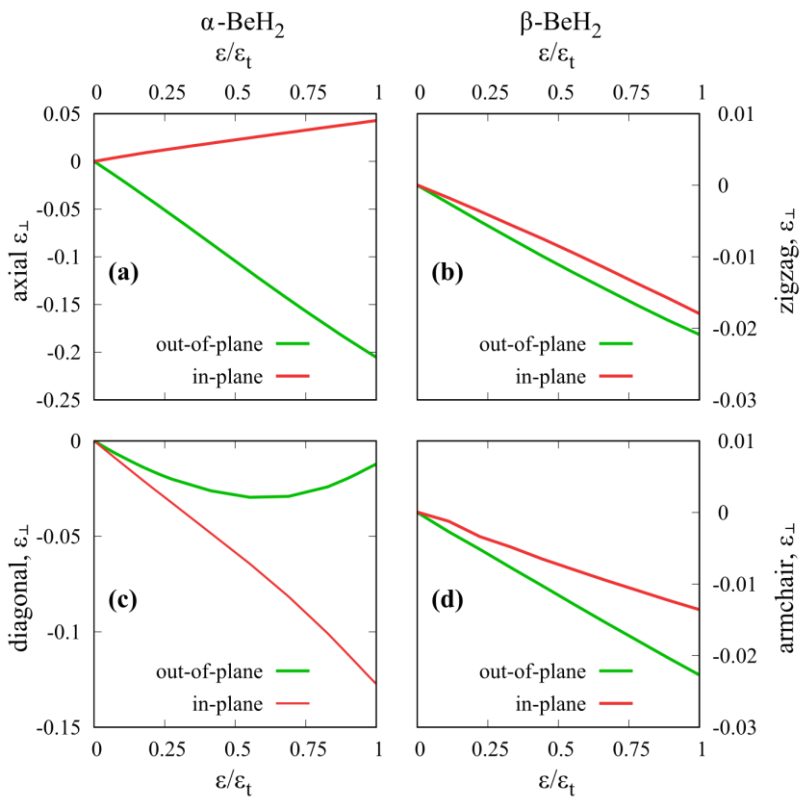

Figure 4.5. Resultant strains until phase transition (ε_t) for the uniaxial distortions of α-BeH_2 in the a) axial and c) diagonal directions, and for β-BeH_2 in the b) zigzag and d) armchair directions.

Figure 4.6b depicts the in-plane Poisson's ratios for the zigzag and armchair directions of uniaxially strained β-BeH_2. The calculated traverse deformations reveal a marked difference in the response of the directions in the solid when strained; hence, when measured individually, the anisotropy ensues. Straining in the armchair direction exhibits a greater opposition to deformation than in strain in the zigzag direction. This markedly different response gradually heightens as loading progresses. The Poisson's ratio in the zigzag direction increases with applied strain, so does the armchair direction for a short period of strain. After a sharp increase in its Poisson's ratio, the following steps reveal a steady decline in the rate of traverse contraction. The anisotropy of β-BeH_2 exhibits a compliant direction (zigzag) and a stiffer one (armchair). Albeit these conditions might be too specific, they are helpful in understanding the overall mechanical behavior displayed by this polymorph.

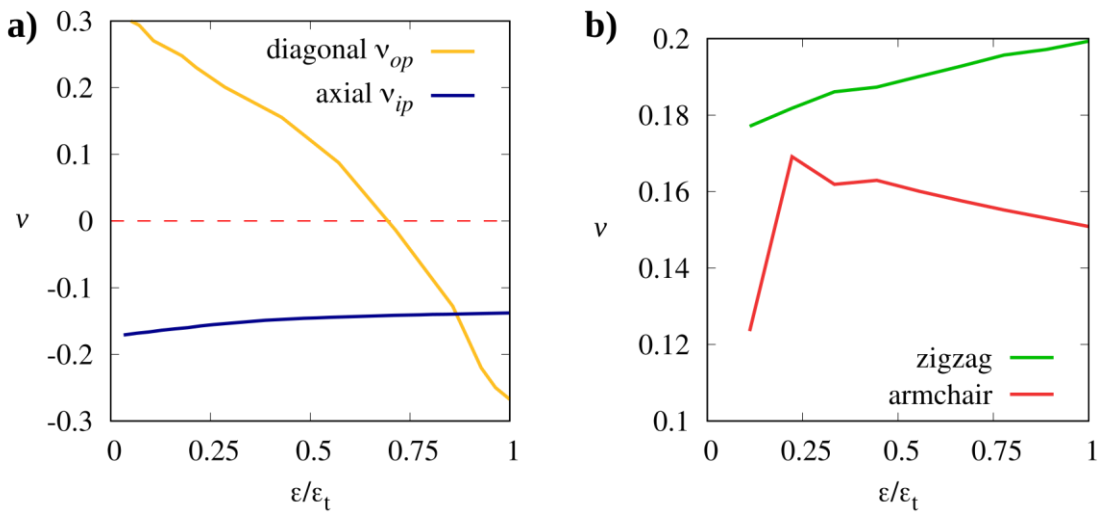

Figure 4.6. Poisson's ratios until phase transition (ε_t) for a) α-BeH_2 in the out-of-plane diagonal (yellow) and in-plane axial (blue) directions, and of b) β-BeH_2 in the in-plane zigzag (green) and in-plane armchair (red) directions.

A change in the magnitude of the cell inevitably alters its internal structure. The elastic bond lengths (Fig. 4.7), reveal that the equivalence of r_1 and r_2 does not hold for applied tension in a single axis, save for the diagonal α-BeH_2 direction of (Fig. 4.7c). For loads at 45° in α-BeH_2, the applied strain is equivalent in the two in-plane axes, therefore, r_1 and r_2 are distorted at equal rates. Figs. 4.7a, 4.7b and 4.7d display an increase in the bond length parallel to the direction of the applied strain, and while the perpendicular component is minimized in zigzag BeH_2 (Fig. 4.7b), Figures 4.7a and 4.7d show no significant change in their magnitudes throughout deformation.

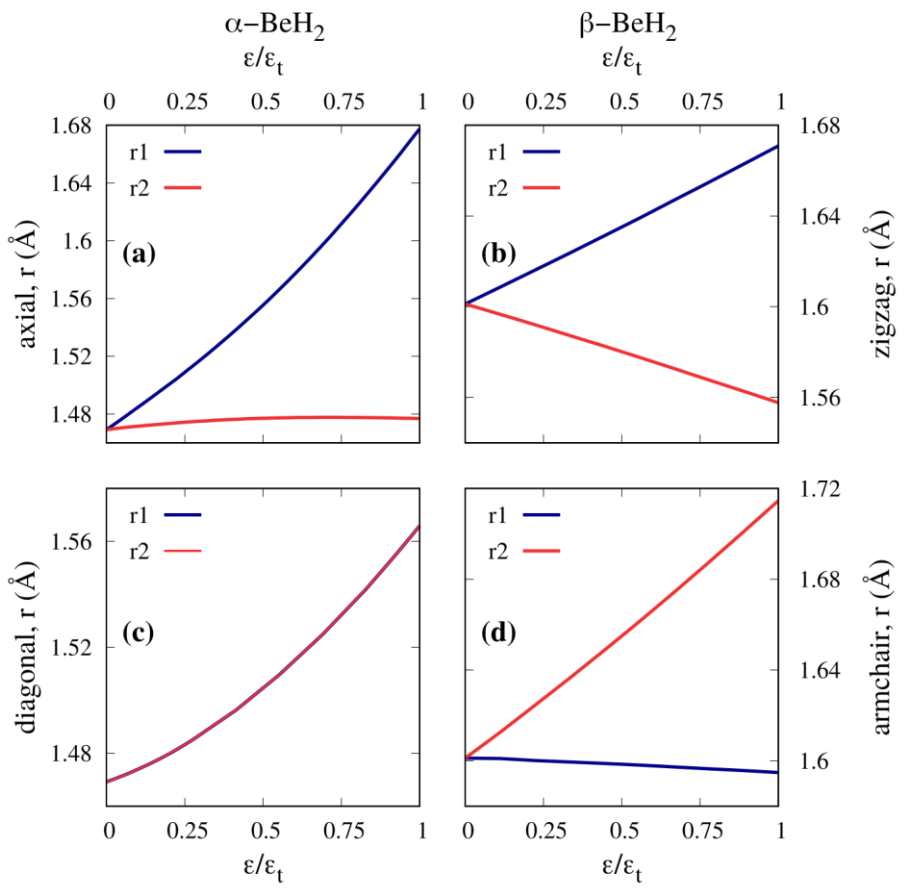

Figure 4.7. Bond lengths until phase transitions for the uniaxial distortions of α-BeH_2 in the a) axial and c) diagonal directions, and for β-BeH_2 in the b) zigzag and d) armchair directions.

Previously, in Section 4.2, a maximum bond length was estimated for both biaxially strained α-BeH_2 and β-BeH_2 before reaching phase transitions, at r=1.68 Å. The predicted bond lengths at the mechanical instabilities for most of the computed uniaxial deformations approach the same value of r_{pt} ≈1.68Å. Arguably, it can be inferred that this is a critical value for bond lengths before the material undergoes an instability. The newly defined value of r_{pt} is closer to the values of r for β-BeH_2 than it is for the bond length of α-BeH_2. Therefore, the initial difference in bond lengths in both unstrained α-BeH_2 and β-BeH_2 can be linked directly to the magnitude of strain that these crystals can ultimately withstand.

There is another unclear issue, and that is to find the reason for the unchanged bond lengths in r_2 in both strained axial α-BeH_2 and armchair β-BeH_2. The answer might be hidden within another parameter of the crystals, Fig. 4.8 shows the change in the bond angles with

respect to uniaxial tensile strain. In axial α-BeH_2, three bond angles are independent, these being the angles collinear with the axes, θ_1 and θ_2, and a third more in θ_3 (equal to θ_4). For diagonal α-BeH_2, three angles are also independent, but these are θ_3, θ_4 and θ_1 (equal to θ_2). In β-BeH_2, all three considered angles are independent of each other.

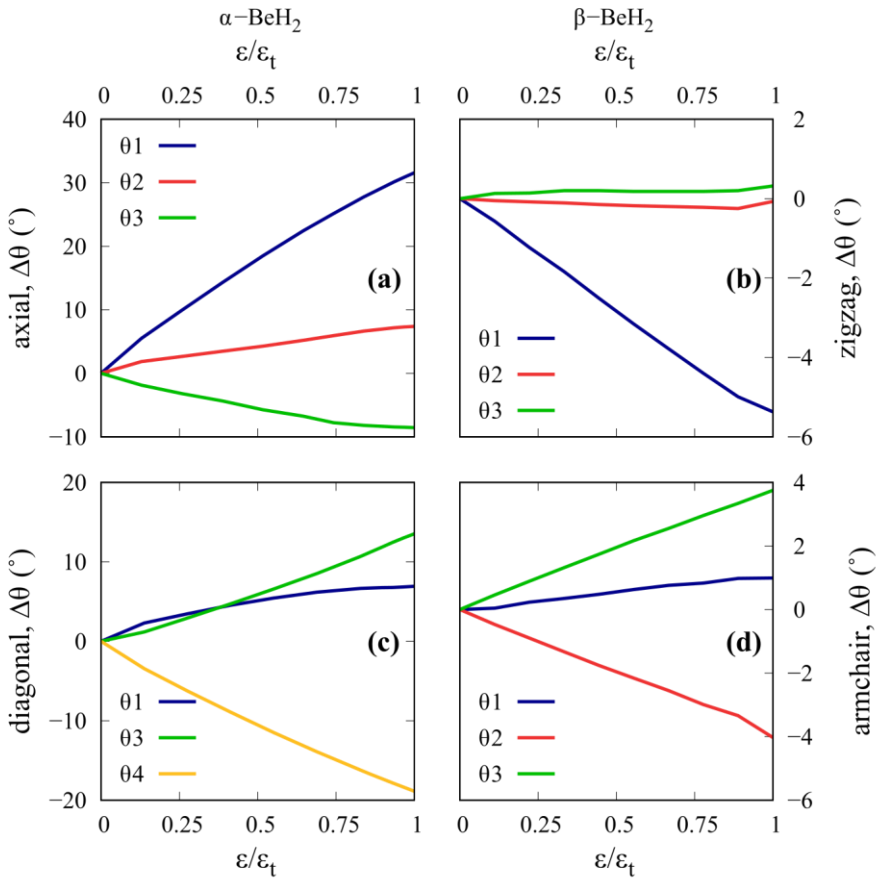

Figure 4.8. Bond angle changes until phase transition for the uniaxial distortions of α-BeH_2 in the a) axial and c) diagonal directions, and for β-BeH_2 in the b) zigzag and d) armchair directions.

Strain in zigzag β-BeH_2 is easy to understand, as r_1 is stretched, θ_1 is narrowed, the other bond angles are seemingly unaffected, as r_2 contracts it compensates for the change in r_1. In armchair β-BeH_2, however, tension stretches r_2, narrowing θ_2, but the effect is countered by widening of θ_3, leaving θ_1, and ultimately r_1, unaltered.

In diagonal α-BeH_2, the applied strain stretches r_1 and r_2 at an equal rate, hence, θ_1 and θ_2 also change in the same proportion (Fig. 4.8c); the increase of θ_1 is associated with

the flattening of the layer when strained. The angle θ_4 is found parallel to the direction of the strain, thus it will contract as the stretch increases, and θ_3 will expand as it is found at the opposing end.

Fig. 4.9 depicts three stages of strain for diagonal α-BeH_2, where strain is applied horizontally, parallel to the projected images of the BeH_2 systems. As the applied strain continues to distort the structure, bond lengths gradually increase, separating the atoms equidistantly, the initial stretch will produce a thinning of the buckling, slightly flattening the monolayer. At a stage where θ_3 starts to diverge from θ_1, the out-of-plane distortion stops reducing its thickness. θ_3 acts as the opening hinge mechanism, and as it widens and the bond lengths increase, the out-of-plane NPR phenomenon is produced. A known case of transition into auxeticity is graphene,[78-79] in which transition occurs at a $\varepsilon \approx 0.06$ for the armchair direction; in diagonal α-BeH_2, this transition has been calculated at $\varepsilon \approx 0.18$. The failure stage does not have a bond length similar to the estimated value of r_{pt}. Instead, its mechanical instability can be linked to the value of θ_4, as this angle decreases until measuring 90.6º, generating much stress in the stability of the tetrahedral unit.

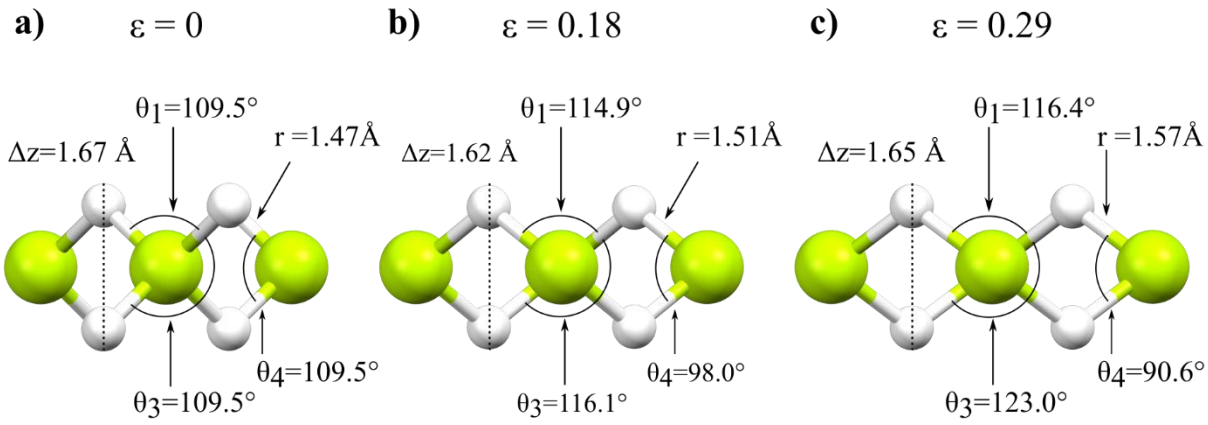

Figure 4.9. The out-of-plane NPR transition in diagonal α-BeH_2. a) At equilibrium; b) at the thinnest predicted out-of-plane distortion; c) at the maximum value of strain before phase transition occurs.

For axial α-BeH_2, the tension parallel to x_1 increases r_1, opening the θ_1 angle; the effect produced by stretch lowers the buckling height, seen by a negative out-of-plane deformation and narrowing of θ_3, effectively flattening the layer. However, the direction perpendicular to the strain expands while r_2 remains virtually unaffected through all the

deformation process; this is tempered by a widening of θ_2, arriving at the predicted NPR effect.

Fig. 4.10, depicts the evolution of auxeticity for axial α-BeH_2, the ground-state is presented in the Figures to the left and the state before mechanical instability is shown to the right. At the initial setup, the bond lengths (r_{ng}, n=1,2) and bond angles (θ_{ng}, n=1,2,3,4) are equivalent. As strain is applied in a direction parallel to the bonds, the bond lengths (r_{1t}) and the bond angles (θ_{1t}), will increase and expand the lattice. At conditions approaching failure, the traverse bond lengths (r_{2t}) are virtually unaffected, however, the bond angles perpendicular to the applied load (θ_{2t}) will increase, reducing the out-of-plane distortion (Δz_t), and effectively flattening the monolayer; expanding this side of the monolayer as well. The NPR phenomenon here reported is reminiscent of the observed cases for the re-entrant foam of Lakes[12] as well of phosphorene,[13-14] where orthogonal hinges will expand at applied tension. Very likely, the NPR is intrinsic to this type of symmetry, which may soon enrich the number of viable auxetic materials.

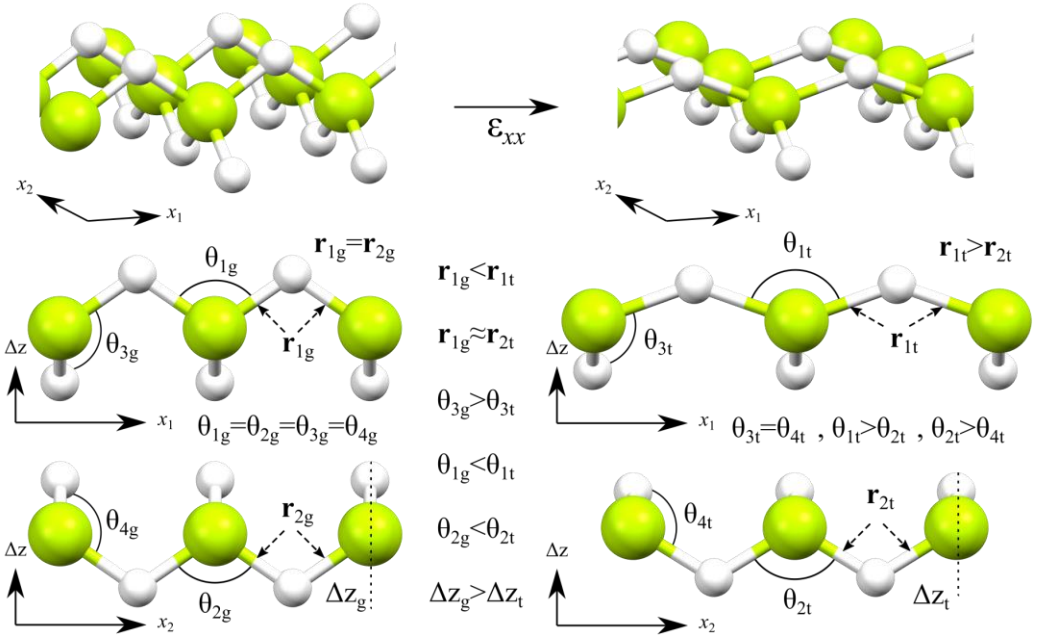

Figure 4.10. α-BeH_2 at (left) the ground-state, and (right) before inducing the phase transition in the *axial* direction. The bond angles traverse to the applied strain (θ_{2t}) will expand, opening the orthogonal hinges and flattening the monolayer, triggering the auxetic response.

The computed elastic modulus and in-plane Poisson's ratios for axial α-BeH_2 are 55.58 Nm^{-1} and -0.17, while for diagonal α-BeH_2 these are 30.12 Nm^{-1} and 0.42, in line with the calculated values of Chapter 3. The stress-strain curves of axial α-BeH_2 are presented in Fig. 4.11, the predicted ideal tensile strength in this direction is of 9.94 Nm^{-1} at a critical strain of 0.57. Phase transitions are expected to occur at strains of 0.31 and strengths of 8.60 Nm^{-1}, undermining the critical strain almost by half.

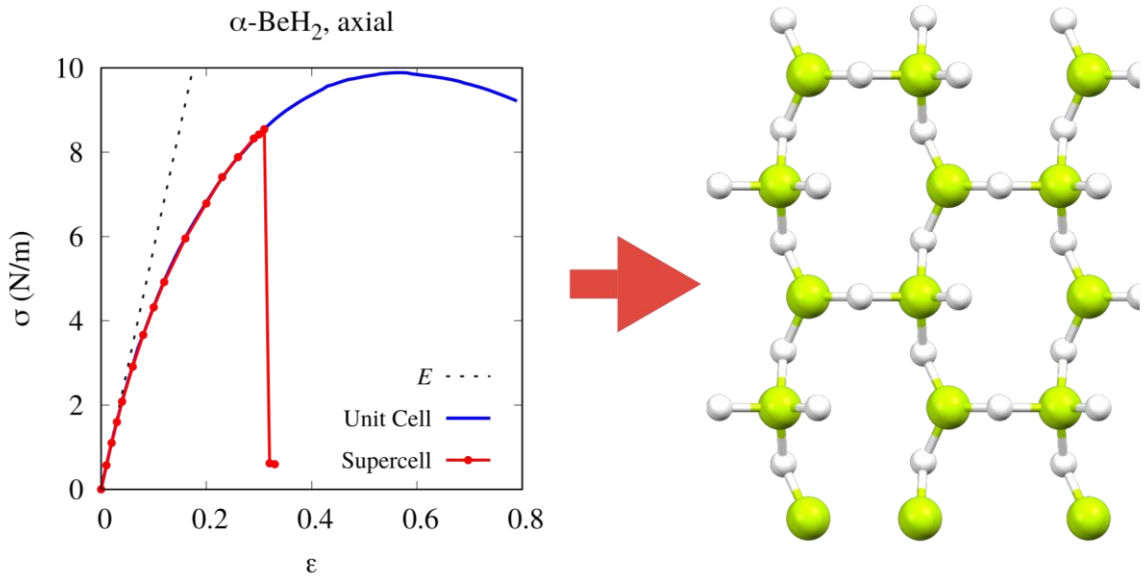

Figure 4.11. Stress-strain curves for α-BeH_2 under tensile strain in the axial direction and plastically deformed structure. *E* is the infinitesimal elastic modulus, the blue curve is the calculated curve with a primitive cell, and in red, the calculated curve of a supercell.

The stress-strain curve for the diagonal direction of α-BeH_2 is shown in Fig. 4.12, the ideal strength is of 15.83 Nm^{-1} and the critical strain, 0.52. However, the mechanical instabilities are expected to occur at values of 0.29 and 10.14 Nm^{-1}, for the strain and stress, respectively. The more compliant direction also resulted as the more resistant to stresses, perhaps this can be attributable to the out-of-plane NPR transition at ε≈0.18, which sees the Poisson's ratio decrease until a mechanical instability is reached.

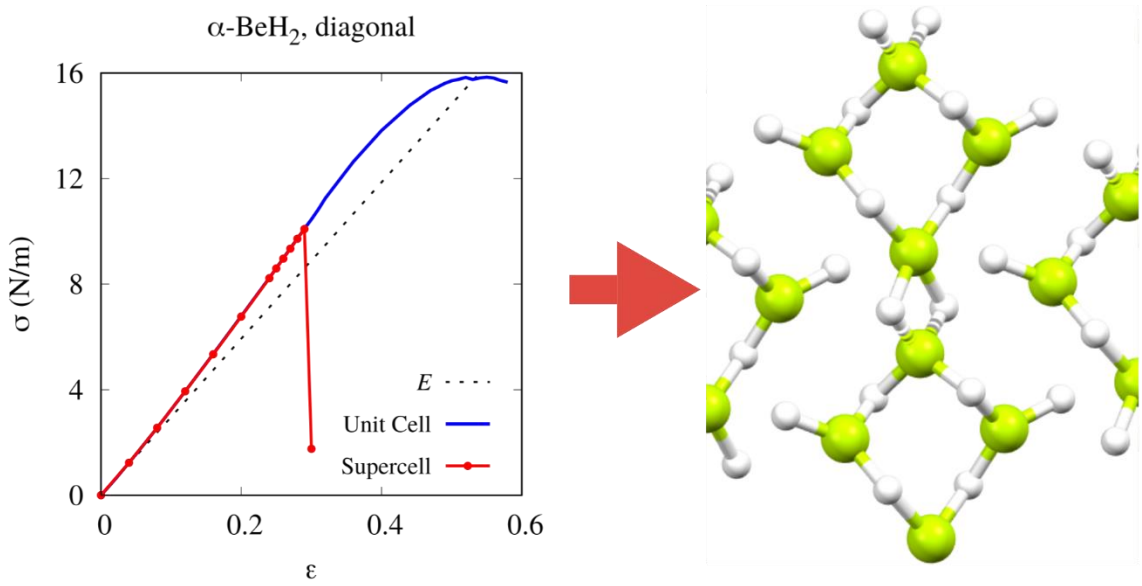

Figure 4.12. Stress-strain curves for α-BeH_2 under tensile strain in the diagonal direction. *E* is the infinitesimal elastic modulus, the blue curve is the calculated curve with a primitive cell, and in red, the calculated curve of a supercell.

Table 4.2 puts together these computed properties, together with the traverse strains, the out-of-plane distortions and bond lengths at the mechanical instabilities. The structure remains stable until deformations close to 30%, these calculated values of deformation are slightly higher than the critical strains of graphene[6] in the *armchair* (27%) and MoS_2[93] *zigzag* (23%) directions. Overall, this is a very interesting crystal, as its flexibility is superior to most known 2D materials,[44] together with its bidirectional auxeticity make it a desirable candidate for strain involving applications.

Table 4.2. α-BeH_2 under strain in the axial and diagonal directions. The elastic modulus (*E*), critical strains (ε_c) and ideal tensile strengths (σ_c); together with the maximum strains (ε_t) and strengths (σ_t), the in-plane traverse strains ($\varepsilon_{\perp\, ip}$), out-of-plane distortions (Δz), and bond lengths (r) before phase transitions.

α-BeH_2, direction	*E* (N/m)	ε_c	σ_c (N/m)	ε_t	σ_t (N/m)	$\varepsilon_{\perp ip}$	Δz (Å)	r (Å)
axial	55.58	0.57	9.94	0.31	8.60	0.04	1.33	1.67
diagonal	30.12	0.52	15.83	0.29	10.14	-0.13	1.65	1.57

In turn, the elastic modulus and Poisson's ratio for β-BeH_2 in the zigzag direction are of 72.41 Nm^{-1} and 0.18, while in the armchair direction, these are 73.68 Nm^{-1} and 0.12. Where the armchair direction is slightly stiffer than the zigzag direction, with a higher elastic modulus but a lower Poisson's ratio. The calculated stress-strain curve for zigzag β-BeH_2 is shown in Fig, 4.13, the ideal tensile strength is 7.12Nm^{-1}, at a critical strain of 0.24. But mechanical instabilities are expected to occur on exceeding strains of 0.09, and strengths of 4.97 Nm^{-1}. This trend repeats when straining in the armchair direction as well, the strain-stress curve of Fig. 4.14, reveals an ideal tensile strength of 7.43 Nm^{-1}, and a critical strain of 0.22. These would be undermined by phase transitions occurring at strains of 0.09, and strengths of 5.21 Nm^{-1}. The anisotropy in β-BeH_2 is not as heightened when the crystal reaches its mechanical instabilities. The failure strains of each chiral direction are found at 9%, in close proximity with the biaxial strain, and the failure strengths reveal the armchair direction to be the more resistant, only by a slight margin.

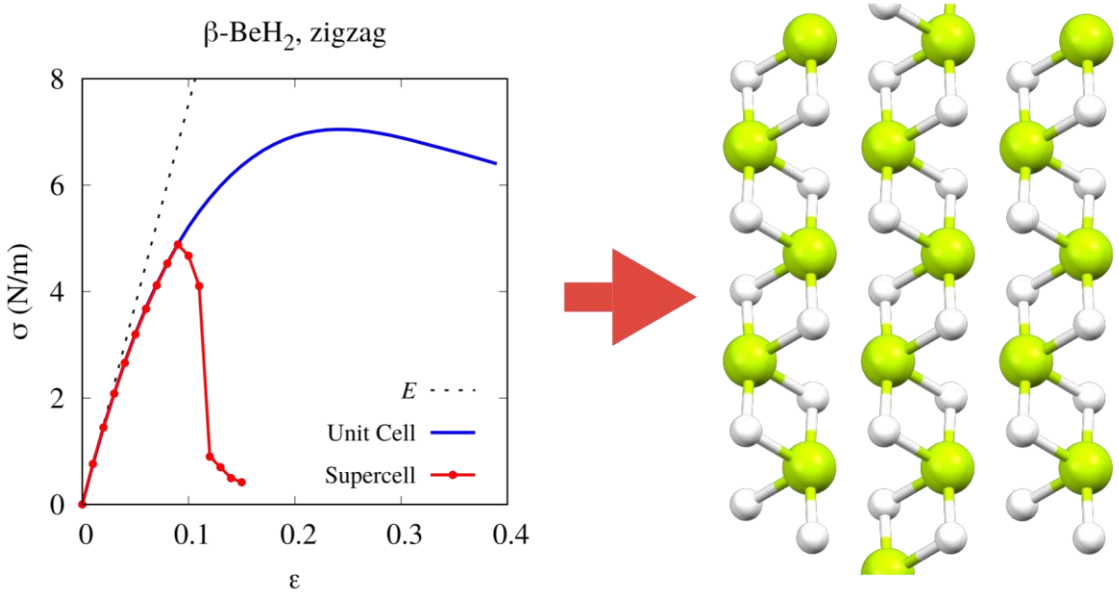

Figure 4.13. Stress-strain curves for β-BeH_2 under tensile strain in the zigzag direction and plastically deformed structure. *E* is the infinitesimal elastic modulus, the blue curve is the calculated curve with a primitive cell, and in red, the calculated curve of a supercell.

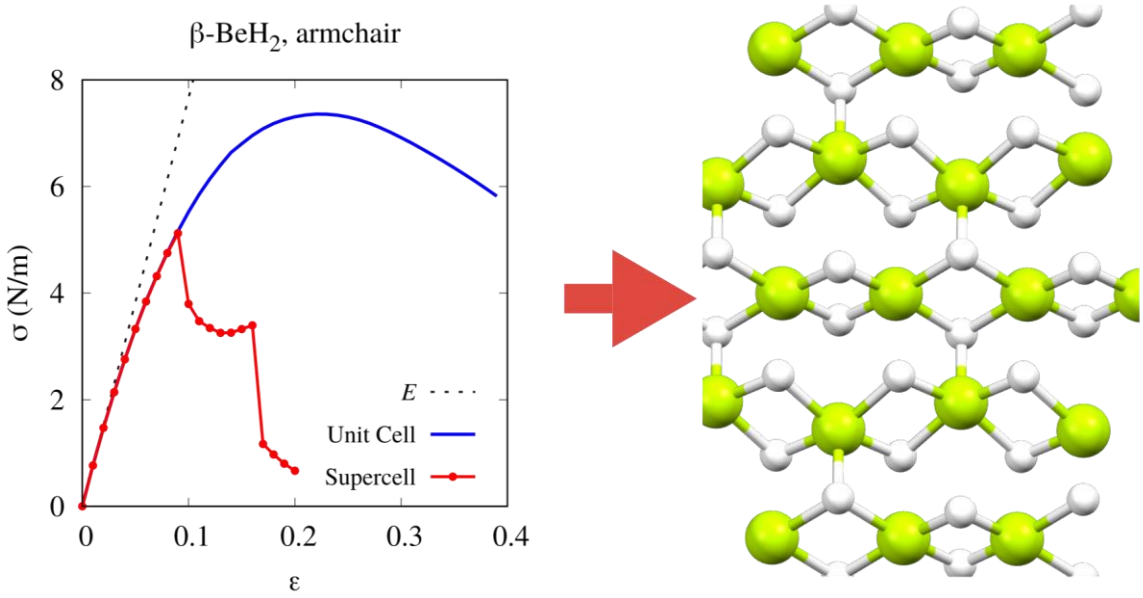

Figure 4.14. Stress-strain curves for β-BeH_2 under tensile strain in the armchair direction and plastically deformed structure. *E* is the infinitesimal elastic modulus, the blue curve is the calculated curve with a primitive cell, and in red, the calculated curve of a supercell.

These parameters are condensed in Table 4.3, together with the traverse strains, the out-of-plane distortions and bond lengths at the mechanical instabilities. The larger initial bond lengths in β-BeH_2, together with the computed bond strengths (Sect. 3.4) that revealed weaker Be-H contacts in β-BeH_2 (1.80 eV/atom) than in α-BeH_2 (2.70 eV/atom), could be indicators of the predicted failure at short strains for this solid. Not many 2D materials are known with low failure strains, which may open a new niche of applications.

Table 4.3. β-BeH_2 under strain in the zigzag and armchair directions. The elastic modulus (*E*), the critical strains (ε_c) and ideal tensile strengths (σ_c); together with the maximum strains (ε_t) and strengths (σ_t), the in-plane traverse strains ($\varepsilon_{\perp ip}$), out-of-plane distortions (Δz), and bond lengths (r) before phase transitions.

β-BeH_2, direction	*E* (N/m)	ε_c	σ_c (N/m)	ε_t	σ_t (N/m)	$\varepsilon_{\perp ip}$	Δz (Å)	r (Å)
zigzag	72.41	0.24	7.12	0.09	4.97	-0.02	1.71	1.71
armchair	73.68	0.22	7.43	0.09	5.21	-0.01	1.70	1.67

With graphene setting the gold standard in terms of strength (42 Nm^{-1}) and stiffness (340 Nm^{-1}) for 2D materials. The maximum strength output for any of the tested directions of the BeH_2 monolayer is only a mere fraction of the breaking strength of graphene. The α-BeH_2 polymorph has been predicted to be more resistant to forces than β-BeH_2, with biaxial loading as the most resistant direction in β-BeH_2 (5.71 Nm^{-1}), not as strong as the softer direction of α-BeH_2 (5.99 Nm^{-1}), also, biaxial loading. Other 2D materials of relatable strengths are black-phosphorus[95] with a tensile strength in the zigzag direction of 8.88 Nm^{-1}, and blue-phosphorus,[142] with predicted strengths of 7.06 Nm^{-1} (zigzag) and 6.72 Nm^{-1} (armchair).

Heavier group 14 and 15 allotropes reveal lower strengths, reasonably due to weakening of their bonds as the atomic radii and, in consequence, their bond lengths grow larger. The group 14 2D monochalcogenides,[76] also have strengths akin to the BeH_2 monolayers, the stronger of them, GeS, displays an ideal strength of 5.12 Nm^{-1} in the zigzag direction, much like the armchair direction of β-BeH_2. These puckered lattices reveal out-of-plane auxeticity and are very flexible monolayers, with SnSe owning a critical strain of 63% when strained in the armchair direction. Albeit, these computations are performed on unit cells, therefore, they do not account for the mechanical instabilities.

Summary

Herein, the computational results of the stability and mechanical properties of the 2D BeH_2 monolayers are presented. The ground-state and the linear elastic properties have been validated with the reports in the literature. On pairing bilayers at several stacking orders and calculating their interlayer interactions, the stability of the monolayers was assessed. Weak binding energies and large interlayer distances were computed, promoting these 2D crystals as stable free-standing monolayers of prospective lubricity.

The electronic properties have been estimated, predicting large band gaps that corresponded to the values in the literature. The chemical bond was also examined, the pDOS and pCOHP approaches signal the existence of delocalized bonding states throughout the valence bands, which translate to bonding contacts of both Be-Be and Be-H pairs. The computed bond strength for the Be-H contacts is greater in α-BeH_2. These interactions produce strong multicentered bonds, which develop surrounding the H atoms, as the literature reports.

After determination of the stiffness tensors, the direction-dependent elastic properties were computed. The anisotropy of α-BeH_2 delivered interesting results, as regions of large positive Poisson's ratios (PPR) were predicted. In accordance with the theory on auxetic solids, an NPR provides reinforcement to the elastic modulus.

The mechanical instabilities for uniaxial and biaxial strain directions were computed, the results give insight into the high flexibility of the crystals. The supercell method was adopted to predict the phase transitions in the same directions that computed the ideal tensile strengths. The newfound maximum strains reveal that α-BeH_2 has superior flexibility in comparison to most 2D materials. On the other hand, β-BeH_2, reveals phase transition at low strains, which might have in itself interesting applications.

The maximum strengths in both monolayers are of similar magnitudes, not as large as graphene or h-BN, but similar to black-phosphorus or silicene. The changes in the parameters of the monolayers against tension were also assessed.

A critical value for the bond length was estimated, as well as an interpretation of why one polymorph is more flexible than the other. The bidirectional auxetic behavior of the α-BeH_2 phase has been elucidated.

An out-of-plane transition into auxeticity has been revealed for the first time in α-BeH_2 strained in the diagonal direction. An opening hinge mechanism in the angle that binds atoms at opposing ends, together with equivalently increasing bond lengths begin to dominate and produce the out-of-plane NPR effect.

The in-plane auxeticity can be explained by an opening of the bond angle that is perpendicular to the direction of the applied strain, while keeping the traverse bond lengths virtually unchanged, thus flattening the layer, and producing the in-plane NPR effect.

Other 2D materials with this symmetry are very likely also to exhibit an in-plane NPR, and if conditions allow it, an out-of-plane NPR transition as well. In all, BeH_2 possesses very interesting properties that can be exploited in the realm of flexible and non-flexible applications.

Perspectives and Future Work

This work is not conclusive. Phonon instabilities are a proper way to complement on the predicted ideal tensile strengths, as they will also provide insight into the corresponding failure modes for each type of instability here presented.

The effect of multi-layered stacking on the mechanical properties is also to be addressed. A first inspection with the bilayered configurations revealed minimal to no change on the mechanical properties from single layers. However, it is also desirable to evaluate on systems of various layers and register their mechanical response.

A more in depth analysis of the bond strength in α-BeH_2 is in order, as to find a chemical reason on the evolution of the NPR, and if such behavior is exclusive of the BeH_2 system or if it is an intrinsic property of the lattice.

The heavier 2D alkaline-earth hydrides that share lattice with α-BeH_2, might tend to be less covalently bonded like their bulk counterparts, and result in less flexible structures.

References

1. Orowan, E., Fracture and strength of solids. *Rep. Prog. Phys.* **1949**, *12* (1), 185-232.
2. Ogata, S.; Umeno, Y.; Kohyama, M., First-principles approaches to intrinsic strength and deformation of materials: perfect crystals, nano-structures, surfaces and interfaces. *Model. Simul. Mater. Sc.* **2009**, *17* (1).
3. Novoselov, K. S.; Geim, A. K.; Morozov, S. V.; Jiang, D.; Zhang, Y.; Dubonos, S. V.; Grigorieva, I. V.; Firsov, A. A., Electric field effect in atomically thin carbon films. *Science* **2004**, *306* (5696), 666-669.
4. Novoselov, K. S.; Geim, A. K.; Morozov, S. V.; Jiang, D.; Katsnelson, M. I.; Grigorieva, I. V.; Dubonos, S. V.; Firsov, A. A., Two-dimensional gas of massless Dirac fermions in graphene. *Nature* **2005**, *438* (7065), 197-200.
5. Castro Neto, A. H.; Guinea, F.; Peres, N. M. R.; Novoselov, K. S.; Geim, A. K., The electronic properties of graphene. *Rev. Mod. Phys.* **2009**, *81* (1), 109-162.
6. Liu, F.; Ming, P. M.; Li, J., Ab initio calculation of ideal strength and phonon instability of graphene under tension. *Phys. Rev. B* **2007**, *76* (6).
7. Lee, C.; Wei, X. D.; Kysar, J. W.; Hone, J., Measurement of the elastic properties and intrinsic strength of monolayer graphene. *Science* **2008**, *321* (5887), 385-388.
8. Novoselov, K. S.; Jiang, D.; Schedin, F.; Booth, T. J.; Khotkevich, V. V.; Morozov, S. V.; Geim, A. K., Two-dimensional atomic crystals. *P. Natl. Acad. Sci. USA* **2005**, *102* (30), 10451-10453.
9. Ting, T. C. T.; Chen, T. Y., Poisson's ratio for anisotropic elastic materials can have no bounds. *Q. J. Mech. Appl. Math.* **2005**, *58*, 73-82.
10. Lakes, R. S., Negative-Poisson's-Ratio Materials: Auxetic Solids. *Annu. Rev. Mater. Res.* **2017**, *47*, 63-81.
11. Evans, K. E.; Alderson, A., Auxetic materials: Functional materials and structures from lateral thinking! *Adv. Mater.* **2000**, *12* (9), 617-+.
12. Lakes, R. S., Foam Structures with a Negative Poisson's Ratio. *Science* **1987**, *235* (4792), 1038-1040.
13. Jiang, J. W.; Park, H. S., Negative Poisson's ratio in single-layer black phosphorus. *Nat. Commun.* **2014**, *5*.
14. Du, Y. C.; Maassen, J.; Wu, W. R.; Luo, Z.; Xu, X. F.; Ye, P. D., Auxetic Black Phosphorus: A 2D Material with Negative Poisson's Ratio. *Nano. Lett.* **2016**, *16* (10), 6701-6708.
15. Saxena, K. K.; Das, R.; Calius, E. P., Three Decades of Auxetics Research - Materials with Negative Poisson's Ratio: A Review. *Adv. Eng. Mater.* **2016**, *18* (11), 1847-1870.
16. Peng, R.; Ma, Y. D.; Wu, Q.; Huang, B. B.; Dai, Y., Two-dimensional materials with intrinsic auxeticity: progress and perspectives. *Nanoscale* **2019**, *11* (24), 11413-11428.
17. Peng, R.; Ma, Y. D.; He, Z. L.; Huang, B. B.; Kou, L. Z.; Dai, Y., Single-Layer Ag_2S: A Two-Dimensional Bidirectional Auxetic Semiconductor. *Nano. Lett.* **2019**, *19* (2), 1227-1233.

18. Yuan, J. H.; Xue, K. H.; Wang, J. F.; Miao, X. S., Gallium Thiophosphate: An Emerging Bidirectional Auxetic Two-Dimensional Crystal with Wide Direct Band Gap. *J. Phys. Chem. Lett.* **2019**, *10* (15), 4455-4462.
19. Topsakal, M.; Cahangirov, S.; Ciraci, S., The response of mechanical and electronic properties of graphane to the elastic strain. *Appl. Phys. Lett.* **2010**, *96* (9), 091912.
20. Wei, Q.; Peng, X. H., Superior mechanical flexibility of phosphorene and few-layer black phosphorus. *Appl. Phys. Lett.* **2014**, *104* (25).
21. Akinwande, D.; Brennan, C. J.; Bunch, J. S.; Egberts, P.; Felts, J. R.; Gao, H. J.; Huang, R.; Kim, J. S.; Li, T.; Li, Y.; Liechti, K. M.; Lu, N. S.; Park, H. S.; Reed, E. J.; Wang, P.; Yakobson, B. I.; Zhang, T.; Zhang, Y. W.; Zhou, Y.; Zhu, Y., A review on mechanics and mechanical properties of 2D materials-Graphene and beyond. *Extreme. Mech. Lett.* **2017**, *13*, 42-77.
22. Castellanos-Gomez, A.; Singh, V.; van der Zant, H. S. J.; Steele, G. A., Mechanics of freely-suspended ultrathin layered materials. *Ann. Phys-Berlin* **2015**, *527* (1-2), 27-44.
23. Kim, J. H.; Jeong, J. H.; Kim, N.; Joshi, R.; Lee, G. H., Mechanical properties of two-dimensional materials and their applications. *J. Phys. D: Appl. Phys.* **2019**, *52* (8).
24. Mounet, N.; Gibertini, M.; Schwaller, P.; Campi, D.; Merkys, A.; Marrazzo, A.; Sohier, T.; Castelli, I. E.; Cepellotti, A.; Pizzi, G.; Marzari, N., Two-dimensional materials from high-throughput computational exfoliation of experimentally known compounds. *Nat. Nanotechnol.* **2018**, *13* (3), 246-+.
25. Choudhary, K.; Cheon, G.; Reed, E.; Tavazza, F., Elastic properties of bulk and low-dimensional materials using van der Waals density functional. *Phys. Rev. B* **2018**, *98* (1).
26. Haastrup, S.; Strange, M.; Pandey, M.; Deilmann, T.; Schmidt, P. S.; Hinsche, N. F.; Gjerding, M. N.; Torelli, D.; Larsen, P. M.; Riis-Jensen, A. C.; Gath, J.; Jacobsen, K. W.; Mortensen, J. J.; Olsen, T.; Thygesen, K. S., The Computational 2D Materials Database: high-throughput modeling and discovery of atomically thin crystals. *2D Mater.* **2018**, *5* (4).
27. Tang, C.; Kour, G.; Du, A., Recent progress on the prediction of two-dimensional materials using CALYPSO. *Chinese Phys. B* **2019**, *28* (10), 107306.
28. Zhou, X. C.; Hang, Y.; Liu, L. R.; Zhang, Z. H.; Guo, W. L., A Large Family of Synthetic Two-Dimensional Metal Hydrides. *J. Am. Chem. Soc.* **2019**, *141* (19), 7899-7905.
29. Seel, M.; Kunz, A. B.; Hill, S., Electronic structure of lithium beryllium hydride. *Phys. Rev. B* **1989**, *39* (11), 7949-7954.
30. Li, F.; Aeberhard, U.; Wu, H.; Qiao, M.; Li, Y. F., Global minimum beryllium hydride sheet with novel negative Poisson's ratio: first-principles calculations. *Rsc Adv.* **2018**, *8* (35), 19432-19436.
31. Wang, Y. C.; Lv, J. A.; Zhu, L.; Ma, Y. M., Crystal structure prediction via particle-swarm optimization. *Phys. Rev. B* **2010**, *82* (9).
32. Yang, B.; Zhang, X.; Zhao, M., Dirac node lines in two-dimensional Lieb lattices. *Nanoscale* **2017**, *9* (25), 8740-8746.
33. Landau, L. D.; Lifshitz, E. M.; Pitaevskiĭ, L. P.; Sykes, J. B.; Kearsley, M. J.; EBSCOhost, *Statistical physics. Volume 5 of Course of theoretical physics. Part 1*. Third edition, revised and enlarged / ed.; Pergamon Press: Oxford, England ; New York, **1980**; p 1 online resource (563 pages).
34. Mermin, N. D., Crystalline Order in 2 Dimensions. *Phys. Rev.* **1968**, *176* (1), 250-&.

35. Zhang, Y.; Tan, Y.-W.; Stormer, H. L.; Kim, P., Experimental observation of the quantum Hall effect and Berry's phase in graphene. *Nature* **2005**, *438* (7065), 201-204.
36. Berger, C.; Song, Z.; Li, X.; Wu, X.; Brown, N.; Naud, C.; Mayou, D.; Li, T.; Hass, J.; Marchenkov, A. N.; Conrad, E. H.; First, P. N.; de Heer, W. A., Electronic Confinement and Coherence in Patterned Epitaxial Graphene. *Science* **2006**, *312* (5777), 1191-1196.
37. Bolotin, K. I.; Sikes, K. J.; Jiang, Z.; Klima, M.; Fudenberg, G.; Hone, J.; Kim, P.; Stormer, H. L., Ultrahigh electron mobility in suspended graphene. *Solid State Commun.* **2008**, *146* (9), 351-355.
38. Ning, G.; Fan, Z.; Wang, G.; Gao, J.; Qian, W.; Wei, F., Gram-scale synthesis of nanomesh graphene with high surface area and its application in supercapacitor electrodes. *Chem. Commun.* **2011**, *47* (21), 5976-5978.
39. Guo, B.; Xiao, Q.-l.; Wang, S.-h.; Zhang, H., 2D Layered Materials: Synthesis, Nonlinear Optical Properties, and Device Applications. *Laser & Photonics Reviews* **2019**, *13* (12), 1800327.
40. Xiao, X.; Wang, H.; Urbankowski, P.; Gogotsi, Y., Topochemical synthesis of 2D materials. *Chem. Soc. Rev.* **2018**, *47* (23), 8744-8765.
41. Huang, Y.; Pan, Y.-H.; Yang, R.; Bao, L.-H.; Meng, L.; Luo, H.-L.; Cai, Y.-Q.; Liu, G.-D.; Zhao, W.-J.; Zhou, Z., Universal mechanical exfoliation of large-area 2D crystals. *Nat Commun* **2020**, 11, 2453.
42. Galbiati, M.; Motta, N.; De Crescenzi, M.; Camilli, L., Group-IV 2D materials beyond graphene on nonmetal substrates: Challenges, recent progress, and future perspectives. *Appl. Phys. Rev.* **2019**, *6* (4).
43. Gao, N.; Liu, H. S.; Zhou, S.; Bai, Y. Z.; Zhao, J. J., Interaction between Post-Graphene Group-IV Honeycomb Monolayers and Metal Substrates: Implication for Synthesis and Structure Control. *J. Phys. Chem. C* **2017**, *121* (9), 5123-5129.
44. Zhan, H.; Guo, D.; Xie, G. X., Two-dimensional layered materials: from mechanical and coupling properties towards applications in electronics. *Nanoscale* **2019**, *11* (28), 13181-13212.
45. Braghin, F. L.; Hasselmann, N., Thermal fluctuations of free-standing graphene. *Phys. Rev. B* **2010**, *82* (3).
46. Meyer, J. C.; Geim, A. K.; Katsnelson, M. I.; Novoselov, K. S.; Booth, T. J.; Roth, S., The structure of suspended graphene sheets. *Nature* **2007**, *446* (7131), 60-63.
47. Geim, A. K.; Novoselov, K. S., The rise of graphene. *Nat. Mater.* **2007**, *6* (3), 183-191.
48. Zollner, K.; Gmitra, M.; Fabian, J., Heterostructures of graphene and hBN: Electronic, spin-orbit, and spin relaxation properties from first principles. *Phys. Rev. B* **2019**, *99* (12), 125151.
49. Schmidt, H.; Giustiniano, F.; Eda, G., Electronic transport properties of transition metal dichalcogenide field-effect devices: surface and interface effects. *Chem. Soc. Rev.* **2015**, *44* (21), 7715-7736.
50. Miro, P.; Audiffred, M.; Heine, T., An atlas of two-dimensional materials. *Chem. Soc. Rev* **2014**, *43* (18), 6537-6554.
51. Li, R. S.; Shao, Q.; Gao, E. L.; Liu, Z., Elastic anisotropy measure for two-dimensional crystals. *Extreme Mech. Lett.* **2020**, *34*.

52. Vogt, P.; De Padova, P.; Quaresima, C.; Avila, J.; Frantzeskakis, E.; Asensio, M. C.; Resta, A.; B., E.; Le Lay, G., Silicene: compelling experimental evidence for graphenelike two-dimensional silicon. *Phys. Rev. Lett.* **2012**, *108*.
53. Cahangirov, S.; Topsakal, M.; Akturk, E.; Sahin, H.; Ciraci, S., Two- and One-Dimensional Honeycomb Structures of Silicon and Germanium. *Phys. Rev. Lett.* **2009**, *102* (23).
54. Liu, H. S.; Feng, H. F.; Du, Y.; Chen, J.; Wu, K. H.; Zhao, J. J., Point defects in epitaxial silicene on Ag(111) surfaces. *2d Mater.* **2016**, *3* (2).
55. De Padova, P.; Feng, H. F.; Zhuang, J. C.; Li, Z.; Generosi, A.; Paci, B.; Ottaviani, C.; Quaresima, C.; Olivieri, B.; Krawiec, M.; Du, Y., Synthesis of Multilayer Silicene on Si(111)root 3 x root 3-Ag. *J. Phys. Chem. C* **2017**, *121* (48), 27182-27190.
56. Davila, M. E.; Le Lay, G., Few layer epitaxial germanene: a novel two-dimensional Dirac material. *Sci. Rep-Uk* **2016**, *6*.
57. Maniraj, M.; Stadtmuller, B.; Jungkenn, D.; Duvel, M.; Emmerich, S.; Shi, W.; Stockl, J.; Lyu, L.; Kollamana, J.; Wei, Z.; Jurenkow, A.; Jakobs, S.; Yan, B.; Steil, S.; Cinchetti, M.; Mathias, S.; Aeschlimann, M., A case study for the formation of stanene on a metal surface. *Commun. Phys-Uk* **2019**, *2*.
58. Padilha, J. E.; Pontes, R. B., Free-Standing Bilayer Silicene: The Effect of Stacking Order on the Structural, Electronic, and Transport Properties. *J. Phys. Chem. C* **2015**, *119* (7), 3818-3825.
59. Yaokawa, R.; Ohsuna, T.; Morishita, T.; Hayasaka, Y.; Spencer, M. J. S.; Nakano, H., Monolayer-to-bilayer transformation of silicenes and their structural analysis. *Nat. Commun.* **2016**, *7* (1), 10657.
60. Geim, A. K.; Grigorieva, I. V., Van der Waals heterostructures. *Nature* **2013**, *499* (7459), 419-425.
61. Kadioglu, Y.; Santana, J. A.; Özaydin, H. D.; Ersan, F.; Aktürk, O. Ü.; Aktürk, E.; Reboredo, F. A., Diffusion quantum Monte Carlo and density functional calculations of the structural stability of bilayer arsenene. *J. Chem. Phys.* **2018**, *148* (21), 214706.
62. Ahn, J.; Hong, I.; Kwon, Y.; Clay, R. C.; Shulenburger, L.; Shin, H.; Benali, A., Phase stability and interlayer interaction of blue phosphorene. *Phys. Rev. B* **2018**, *98* (8).
63. Arcudia, J.; Kempt, R.; Cifuentes-Quintal, M. E.; Heine, T.; Merino, G., Blue phosphorene bilayer is a two-dimensional metal: An unambiguous classification scheme for buckled hexagonal bilayers. *Phys. Rev. Lett.* **2020**, 125, 196401.
64. Zhang, S.; Ma, T.; Erdemir, A.; Li, Q., Tribology of two-dimensional materials: From mechanisms to modulating strategies. *Mat. Tod.* **2019**, *26*, 67-86.
65. Liu, H.; Neal, A. T.; Zhu, Z.; Luo, Z.; Xu, X. F.; Tomanek, D.; Ye, P. D., Phosphorene: An Unexplored 2D Semiconductor with a High Hole Mobility. *Acs Nano* **2014**, *8* (4), 4033-4041.
66. Dai, J.; Zeng, X. C., Structure and stability of two dimensional phosphorene with =O or =NH functionalization. *Rsc Adv.* **2014**, *4* (89), 48017-48021.
67. Wang, L. Q.; Kutana, A.; Zou, X. L.; Yakobson, B. I., Electro-mechanical anisotropy of phosphorene. *Nanoscale* **2015**, *7* (21), 9746-9751.
68. Landau, L. D.; Lifshitz, E. M.; Sykes, J. B.; Reid, W. H., *Theory of elasticity*. 2nd English ed.; Pergamon: Oxford, **1970**; p viii, 165 p.

69. Evans, K. E.; Nkansah, M. A.; Hutchinson, I. J.; Rogers, S. C., Molecular Network Design. *Nature* **1991**, *353* (6340), 124-124.
70. Baughman, R. H.; Shacklette, J. M.; Zakhidov, A. A.; Stafstrom, S., Negative Poisson's ratios as a common feature of cubic metals. *Nature* **1998**, *392* (6674), 362-365.
71. Baughman, R. H., Auxetic materials: Avoiding the shrink. *Nature* **2003**, *425* (6959), 667-667.
72. Sanami, M.; Ravirala, N.; Alderson, K.; Alderson, A., Auxetic materials for sports applications. *Procedia Engineer.* **2014**, *72*, 453-458.
73. Choi, J. B.; Lakes, R. S., Fracture toughness of re-entrant foam materials with a negative Poisson's ratio: Experiment and analysis. *Int. J. Fracture* **1996**, *80* (1), 73-83.
74. Phani, A. S.; Woodhouse, J.; Fleck, N. A., Wave propagation in two-dimensional periodic lattices. *J. Acoust. Soc. Am.* **2006**, *119* (4), 1995-2005.
75. Wang, H. D.; Li, X. X.; Li, P.; Yang, J. L., delta-Phosphorene: a two dimensional material with a highly negative Poisson's ratio. *Nanoscale* 2017, *9* (2), 850-855.
76. Gao, Y.; Zhang, L. L.; Yao, G.; Wang, H. F., Unique mechanical responses of layered **phosphorus-like group-IV monochalcogenides. *J. Appl. Phys.* 2019, *125* (8).**
77. Han, J. W.; Xie, J. F.; Zhang, Z. Y.; Yang, D. Z.; Si, M. S.; Xue, D. S., Negative Poisson's ratios in few-layer orthorhombic arsenic: First-principles calculations. *Appl. Phys. Express* **2015**, *8* (4).
78. Jiang, J.-W.; Chang, T.; Guo, X.; Park, H. S., Intrinsic Negative Poisson's Ratio for Single-Layer Graphene. *Nano Lett.* **2016**, *16* (8), 5286-5290.
79. Deng, B. H.; Hou, J.; Zhu, H. X.; Liu, S.; Liu, E.; Shi, Y. F.; Peng, Q., The normal-auxeticity mechanical phase transition in graphene. *2d Mater.* **2017**, *4* (2).
80. Cadelano, E.; Palla, P. L.; Giordano, S.; Colombo, L., Elastic properties of hydrogenated graphene. *Phys. Rev. B* **2010**, *82* (23).
81. Rong, X.; Li, Y.; Han, S.; Cao, P.; Zeng, Y.; Xu, W.; Fang, M.; Liu, W.; Zhu, D.; Lu, Y., Electric field modulation in the auxetic effect of BP-analog monolayer As and Sb by first-principles calculations. *Phys. Chem. Chem. Phys.* **2020**, 22, 8739-8744.
82. Wang, B.; Wu, Q. S.; Zhang, Y. H.; Ma, L.; Wang, J. L., Auxetic B_4N Monolayer: A Promising 2D Material with in-Plane Negative Poisson's Ratio and Large Anisotropic Mechanics. *Acs Appl. Mater. Inter.* **2019**, *11* (36), 33231-33237.
83. Pokluda, J.; Cerny, M.; Sob, M.; Umeno, Y., Ab initio calculations of mechanical properties: Methods and applications. *Prog. Mater. Sci.* **2015**, *73*, 127-158.
84. Kitamura, T.; Umeno, Y.; Kushima, A., Ideal strength of nano-components. *Mater. Sci. Forum* **2005**, *482*, 25-32.
85. Clatterbuck, D. M.; Krenn, C. R.; Cohen, M. L.; Morris, J. W., Phonon instabilities and the ideal strength of aluminum. *Phys. Rev. Lett.* **2003**, *91* (13).
86. Řehák, P.; Černý, M.; Pokluda, J., Dynamic stability of fcc crystals under isotropic loading from first principles. *J. Phys. Condens. Matter* **2012**, *24* (21), 215403.
87. Li, X.; Sun, M.; Shan, C. X.; Chen, Q.; Wei, X. L., Mechanical Properties of 2D Materials Studied by In Situ Microscopy Techniques. *Adv. Mater. Interfaces* **2018**, *5* (5).
88. Sun, Y. F.; Liu, K., Strain engineering in functional 2-dimensional materials. *J. Appl. Phys.* **2019**, *125* (8).
89. Marianetti, C. A.; Yevick, H. G., Failure Mechanisms of Graphene under Tension. *Phys. Rev. Lett.* **2010**, *105* (24).

90. Falin, A.; Cai, Q. R.; Santos, E. J. G.; Scullion, D.; Qian, D.; Zhang, R.; Yang, Z.; Huang, S. M.; Watanabe, K.; Taniguchi, T.; Barnett, M. R.; Chen, Y.; Ruoff, R. S.; Li, L. H., Mechanical properties of atomically thin boron nitride and the role of interlayer interactions. *Nat. Commun.* **2017**, *8*.
91. Peng, Q.; Ji, W.; De, S., Mechanical properties of the hexagonal boron nitride monolayer: Ab initio study. *Comp. Mater. Sci.* **2012**, *56*, 11-17.
92. Bertolazzi, S.; Brivio, J.; Kis, A., Stretching and Breaking of Ultrathin MoS_2. *Acs Nano* **2011**, *5* (12), 9703-9709.
93. Cooper, R. C.; Lee, C.; Marianetti, C. A.; Wei, X. D.; Hone, J.; Kysar, J. W., Nonlinear elastic behavior of two-dimensional molybdenum disulfide. *Phys. Rev. B* **2013**, *87* (3).
94. Isaacs, E. B.; Marianetti, C. A., Ideal strength and phonon instability of strained monolayer materials. *Phys. Rev. B* **2014**, *89* (18).
95. Tian, H.; Seh, Z. W.; Yan, K.; Fu, Z.; Tang, P.; Lu, Y.; Zhang, R.; Legut, D.; Cui, Y.; Zhang, Q., Theoretical Investigation of 2D Layered Materials as Protective Films for Lithium and Sodium Metal Anodes. *Adv. Energy Mater.* **2017**, *7* (13), 1602528.
96. Jiang, J.-W.; Park, H. S., Mechanical properties of single-layer black phosphorus. *J. Phys. D: App. Phys.* **2014**, *47* (38), 385304.
97. Wang, J.-Y.; Li, Y.; Zhan, Z.-Y.; Li, T.; Zhen, L.; Xu, C.-Y., Elastic properties of suspended black phosphorus nanosheets. *Appl. Phys. Lett.* **2016**, *108* (1), 013104.
98. Gere, J. D.; Timoshenko, S. P., *Mechanics of Materials*. 3rd ed.; Springer Science+ Business Media Dordrecht: Boston, **1991**; p 827.
99. Roylance, D., *Mechanics of materials*. Wiley: New York ; Chichester, **1996**; p xv, 315 p.
100. Field, J. E., The mechanical and strength properties of diamond. *Rep. Prog. Phys.* **2012**, *75* (12), 126505.
101. Coates, G. E.; Glockling, F., Diisopropylberyllium and some beryllium hydrides. *J. Chem. Soc. (Resumed)* **1954**, (0), 22-27.
102. Coates, G. E.; Glockling, F., Di-tert.-butylberyllium and beryllium hydride. *J. Chem. Soc. (Resumed)* **1954**, (0), 2526-2529.
103. Head, E. L.; Holley, C. E.; Rabideau, S. W., Di-t-butylberyllium and Beryllium Hydride 1. *J. Am. Chem. Soc.* **1957**, *79* (14), 3687-3689.
104. Armstrong, D. R.; Jamieson, J.; Perkins, P. G., Electronic-Structures of Polymeric Beryllium Hydride and Polymeric Boron Hydride. *Theor. Chim. Acta* **1979**, *51* (2), 163-172.
105. Clark, J. D., *Ignition! An Informal History of Liquid Rocket Propellants*. 1 ed.; Rutgers University Press: New Jersey, **1972**; p 192.
106. Grochala, W.; Edwards, P. P., Thermal Decomposition of the Non-Interstitial Hydrides for the Storage and Production of Hydrogen. *Chem. Rev.* **2004**, *104* (3), 1283-1316.
107. Shark, S.; Sippel, T.; Son, S.; Heister, S.; Pourpoint, T., Theoretical Performance Analysis of Metal Hydride Fuel Additives for Rocket Propellant Applications. In *47th AIAA/ASME/SAE/ASEE Joint Propulsion Conference & Exhibit*, **2012**.
108. Ashcroft, N. W., Hydrogen Dominant Metallic Alloys: High Temperature Superconductors? *Phys. Rev. Lett.* **2004**, *92* (18), 187002.

109. Wang, Z. W.; Yao, Y. S.; Zhu, L.; Liu, H. Y.; Iitaka, T.; Wang, H.; Ma, Y. M., Metallization and superconductivity of BeH_2 under high pressure. *J. Chem. Phys.* **2014**, *140* (12).
110. Yu, S. Y.; Zeng, Q. F.; Oganov, A. R.; Hu, C. H.; Frapper, G.; Zhang, L. T., Exploration of stable compounds, crystal structures, and superconductivity in the Be-H system. *Aip Adv.* **2014**, *4* (10).
111. Zhang, C.; Chen, X.-J.; Zhang, R.-Q.; Lin, H.-Q., Chemical Trend of Pressure-Induced Metallization in Alkaline Earth Hydrides. *J. Phys. Chem. C* **2010**, *114* (34), 14614-14617.
112. Smith, G. S.; Johnson, Q. C.; Smith, D. K.; Cox, D. E.; Snyder, R. L.; Zhou, R. S.; Zalkin, A., The Crystal and Molecular-Structure of Beryllium Hydride. *Solid State Commun.* **1988**, *67* (5), 491-494.
113. Vajeeston, P.; Ravindran, P.; Kjekshus, A.; Fjellvag, H., Structural stability of BeH_2 at high pressures. *Appl. Phys. Lett.* **2004**, *84* (1), 34-36.
114. Iddir, H.; Zapol, P.; Kolesnikov, A. I., Theoretical investigation of the vibrational properties of BeH_2 and Li_2BeH_4. *Phys. Rev. B* **2009**, *80* (13).
115. Zdetsis, A. D.; Sigalas, M. M.; Koukaras, E. N., Ab initio theoretical investigation of beryllium and beryllium hydride nanoparticles and nanocrystals with implications for the corresponding infinite systems. *Phys. Chem. Chem. Phys.* **2014**, *16* (27), 14172-14182.
116. Seel, M., Abinitio Band-Structure Studies of Beryllium and Beryllium-Hydrogen Ultrathin Films. *Phys. Rev. B* **1991**, *43* (12), 9532-9537.
117. Wu, J. Z.; Trickey, S. B.; Boettger, J. C., Beryllium-hydrogen ultrathin films. I. Metallic behavior of the BeH_2 monolayer. *Phys. Rev. B* **1990**, *42* (3), 1663-1667.
118. Jain, A.; Ong, S. P.; Hautier, G.; Chen, W.; Richards, W. D.; Dacek, S.; Cholia, S.; Gunter, D.; Skinner, D.; Ceder, G.; Persson, K. A., Commentary: The Materials Project: A materials genome approach to accelerating materials innovation. *APL Mater.* **2013**, *1* (1), 011002.
119. Greeves, N. ChemTube3D Gallery of Rotatable Structures. https://www.chemtube3d.com/beh2/ (accessed April 25, 2020).
120. Galeev, T. R.; Dunnington, B. D.; Schmidt, J. R.; Boldyrev, A. I., Solid state adaptive natural density partitioning: a tool for deciphering multi-center bonding in periodic systems. *Phys. Chem. Chem. Phys.* **2013**, *15* (14), 5022-5029.
121. Reddy, J. N., *An introduction to continuum mechanics*. Cambridge university press: **2008**; p 360.
122. Cadelano, E. Graphene Under Strain. PhD, Universita‘ Degli Studi Di Cagliari, Cagliari, **2010**.
123. Transformation of a tensor to a new coordinate system. https://www.rockmechs.com/tensor-transformation-rotation/ (accessed April 25, 2020).
124. Mouhat, F.; Coudert, F.-X., Necessary and sufficient elastic stability conditions in various crystal systems. *Phys. Rev. B* **2014**, *90* (22), 224104.
125. Perdew, J. P.; Burke, K.; Ernzerhof, M., Generalized gradient approximation made simple. *Phys. Rev. Lett.* **1996**, *77* (18), 3865-3868.
126. Kresse, G.; Furthmuller, J., Efficiency of ab-initio total energy calculations for metals and semiconductors using a plane-wave basis set. *Comp. Mater. Sci.* **1996**, *6* (1), 15-50.

127. Kresse, G.; Furthmuller, J., Efficient iterative schemes for ab initio total-energy calculations using a plane-wave basis set. *Phys. Rev. B.* **1996**, *54* (16), 11169-11186.
128. Blochl, P. E., Projector Augmented-Wave Method. *Phys. Rev. B* **1994**, *50* (24), 17953-17979.
129. Kresse, G.; Joubert, D., From ultrasoft pseudopotentials to the projector augmented-wave method. *Phys. Rev. B* **1999**, *59* (3), 1758-1775.
130. Grimme, S., Semiempirical GGA-type density functional constructed with a long-range dispersion correction. *J. Comput. Chem.* **2006**, *27* (15), 1787-1799.
131. Maintz, S.; Deringer, V. L.; Tchougréeff, A. L.; Dronskowski, R., LOBSTER: A tool to extract chemical bonding from plane-wave based DFT. *J. Comput. Chem.* **2016**, *37* (11), 1030-1035.
132. Maintz, S.; Deringer, V. L.; Tchougréeff, A. L.; Dronskowski, R., Analytic projection from plane-wave and PAW wavefunctions and application to chemical-bonding analysis in solids. *J. Comput. Chem.* **2013**, *34* (29), 2557-2567.
133. Deringer, V. L.; Tchougréeff, A. L.; Dronskowski, R., Crystal Orbital Hamilton Population (COHP) Analysis As Projected from Plane-Wave Basis Sets. *J. Phys. Chem. A* **2011**, *115* (21), 5461-5466.
134. Dronskowski, R.; Bloechl, P. E., Crystal orbital Hamilton populations (COHP): energy-resolved visualization of chemical bonding in solids based on density-functional calculations. *J. Phys. Chem.* **1993**, *97* (33), 8617-8624.
135. Hughbanks, T.; Hoffmann, R., Chains of trans-edge-sharing molybdenum octahedra: metal-metal bonding in extended systems. *J. Am. Chem. Soc.* **1983**, *105* (11), 3528-3537.
136. Ahlrichs, R., Ab initio calculations on small hydrides including Electron correlation. *Theor. Chim. Acta* **1970**, 17 (5), 348-361.
137. Yang, L.-M.; Bačić, V.; Popov, I. A.; Boldyrev, A. I.; Heine, T.; Frauenheim, T.; Ganz, E., Two-Dimensional Cu_2Si Monolayer with Planar Hexacoordinate Copper and Silicon Bonding. *J. Am. Chem. Soc.* **2015**, *137* (7), 2757-2762.
138. Guo, H.; Lu, N.; Dai, J.; Wu, X.; Zeng, X. C., Phosphorene Nanoribbons, Phosphorus Nanotubes, and van der Waals Multilayers. *J. Phys. Chem. C* **2014**, 118 (25), 14051-14059.
139. Koskinen, P.; Malola, S.; Häkkinen, H., Self-Passivating Edge Reconstructions of Graphene. *Phys. Rev. Lett.* **2008**, 101, 115502.
140. Wang, Y.; Li, F.; Li, Y. F.; Chen, Z. F., Semi-metallic Be_5C_2 monolayer global minimum with quasi-planar pentacoordinate carbons and negative Poisson's ratio. *Nat. Commun.* **2016**, *7*.
141. Chen, X.; Tian, F.; Persson, C.; Duan, W.; Chen, N.-x., Interlayer interactions in graphites. *Sci. Rep.-Uk* **2013**, *3* (1), 3046.
142. Liu, G.; Gao, Z. B.; Zhou, J., Strain effects on the mechanical properties of Group-V monolayers with buckled honeycomb structures. *Physica E* **2019**, *112*, 59-65.